Thesis, FRANZEN Rachelle

Auteur : Sauté, Lisa
Promoteur(s) : Nguyen, Laurent
Faculté : Faculté de Médecine
Diplôme : Master en sciences biomédicales, à finalité approfondie
Année académique : 2025-2026
URI/URL : http://hdl.handle.net/2268.2/25984

INVESTIGATION OF MIGRATING INTERNEURONS SECRETOME FROM HUMAN ORGANOIDS

LISA SAUTÉ

PROMOTER : LAURENT NGUYEN

MASTER 2 - BIOMEDICAL SCIENCES
ULIEGE 2025-2026

LIÈGE université
GIGA
Neuroscience

ACKNOWLEDGEMENTS

First, I would like to thank Pr. Laurent Nguyen for letting me do my internship in his laboratory, in a really welcoming and encouraging team. I also want to thank him for giving me the opportunity to continue in his lab for a PhD.

A very special thanks to Anaïs Boutsen for her guidance during those five months. You taught me so much. You were there to celebrate the success of experiments, but also during difficult and frustrating times. This internship wouldn't have been the same without you.

Thanks to Antonella Bonafina. You always found time for me in your really busy schedule. All your knowledge is a real inspiration to me.

Thanks to Miriam, Natali, Sergio, Erwan Pauline, Hannah, Gérald, Fatemeh, Sylvia, Manon, Léa, Coralie, Aurore and all the other members of the team for all those lunchtime discussions. You have all been a great help, whether with advice or entertainment.

Thank you to the jury for taking the time to read and evaluate this work.

Thanks to my friends with whom I have shared these last 3 years. Even the most boring classes become good memories thanks to you. A particular thanks to Sadaf and Ilona with whom I shared the lab corridors during this internship. You were such great supports.

Thank you to my family for supporting me throughout my studies. They probably still don't know what they consist of or what the future holds for me (no dad, I'm not going to become a physician), but they never stopped believing in me.

SUMMARY

The cerebral cortex is the outer layer of the brain, responsible of higher cognitive functions. It is populated by two main types of neurons: i – the excitatory projection neurons which, during development, migrate radially through the cortex; and ii – the inhibitory interneurons (cINs) that originate ventrally at the medial and the caudal ganglionic eminence (MGE and CGE, respectively) and preoptic area and migrate tangentially to the developing cortex. cINs migrate via nucleokinesis: a saltatory movement characterized by a nuclear jump. During this process, they respond to extracellular diffusible cues released by surrounding cells, which allows intercellular communication that will influence their trajectory and promote their survival. Cortical interneurons also secrete signals that will influence neighboring cells, such as intermediate progenitors (IPs), by promoting their proliferation (REF). The identity of these cues has not yet been elucitated, and whether they are conserved between mice and human remains unknown. The aim of my thesis is to characterize a novel human ventral forebrain organoid model to study cINs migration, and to set a protocol to study the diffusible cues that modulate their migration. Here, I characterized them by immunolabaling to identify ventral progenitors (NKX2.1, SOX2), immature interneurons (TUJ1), MGE mature cINs (SST28, GAD67), and oligodendrocyte precursor cells (OPCs) (SOX10). In addition I performed RT-qPCRs at different time points of the protocol to track the maturation of cINs. Results revealed that gene expression is stable between cell lines, including some genes of interest such as *NKX2.1, DLX5, DCX* and *GAD67,* further confirming the ventral forebrain identity. The second part of my thesis focuses on developing a protocol to collect the secretome of migrating cINs derived from human ventral organoids. The secretome refers to the complete set of proteins actively secreted by a cell into the extracellular space. To achieve this goal, GFP+ cINs were isolated from other progenitor populations by FACS after infection of the organoids with a DLX5/6-GFP lentivirus. Once sorted and put in culture, cells undergo two starvation periods before medium collection. The collected samples were sent to the mass spectrometry platform at the University of Liège for analysis. This platform will provide a list of proteins specifically secreted by interneurons. Identified candidates will subsequently be screen bibliographically and analyse by bioinformatic approaches to assess their potential roles in the crosstalk occurring between IPs and cINs. The protocol is now established, and we expect to identify proteins associated with cell proliferation or migration.

RESUME

Le cortex cérébral est la couche externe du cerveau, responsable des fonctions cognitives supérieures. Il est principalement composé de deux types de neurones : i – les neurones de projection excitateurs qui, pendant leur développement, migrent radialement à travers le cortex ; et ii – les interneurones inhibiteurs (cINs) qui prennent naissance ventralement dans l'éminence ganglionnaire médiale (MGE) et à la zone préoptique et migrent de manière tangentielle vers le cortex en développement. Les cINs migrent via la nucléocinèse : un mouvement saltatoire caractérisé par un saut nucléaire. Au cours de ce processus, les cINs répondent aux signaux diffusibles extracellulaires libérés par les cellules environnantes, ce qui permet une communication intercellulaire qui influencera leur trajectoire et favorisera leur survie. Ces interneurones sécrètent également des signaux qui influenceront les cellules voisines, comme les progéniteurs intermédiaires (IPs), en favorisant leur prolifération (REF). L'identité de ces signaux reste inconnue. Le premier objectif de mon mémoire est de caractériser un modèle d'organoïde ventral humain pour étudier la migration des cINs. Ils ont été caractérisés par immunofluorescence permettant d'identifier la présence de progéniteurs ventraux (NKX2.1, SOX2), d'interneurones immatures (TUJ1), de cINS matures de MGE (SST28, GAD67), et d'OPC (SOX10), ainsi que par RT-qPCR à 60 et 90 jours de croissance pour suivre leur maturation. Les résultats ont révélé que l'expression des gènes est stable entre les lignées cellulaires et que des gènes d'intérêt tels que *NKX2.1, DLX5, DCX* et *GAD67* sont exprimés, confirmant l'identité ventrale des organoïdes. La seconde partie de ma thèse porte sur le développement d'un protocole pour collecter le sécrétome des cINs dérivés des organoïdes ventraux. Le sécrétome désigne l'ensemble complet des protéines sécrétées par une cellule. Pour y parvenir, les cINs GFP+ sont isolés des cellules progénitrices par FACS après infection des organoïdes avec un lentivirus DLX5/6-GFP. Une fois triées et mises en culture, les cellules subissent deux périodes de « starving » avant que le milieu ne soit collecté. Les échantillons collectés seront analysés par la plateforme de spectrométrie de masse de l'Université de Liège afin de fournir une liste des protéines spécifiquement sécrétées par les interneurones qui influence la prolifération des IPs. Les candidats identifiés seront ensuite analysés bibliographiquement afin d'évaluer leurs rôles potentiels dans la prolifération ou la migration.

ACRONYMS

5HT3R = 5-hydroxytryptamine (serotonin) receptor 3
ANOVA = Analysis of variance
APC = Adenomatous Polyposis Coli
BCA = bicinchoninic acid
BDNF = brain derived neurotrophic factor
BMP = bone morphogenetic protein
BSA = bovine serum albumin
CCP = cytosolic carboxypeptidase
cIN = cortical interneuron
CGE = caudal ganglionic eminence
CRCR = C-X-C Motif Chemokine Receptor
CRISPR Cas9 = Clustered Regularly Interspaced Short Palindromic Repeats–CRISPR-associated Protein 9
CXCL = C-X-C Motif Chemokine Ligand
DAPI = 4',6-diamidino-2-phenylindole
DCX = doublecortin
dNTP = deoxynucleotide triphosphate
DLX = distal-less homeobox
DMEM/F12 = Dulbecco's Modified Eagle Medium / Nutrient Mixture F-12
DMS = deep migratory stream
dPBS = Dulbecco's phosphate-buffered saline
ECL = enhanced chemiluminescence
EphA4 = Ephrin Type-A Receptor 4
FACS = fluorescence-activated cell sorting
FGF / bFGF = fibroblast growth factor
FIJI = Fiji Is Just ImageJ
GABA = gamma-aminobutyric acid
GAD = glutamate decarboxylase
GFP = green fluorescent protein
GLI = Glioma-Associated Oncogene Homolog
GW = gestational week
H = hour
HBSS = Hanks' Balanced Salt Solution
hdCO = guman dorsal cerebral organoid
hESC = human embryonic stem cells
HGF = Hepatocyte Growth Factor
hvCO = human ventral cerebral organoid
IF = immunofluorescence
IN = interneurons
IP = intermediate progenitors
iPSC = induced pluripotent stem cell
IZ = intermediate zone
KO = knockout
KO serum = knockout serum
LC = liquid chromatography
LGE = lateral ganglionic eminence
LIS1 = Lissencephaly 1
LOF = loss of function
MEM-NEAA = minimum essential medium non-essential amino acids
Min = minute(s)
MGE = medial ganglionic eminence
MLC = myosin light chain
MLCK = myosin light chain kinase
MOI = multiplicity of infection
mRNA = messenger ribonucleic acid
MS = mass spectrometry
mTeSR = modified Tenneille's Serum Replacement
MZ = marginal zone
NSC = neuroepithelial stem cell
NDM-A = neural differentiation medium without vitamin A
Ncadh = N-Cadherin
NIM = neural induction medium
NKX2.1 = NK2 homeobox 1
NSC = neural stem cell
NT = neurotrophin
OCT (compound) = optimal cutting temperature compound
OCT4 = Octamer-binding transcription factor 4 (si vous utilisez OKSM séparément)
OKSM = Oct4, Sox2, c-Myc, Klf4
OPC = oligodendrocyte precursor cell
oRG = outer radial glial cell
oSVZ = outer subventricular zone
PBS = phosphate-buffered saline
PDL = poly-D-lysine
PFA = paraformaldehyde
PMT = photomultipler tubes
PN = projection neuron
POA = preoptic area
PTCH1 = patched1
PV = parvalbumin
PVDF =polyvinylidene fluoride
qPCR = quantitative polymerase chain reaction
RA = retinoic acid
RGC = radial glial cell
RI = ROCK inhibitor
RhoA = Ras Homolog Family Member A
Robo1 = Roundabout Guidance Receptor 1
RT = room temperature
SHH = Sonic Hedgehog
SMO = Smoothened
SMS = superficial migratory stream
SOX = SRY-Box Transcription Factor
SST = somatostatin
SVZ = subventricular zone
T = Tween
TF = transcription factor
TGF-β = transforming growth factor beta
TTLL = Tubulin Tyrosine Ligase-Like
TUJ1 = Neuron-Specific Class III β-Tubulin
VZ = ventricular zone
WNT = Wingless/Integrated Signaling Pathway

TABLE OF CONTENTS

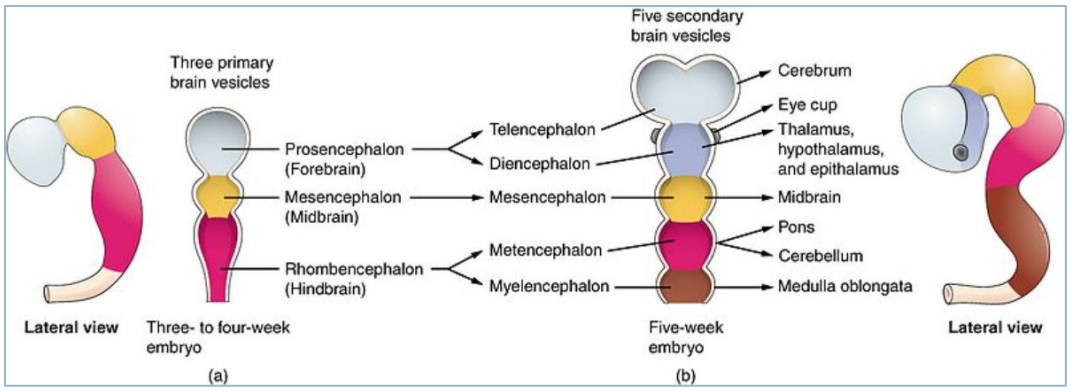

Figure 1 : Development of brain vesicles during mouse embryogenesis. Following neurulation, the rostral neural tube expands to form the three primary brain vesicles (left): the prosencephalon (forebrain), mesencephalon (midbrain), and rhombencephalon (hindbrain). These structures subsequently develop into five secondary brain vesicles. By OpenStax College.

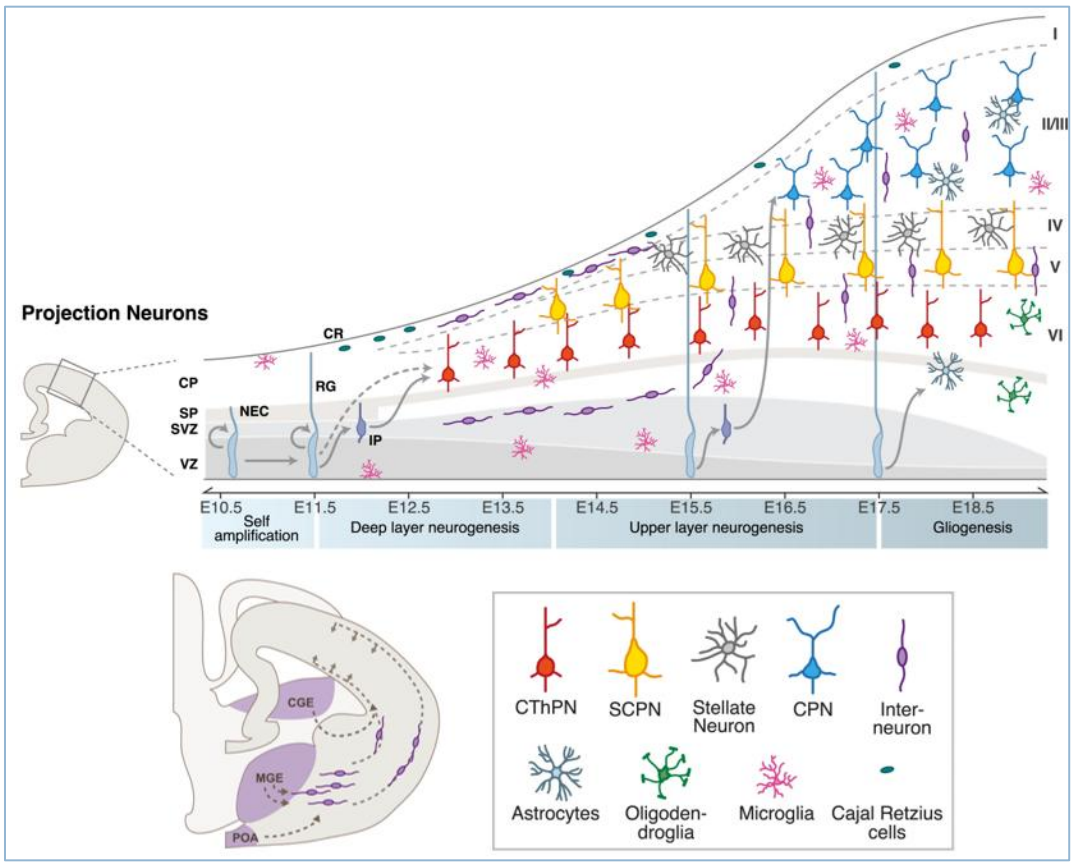

Figure 2 : Origin of cellular diversity in the mammalian cortex Schematic representation of the corticogenesis process in mouse from E10.5 to E18.5. In the ventricular zone (VZ), neuroepithelial cells (NECs) self-amplify and then transition to radial glial cells (RG, light blue) that asymmetrically divide to maintain the progenitor pool, while also producing projection neurons (PNs) directly or indirectly through intermediate progenitors (IPs, light purple) located in the subventricular zone (SVZ). Newborn PNs migrate radially to first form the subplate (SP) and then the sequential layers of the cortical plate (CP) in an inside-out fashion (layers labeled I–VI). Interneurons (purple) originate from ventral progenitor pools including caudal and medial ganglionic eminences (CGE and MGE) and the preoptic area (POA). They first migrate tangentially to access the cortex and then migrate radially to reach their final positions (route indicated with dashed lines). cortical plate, CP: subplate, SP; subventricular zone, SVZ; ventricular zone, VZ; projection neurons, PN; corticothalamic PN (CThPN, red), subcerebral PN (SCPN, yellow), stellate cells (gray), and callosal PN (CPN , blue) adapted from Di Bella et al.[7]

1. INTRODUCTION

1.1. BRAIN DEVELOPMENT

1.1.1. THE ORIGIN OF THE NERVOUS SYSTEM

The formation of the nervous system begins during the second week of embryonic life in human, and at embryonic day 7.5 (E7.5) in mouse embryonic development[1,2]. Three primary germ layers are formed: the endoderm, the mesoderm, and the ectoderm. The latter folds along the midline to form the neural tube, the primordial structure of the central nervous system[1].

The neural tube subsequently differentiates along the anteroposterior axis into three primary brain vesicles: the prosencephalon (forebrain), mesencephalon (midbrain), and rhombencephalon (hindbrain) which further subdivide into five secondary brain vesicles (Figure 1)[1]. The rhombencephalon gives rise to the metencephalon, future pons and cerebellum, and the myelencephalon, future caudal brainstem. The prosencephalon differentiates into the diencephalon, which develops into structures such as the thalamus and the telencephalon[1].

Subsequent patterning of the telencephalon along the dorsoventral axis leads to the formation of the pallium and subpallium. Dorsally, the pallium develops into the future cerebral cortex while ventrally, the subpallium gives rise to transient proliferative structures: the medial ganglionic eminence (MGE), the lateral ganglionic eminence (LGE), and the caudal ganglionic eminence (CGE) and, at the telencephalon-diencephalon boundary, the preoptic area (POA)[3,4]. This dorsoventral patterning is driven by opposing morphogenetic gradients, notably Sonic Hedgehog (SHH) signaling ventrally and bone morphogenic protein (BMP)/Wingless-type (Wnt) signaling dorsally, which will be further introduced in section 1.1.3.[4].

1.1.2. CEREBAL CORTICOGENESIS

Corticogenesis is the process by which neural progenitors generate mature neurons that will form the future cortex, occurring from E10.5 to E18.5 in mice (as illustrated in Figure 2). In the ventricular zone (VZ), neuroepithelial stem cells (NSC, details on progenitors categories can be found in table 1) initially undergo symmetric divisions, promoting self-renewal and expansion of the progenitor pool[1,5,6].

At the onset of neurogenesis, NSCs transition into radial glial cell (RGCs) shifting from symmetric to asymmetric division. Each division produces one self-renewing daughter and one neuroblast committed towards basal progenitors or neuronal differentiation[5]. RGCs are transient cell types

Table 1 : summary of progenitor cells, their location, division mode and the type of cell they become.

Progenitor cells	Main location	Division mode	Cellular fate
Neuroepithelial cells (NECs)	VZ	Symmetric proliferative	Apical radial glia
Radial glia cells (RGC)	VZ	Initially symmetric, later asymmetric	Neuroblasts, IPs, RGCs, Astrocytes, Oligodendrocytes
Outer radial glia cells (oRG)	oSVZ	Self-renewing asymmetric divisions	Neuroblasts, IPs
Intermediate progenitor (IPs)	SVZ	Mostly symmetric neurogenic	Neuroblasts
Neuroblasts	SVZ → CP	Usually post-mitotic	Immature neurons
Immature excitatory neurons	IZ/CP	Post-mitotic	Mature pyramidal neurons
MGE/CGE progenitors	Ganglionic eminences (+PoA)	Symmetric and asymmetric	Interneuron precursors
Interneuron precursors	Ganglionic eminence → cortex	Mainly post-mitotic migration	cINs

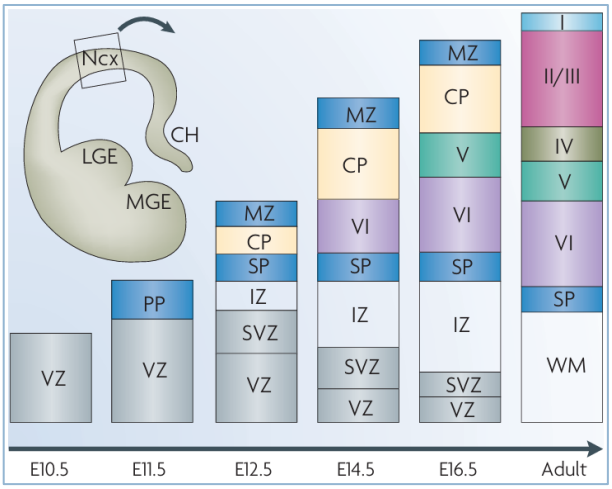

Figure 3 : Chronological apparition of the different layers during the mice neocortex development. Schematic representation of the different layers appearing in the neocortex (Ncx) from embryonic day 10.5 to adult life in mice. At embryonic day (E) 10.5, the neuroepithelium is composed primarily of ventricular zone (VZ) progenitors. The preplate (PP) forms at E11.5 and subsequently splits into the marginal zone (MZ) and subplate (SP) following the arrival of cortical plate (CP) neurons. As corticogenesis proceeds, the subventricular zone (SVZ), intermediate zone (IZ), and cortical plate become progressively established. Deep-layer neurons (layer VI followed by layer V) are generated first, whereas upper-layer neurons (layers II/III and IV) are produced later, resulting in the characteristic inside-out pattern of cortical development. The schem on the left illustrates the embryonic telencephalon, highlighting the neocortex (Ncx), lateral ganglionic eminence (LGE), and medial ganglionic eminence (MGE). [37]

whose soma remain in the VZ while extending long fibers to the pia guiding the migration of newly born projection neurons (PNs)[7] [8].

RGCs can divide asymmetrically directly into PNs or indirectly through the formation of intermediate progenitors (IPs). In the indirect pathway, RGCs first produce IPs, which subsequently undergo additional rounds of division before differentiating into PNs, thereby amplifying neuronal output[8,9]. As corticogenesis progresses, progenitors sequentially generate distinct PN subtypes characterized by specific transcriptional programs, cortical layer identities, connectivity patterns, and functional properties (as described in section 1.2.1.) [7].

Following cell cycle exit, neuroblasts migrate from the VZ through the subventricular zone (SVZ) to form the intermediate zone (IZ), under the marginal zone (MZ). Cells within the IZ are post-mitotic and represent immature neuronal precursors. Later in embryonic development, they migrate along radial glial fibers toward the inner surface of the MZ where they accumulate to form a densely packed cellular layer known as the cortical plate (CP), a transient structure that will later give rise to the mature cerebral cortex[8,10].

Cortical neurogenesis follows a precise chronological organization that leads to the formation of distinct cortical layers through a process known as “inside-out layering” (as illustrated in Figure 3). Early-born neurons settle in the deep cortical layers (layers VI and V), whereas later-born neurons migrate past these earlier populations to establish the superficial layers (layers II–IV)[11]. The radial migration of PN is regulated by Reelin, an extracellular matrix glycoprotein secreted by Cajal-Retzius cells located in the MZ[12,13]. In the absence of this protein, PNs cannot reach their *ad hoc* final position [7,12]. At later stages (E17.5 in mice), radial glia cells transition to a gliogenic phase, during which they generate various types of astrocyte precursors and finally transform into astrocytes as well as oligodendrocytes [14].

The mature cortex is organized into six layers. Each layer is characterized by the presence of specific neuronal subtypes with distinct connectivity and functional roles. Layer I corresponds to the molecular layer mostly filled with axons, layers II and IV are respectively the extern and inner granular layers, layers III and V are respectively extern and inner pyramidal layers, and layer VI contains polymorphous cells. The establishment of these layers and their associated neuronal subtypes is essential for the functional organization of the cerebral cortex (Figure 3) [15].

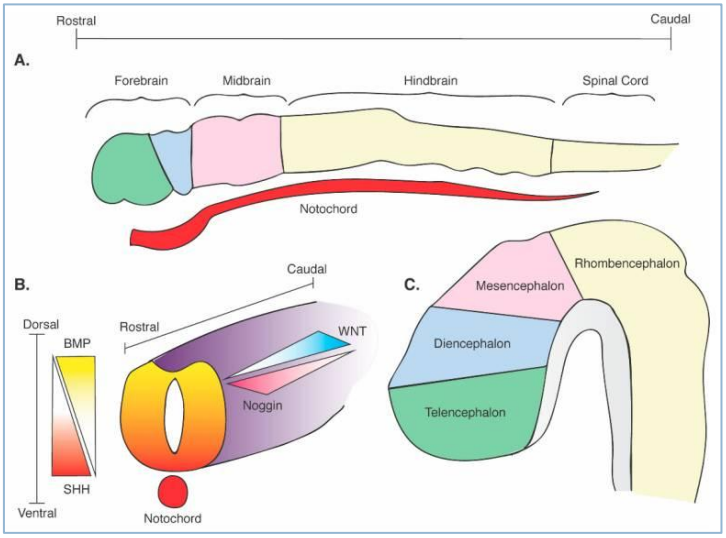

Figure 4: Schematic of neural tube formation and cerebral regional identity. (A) Regional definition of the neural plate with rostrocaudal axes and its contact with the SHH-releasing notochord. (B) Formation of the neural tube and its contact with the SHH-releasing notochord. Dorsoventral and rostrocaudal axes are defined with corresponding critical morphogenetic gradients: dorsal BMP; ventral SHH; rostral noggin; caudal WNT). (C) Development of the embryonic brain and divisions of the central nervous system. [16]

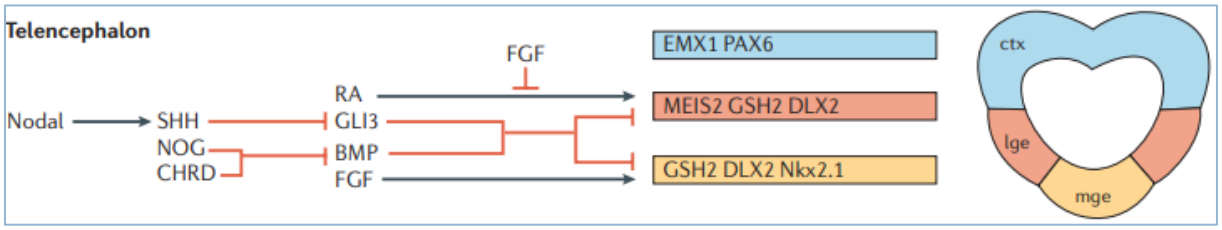

Figure 5 : Morphogenic signalling pathways involved in telencephalon patterning. The telencephalic vesicles are regionalized into the dorsally located cerebral cortex, the intermediate LGE and the most ventrally located MGE, each of which expresses a distinct combination of transcription factors. BMP signals and the repressor form of GLI3 inhibit specification of the LGE and the MGE: these repressors are counteracted by NOG/CHRD and SHH, respectively. Nodal signals also act upstream of SHH. RA controls LGE specification, whereas FGF antagonizes the action of RA and induces mge characteristics. DLX2, distal-less homeobox 2; EMX1, empty spiracles homologue 1 (Drosophila); GSH2, genomic screened homeobox 2; MEIS2, myeloid ecotropic viral integration site 1 homologue 2.[15]

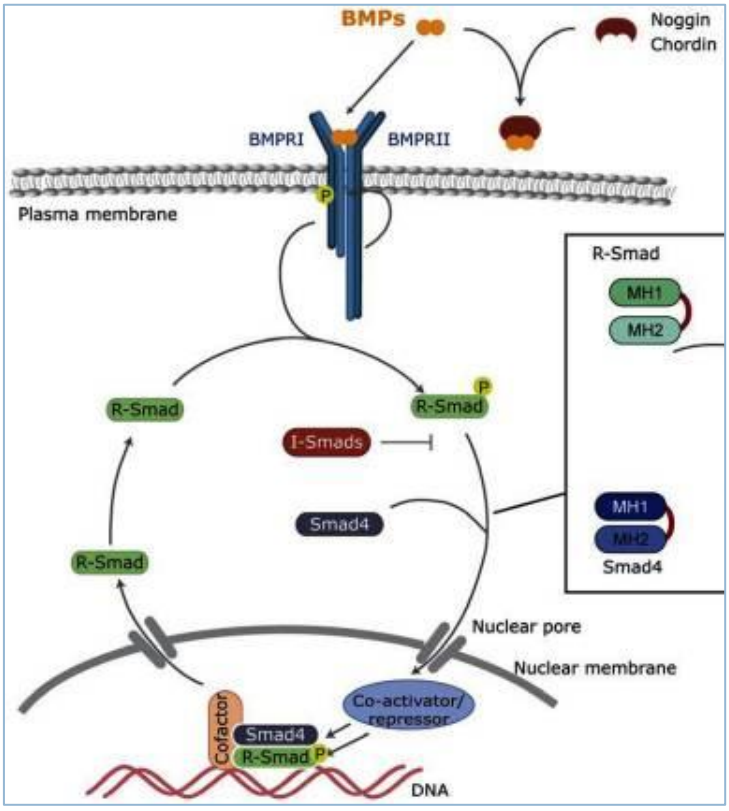

Figure 6 : Canonical BMP signaling. Schematic representation of the BMP signaling pathway. BMPs bind to the BMP receptors type I and II, and then BMP receptor phosphorylates and activates itself. Activated receptor phosphorylates R-Smads, which associate with Smad4 and enter the nucleus, where they regulate transcriptional processes. BMP signaling can be inhibited by extracellular antagonists, such as Noggin.

1.1.3. PATTERNING OF THE BRAIN

The dorsoventral patterning of the neural tube relies on opposing gradients of ventralizing and dorsalizing signals. Several pathways are involved in this patterning, principally SHH, BMP and Wnt pathways. They activate downstream factors that enable cells to acquire their final identity and position[4].

SHH is the principal ventralizing morphogen, initially secreted by the notochord and later by the floor plate (Figure 4A), forming a ventral to dorsal gradient. SHH acts by binding to its receptors Patched (PTCH1) and Smoothened (Smo). Normally, PTCH1 binds to and represses Smo, keeping the pathway inactive and preventing the activation of the glioma-associated oncogene homolog (GLI). When SHH binds to PTCH1, Smo is released, GLI becomes activated and translocates to the nucleus to activate gene expression[4]. This induces ventral neural identities in a concentration dependent manner (Figure 4B). The concentration gradient is translated into graded GLI activation: high SHH levels promote GLI activator forms, inducing the expression ventral transcription factors (TFs) such as NKX2.1, which specifies MGE identity [16–18] (Figure 5).

In contrast, BMPs, members of the transforming growth factor-β (TGF-β) family, are secreted from the neuroectoderm and promote dorsal neural identities[19]. BMP binds to type I and type II receptors, triggering phosphorylation of SMAD1/5/8 (Sma- and Mad-related proteins). Phosphorylated SMAD1/5/8 associates with SMAD4, and the resulting complex enters the nucleus to promote dorsal patterning by decreasing ventral gene expression (e.g. *SHH*). BMP activity is antagonized by secreted inhibitors such as Noggin, expressed in the notochord (Figure 4B and 6) [18,19]. SHH and BMP pathways are therefore acting as opposing signals: SHH represses dorsal identities ventrally while BMP inhibits ventral fates dorsally.

Furthermore, WNT reinforces dorsal identity. In the absence of WNT, the β-catenin is linked to a complex made of adenomatous polyposis coli (APC), Axis Inhibition Protein (AXIN) and glycogen synthase kinase 3 beta (GSK3b) leading to its degradation. When WNT is present, it binds to Frizzled receptors and low-density lipoprotein receptor-related protein (LRP) 5/6 co-receptors. The destruction complex is inhibited, allowing β-catenin to accumulate, translocate to the nucleus, and activate genes associated with dorsal cortical identity such as *empty spiracles homeobox 2* (*EMX2*) (Figure 7) [20,21].

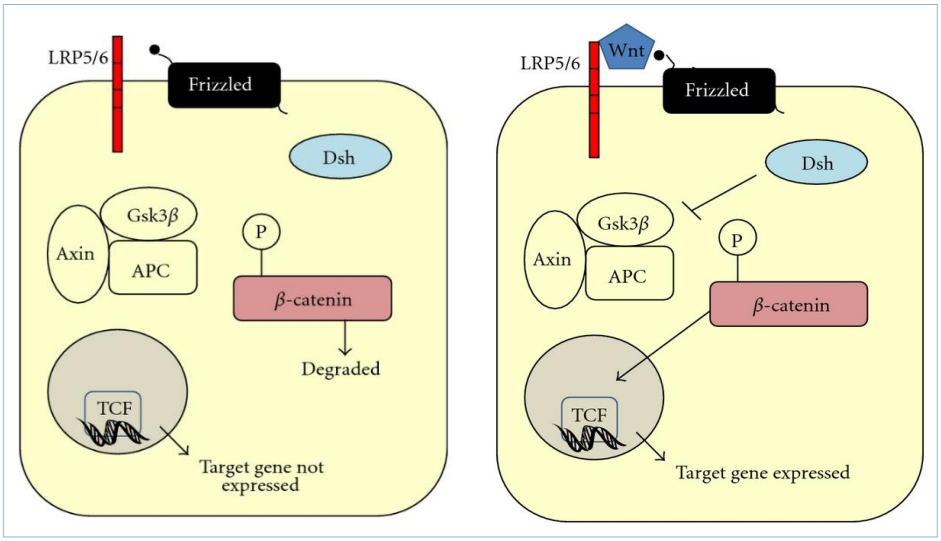

Figure 7 : The canonical Wnt pathway for target gene expression. Left. When a WNT ligand is absent, β-catenin is phosphorylated by the Gsk3β complex and is targeted for degradation and there is no gene expression. Right. When a Wnt ligand binds Frizzled, Dsh is activated and inhibits the axin-Gsk3β complex phosphorylating β-catenin enabling it to translocate to the nucleus and can activate TCF which can activate gene expression. Abbreviations: APC: adenomatous polyposis coli, Dsh: Dishevelled; GSK3β: glycogen synthase kinase 3 β; TCF: T-cell factor. [4]

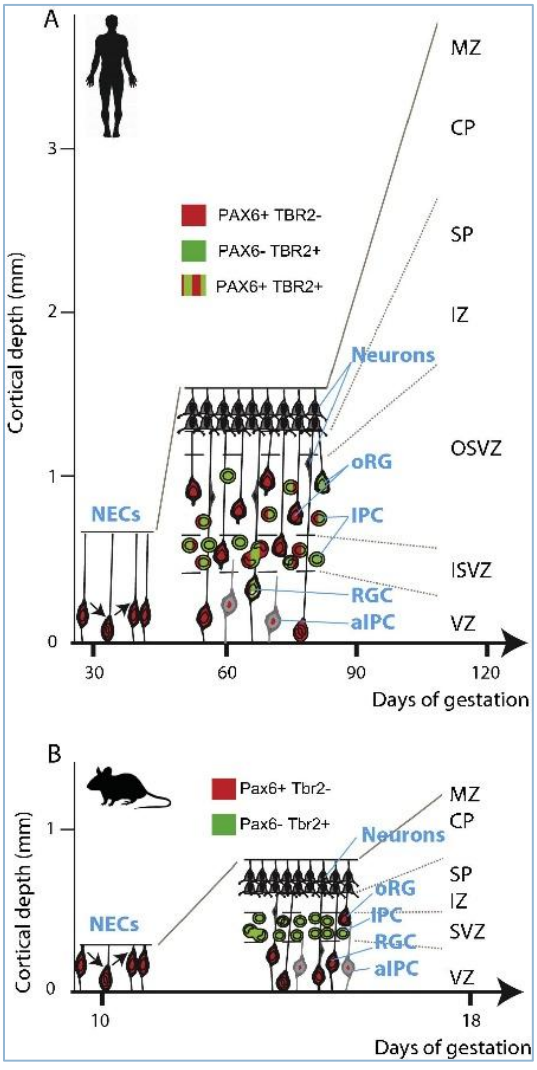

Figure 8 : Comparison of human and mouse cortical development. Diagrams of sections through the depth of the developing cortex of (A) humans and (B) mice showing the major progenitor types and whether they express the transcription factors PAX6/Pax6 and/or TBR2/Tbr2. Mouse corticogenesis occurs over a much shorter period of time than human corticogenesis. MZ, marginal zone; CP, cortical plate; SP, subplate; IZ, intermediate zone; OSVZ, outer subventricular zone; ISVZ, inner subventricular zone; VZ, ventricular zone; SVZ, subventricular zone; NECs, neuroepithelial cells; oRG, outer radial glia; IPC, intermediate progenitor cell; RGC, radial glial cell; aIPC, apical intermediate progenitor cell. [24]

1.1.4. COMPARISION BETWEEN MOUSE AND HUMAN CORTICOGENESIS

Brain development in human and mouse undergoes the same major developmental steps (*e.g.* proliferation, neurogenesis, migration, ...), yet significant differences have been identified in terms of timing, cellular organization and complexity [22].

The human brain is large and gyrencephalic with an expansion of the neocortex. It includes approximately 16.3 billion cortical neurons. On the other hand, the mouse brain is lissencephalic and contains 14 million cortical neurons [23]. Regarding morphogenesis, corticogenesis is prolonged in humans, spanning a long period, from gestational week (GW) 8 to GW26, as compared to mice where this process occurs between E10.5 to E18.5[23].

One significant difference between species concerns progenitor populations in the cortex. In both humans and mice, NECs in the VZ transition into RGC, which generate neurons directly or through IPs in the SVZ. However, humans develops two subventricular proliferative layers : the inner SVZ (iSVZ) and the outer SVZ (oSVZ)[24]. Outer radial glia cells (oRGs), located in the oSVZ, are found in humans and constitute about half of all progenitors present in the oSVZ but account for only a minute fraction of the SVZ progenitors (Figure 8) [24]. Similarly, truncated radial glia, progenitors lacking apical processes, are present in gyrencephalic species absent in mice. This expansion of basal progenitor types and numbers amplifies neuronal output contributing to PN diversification[7].

Regarding the cINs, in mice they originate from the MGE, CGE and POA and migrate tangentially to reach the developing cortex. In human, while most cINs also originate from these transient proliferative regions, several studies suggest that a between 4 and 9% are also produced dorsally within the progenitor layers of the cortex during the second half of the corticogenesis (between GW20 to GW24)[24–26]. Although the main cIN subtypes are broadly conserved between species, there are key differences in the developmental timing and subtype ratios. The relative number of cINs to PNs is higher in human compared to mice, with a 20:80 ratio in mice compared to a 30:70 ratio in humans[27]. Furthermore, in the mouse cortex, parvalbumin cINs (PVs) constitute the dominant mature population (40%) derived from MGE with somatostatin cINs (SST) that represent a smaller fraction (30%)[28]. In humans the proportion of PV and SST is not clearly define but varying between layers in comparison with mice[27,29]. Human cortical development also differs from rodents, as corticogenesis is protracted in time and leads to an expanded and structurally more complex cortex. This prolonged developmental window and increased spatial scale impose additional constraints on human cIN migration, requiring interneurons to navigate longer

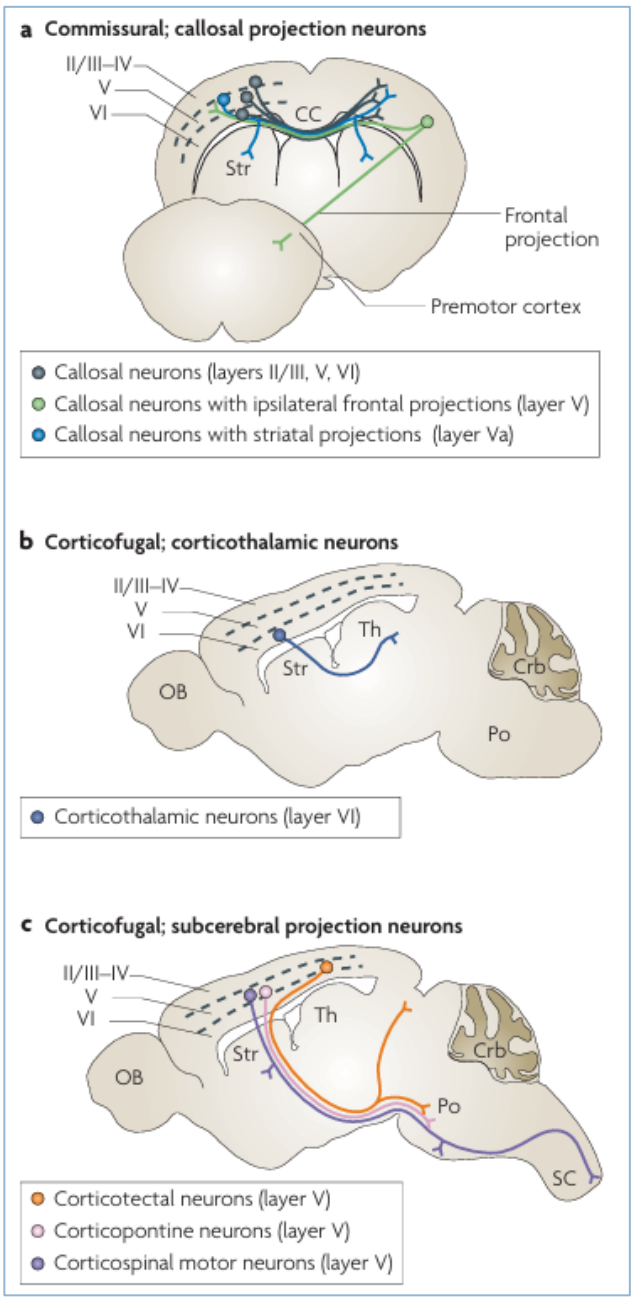

Figure 9: ***Major subtypes of projection neuron in the neocortex****. There are three basic classes of cortical projection neuron: associative, commissural and corticofugal. A. Commissural projection neurons Neurons that extend axonal projections within the cortex to the opposite hemisphere via the corpus callosum or the anterior commissure. B-C. Corticofugal projection neurons Neurons that extend axonal projections 'away' from the cortex. These include subcerebral projection neurons and corticothalamic neurons.*[37]

distances within a dynamically changing environment and to coordinate their migration with extended periods of cortical maturation[30,31]. Moreover, although cell types are homologous across species, their genetic profiles differ[32] and recent transcriptomic studies have revealed human-specific gene expression programs in developing cINs. However, how whether this translates into differences in migratory behaviors between species remains largely unknown[33,34].

1.2. NEURONS

The cerebral cortex is primarily composed of two major neuronal populations. The excitatory PNs originate from the dorsal telencephalon and migrate radially to reach the CP. The cINs originate from the MGE, CGE and POA and migrate tangentially toward the developing cortex before reaching their final positions through radial dispersion[35]. Defects in neuronal migration can lead to neurological disorders as it can result in improper positioning, altered neuronal connectivity or reduced synapse formation. Such defects have been associated with intellectual disability, autism spectrum disorders, and schizophrenia among others[36,37]. Moreover, maintaining the excitation-inhibition balance is critical for cortical circuits, disruptions of this balance may lead to disorders such as epilepsy[38].

1.2.1. PROJECTION NEURONS

PNs are glutamatergic excitatory neurons and account for approximately 70% of cortical neurons in mice[39]. They migrate radially to reach the CP with deep layer neurons (V-VI) followed by superficial layer neurons (II-IV), following the inside-out pattern (see also in 1.1.2. Neurogenesis). They are classified according to their connectivity into three main categories: callosal PNs, corticothalamic PNs, and subcerebral PNs (Figure 9)[40].

Beyond this projection-based classification, PNs display a high degree of heterogeneity and can be further subdivided according to their molecular identity, morphological features, and electrophysiological properties. Single-cell transcriptomic and multimodal profiling approaches have revealed numerous molecularly distinct PN subclasses defined by the expression of specific marker genes, including layer-specific and projection-specific populations[41,42]. In addition, morphological characteristics such as dendritic architecture, axonal branching patterns, and soma location, together with intrinsic electrophysiological properties including firing patterns, adaptation, and membrane properties, allow the identification of finer neuronal subclasses[43].

Callosal PNs are pyramidal neurons. They are mainly located in layers II/III, V, and VI, that extend axons through the corpus callosum to connect the two cerebral hemispheres without projecting outside the telencephalon[40].

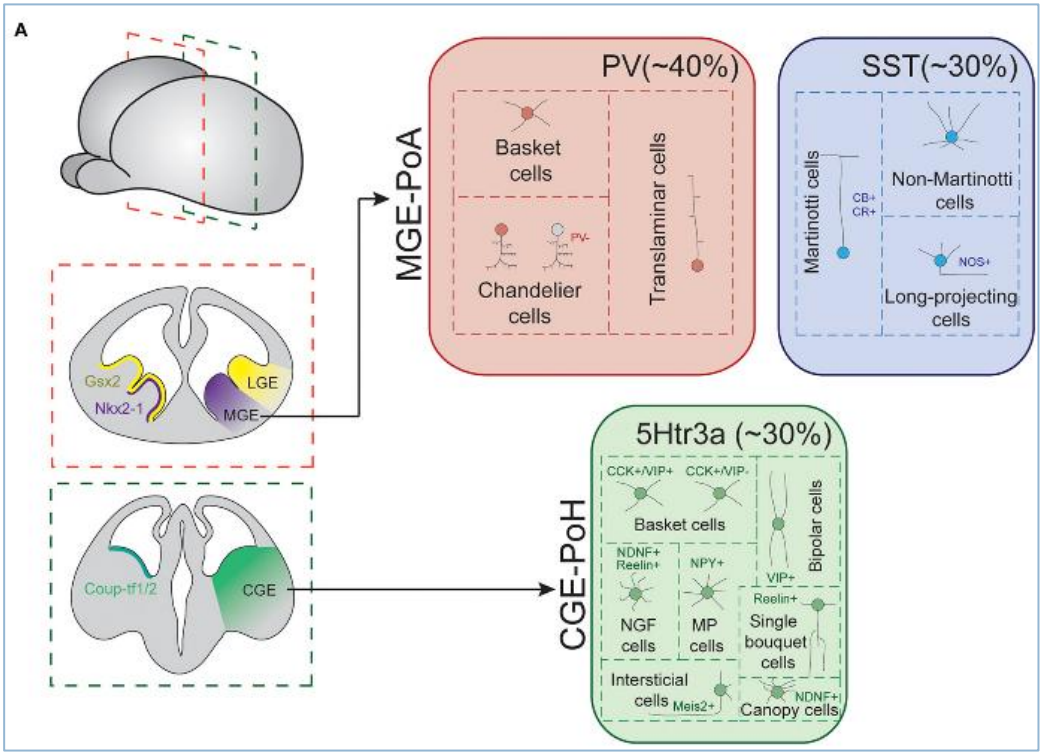

Figure 10 : Fate specification of cINS. MGE and PoA generate PV and SST interneurons. CGE generate all types of 5HT3R interneurons.

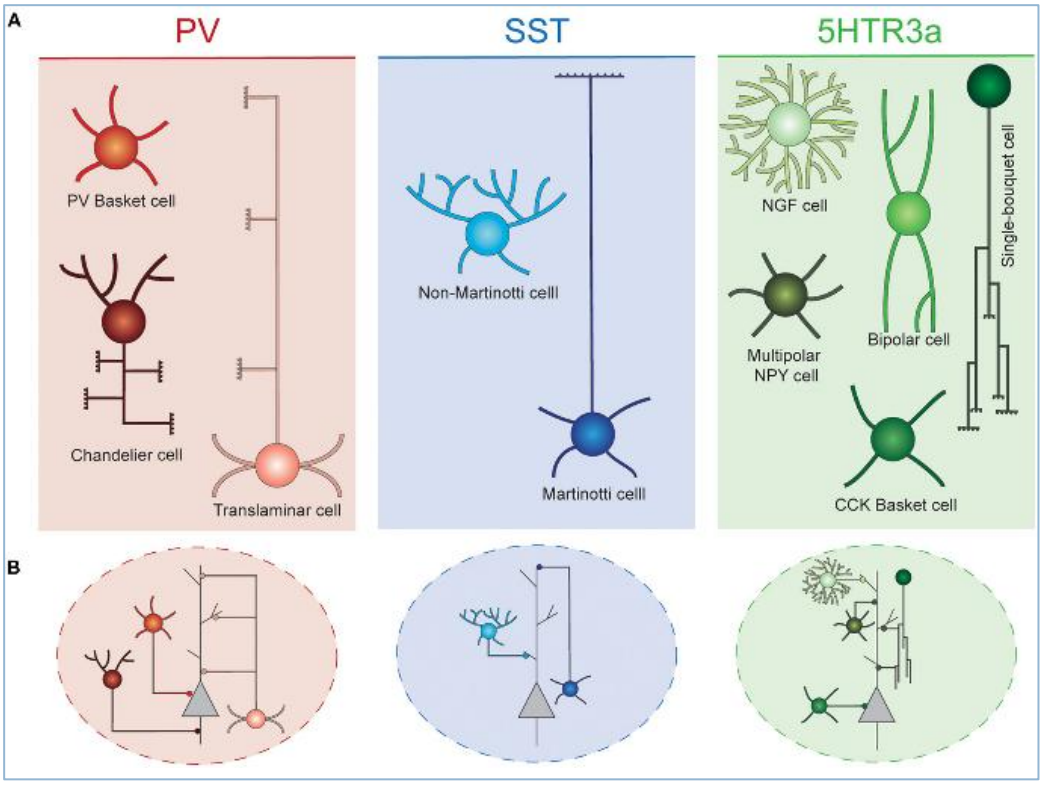

Figure 11 : Interneuron diversity in the neocortex. A. Cortical interneurons can be classified into three main classes: PV, SST and 5HT3R. Each can be subdivided into different subtypes. B. The different types preferentially target specific compartments of the target cell.

Corticothalamic PNs, mainly located in layer VI, project from the cortex to various thalamic nuclei. Subcerebral PNs, pyramidal neurons located primarily in layer V, project to subcortical targets such as the brainstem and spinal cord [40].

The specification of PNs is regulated by TFs, including EMX2[44], PAX6[45], LHX2[46], and FOXG1[47]. Loss of any of these TFs leads to severe developmental cortical malformation or missing brain structures[48–51].

1.2.2. CORTICAL INTERNEURONS

The cINs are gamma-aminobutyric acid-ergic (GABAergic) inhibitory interneurons accounting for approximately 30% of cortical neurons in mice[35]. They originate from the ventral telencephalon, particularly from the MGE (~50-60%), CGE (30%) with a smaller contribution from the POA (~10%)[35]. They reach the developing cortex through long-distance tangential migration. In contrast, the LGE primarily gives rise to striatal GABAergic neurons and does not contribute to the cIN pool[35] (Figure 10).

In the mouse neocortex, three major cardinal classes of cINs have been described: the parvalbumin-expressing, somatostatin-expressing, and 5HT3 receptor–expressing (5HT3R) cINs. Each class contains several subtypes and targets distinct subcellular compartments of PNs[35,52] (Figure 11A). Each subclass of cINs comprises more refined subtypes of interneurons with unique morphological, electrophysiological and transcriptional (met) properties [32]. The identity of cINs is largely determined by their spatial origin within the ventral telencephalon. While MGE-derived cINs predominantly acquire PV and SST identity, CGE produces 5HT3R cINs [52].

Using a multimodal approach combining single-cell transcriptomics, electrophysiological recordings, and morphological reconstructions, Gouwens et al. further classified cortical GABAergic interneurons into 28 met-types. These met-types integrate molecular identity with neuronal morphology and intrinsic electrical properties, providing a more comprehensive description of interneuron diversity. PV met-types mainly include fast-spiking basket and chandelier cells that preferentially inhibit the perisomatic region of PNs, whereas SST met-types, including Martinotti cells, primarily target dendritic compartments and regulate dendritic integration. HTR3A-related met-types, including Vip-expressing interneurons, contribute to the modulation of cortical circuits through local inhibition and disinhibitory mechanisms. This multimodal classification highlights the functional diversity of cINs and emphasizes that their identity cannot be defined solely by transcriptomic signatures but also relies on their morphological and electrophysiological properties[53].

PV cINs account for approximately 40% of cINs and include chandelier cells and basket cells, targeting the axon initial segment or the soma of pyramidal neurons. SST cINs represent about 30% of CINS and include Martinotti cells, which mainly target distal dendrites, non-Martinotti cells and long projecting cells. The remaining 5HT3R CINS (~30%) are multipolar cells located mainly in the superficial cortical layers[35,52] (Figure 10-11B).

Researchers are still debating whether cIN subtype identity is determined intrinsically or shaped by environmental cues. Three complementary models have been proposed to explain interneuron diversification. In the highly predetermined model, subtype identity is largely encoded by intrinsic molecular programs established in progenitor cells, with limited influence from external cues. In contrast, the environmental refinement model suggests that progenitors acquire an early bias toward specific fates, but that extrinsic signals encountered during migration and maturation, such as cortical activity and local cellular interactions, further refine their final identity[54]. Indeed, progenitors from different interneuron classes display molecular differences at cell-cycle exit, while changes in the extracellular environment can alter subtype proportions[55]. Finally, the contraction model proposes that interneuron diversity is generated through the production of transient populations, followed by selective stabilization or elimination of specific cell types during development, a mechanism particularly proposed for long-range interneurons[54].

1.2.3. INTERNEURON MIGRATION

As said earlier, when cINs start their migration, they exit their progenitor zones and initiate tangential migration toward cerebral cortex[56]. During this process, cINs migrate tangentially from the ganglionic eminences to the developing neocortex through defined routes, including the superficial and deep migratory streams (SMS and DMS). They subsequently enter cortical compartments such as the MZ, IZ, and VZ, where they continue their migration before reaching their final positions[56,57]. Once they reach their final destinations, cINs switch to radial migration in order to settle within the appropriate cortical layer[58].

cIN migration proceeds through saltatory migration, characterized by alternating phases of movement and pause. The migration cycle begins with cINs extending their leading process and branching to evaluate the surrounding environment. Then, the leading process retracts, a somal swelling then forms, into which the Golgi apparatus and centrosome relocate from the

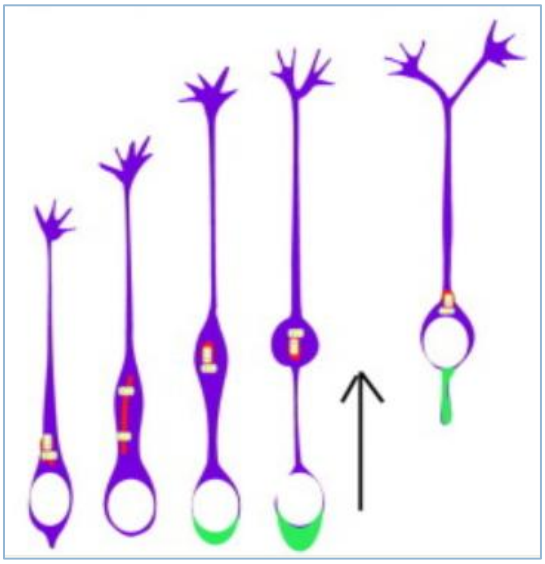

Figure 12 : Schematic representation of nucleokinesis in MGE cells. After the resting phase of the nucleus (white), the centrioles (yellow) and Golgi apparatus (red) migrate forward, and the leading neurite elongates. Then, myosin II accumulates at the rear of the cell body (green) and pushes the nucleus toward the centrosome/Golgi apparatus through actomyosin contraction.

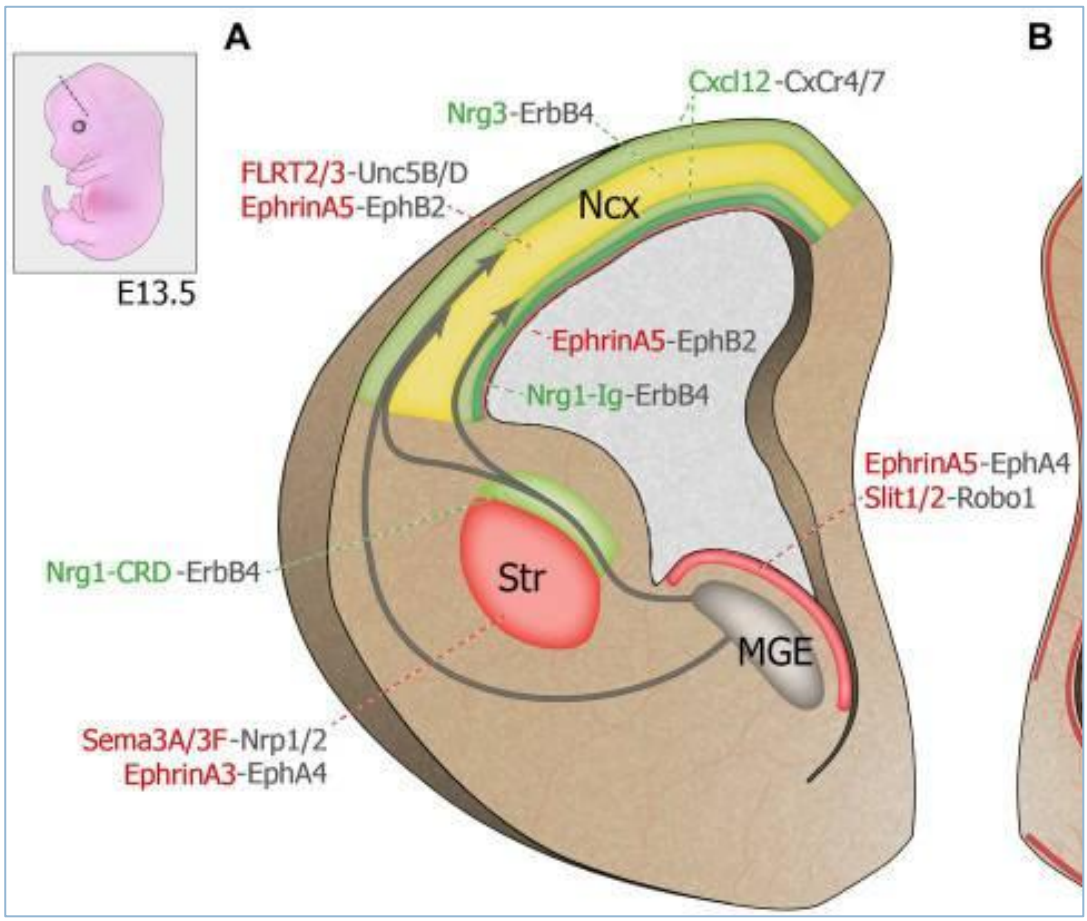

Figure 4 : Molecular regulation of cortical interneuron migration. Top left corner: Representation of an E13.5 mouse embryo. Dash line illustrates the coronal plane through the telencephalon. Schematic representation of a coronal hemi-section (left) highlighting the chemorepulsive (red) and chemoattractive (green) molecules guiding MGE-derived INs migrating towards the developing cortical plate. The cortical plate hosts both chemoattractive and chemorepulsive cues and is represented in yellow. [53]

saltatory motion of the cell. The trailing process then retracts and the cIN pauses, allowing the cycle to restart [59] (Figure 12). Belion et al. showed that myosin II accumulates at the rear of the soma in migrating cINs. Inhibition of myosin blocks the long distance translocation of the nucleus confirming that the contraction of the actomyosin system is necessary to push the nucleus forward during the migration cycle[59]. The contraction of actomyosin is regulated by extracellular signals important to generate force for the cell movement. Post-translational modifications (PTMs) of actors in the contraction, such as the myosin light chain kinase (MLCK), play also an important role in the regulation of the contraction and therefore of the migration as their absence is associated with neuronal migration defects [60].

1.2.4. MOLECULAR REGULATION OF INTERNEURON MIGRATION

CIN migration is guided by a combination of chemoattractive and chemorepulsive signals (Figure 13). These signals are either diffusible molecules secreted by surrounding cells or membrane-bound cues that require contact[35,59].

Within the subpallium, repulsive signals direct cINs away from ventral regions, preventing them from remaining in their progenitor zones. Different cues act at different timings of tangential migration. Firstly, to exit the GE, the diffusible cues Slit homologs 1 and 2 (Slit1 and 2) are expressed by the VZ and SVZ and repulse cINs by the intermediary of Slit receptor roundabout homolog 1 (Robo1), directing their initial tangential migration away from the ganglionic eminence[61]. Ephrin molecules are also expressed in the VZ and promote the repulsion of cINs expressing the EphA4 receptor[61]. Other factors such as hepatocyte growth factor (HGF), brain derived neurotrophic factor (BDNF) and as well as neurotrophins (NT) also promote the cIN migration [61]. Molecules such as Semaphorin 3A and 3F expressed in the striatal mantle as well as Ephrin A3, express by striatal cells, prevent cINs to pass through the striatum [62].

Upon approaching the neocortex, chemoattractives molecules from the developing cortex create a permissive corridor for migrating cINs by providing attractive signals, including neuregulin-1 (Nrg1)[63], GABA[64], and C-X-C motif chemokine ligand 12 (CXCL12)[65], promoting entry into the cortical environment. Nrg1 is a protein that contains an epidermal growth factor-like domain. There are two isoforms expressed by the telencephalon, a membrane-bound express along the route follows cINs toward the cortex one and a secreted one produced in the pallium. Their combined activity act as a short- and long-range attractants, respectively via the activation of the neuregulin receptor Erbb4 expressed by cINs[66]. CXCL12 is a chemokine secreted by the IPs that

attract cINs towards the cortex by linking to C-X-C motif chemokine receptor 4 (CXCR4). While entering the cortex, cINs also release diffusible cues that regulate the proliferation of IPs and therefore the excitatory/inhibitory balance[67].

When migrating towards the cerebral cortex, cINs can integrate either one of the migratory stream, the SMS going through the MZ or the DMS going by SVZ [68,69]. A third migratory stream passing by the subplate appears un mice between E15 and E16[61]. Whether cIN stream allocation is governed by extrinsic cues or intrinsic regulation remains largely unknown. It seem that cINs migrate through a stream based on the diffusible cues they receive but also that they respond differently depending on their differential gene expression profile, such as expression of guidance receptors[61]. Studies have shown that EphB2/EphrinA5 signaling maintains the two streams distinct, with EphrinA5 confining EphB2-expressing CINS to the DMS. Once in the appropriate cortical layer, cINs must stop migrating, a process likely achieved by extrinsic stop signals secreted by cortical cells, whose identity remains unknown[61].

In addition to these extrinsic cues, cIN migration is regulated by intrinsic molecular mechanisms controlling cytoskeletal dynamics and nucleokinesis[61]. These mechanisms involve signaling molecules, TFs, neurotransmitters receptor and factors controlling the cytoskeletal remodeling. Distal-less homeobox (DLX) 1 and 2 are TFs necessary for the exit of cINs from the MGE, as their loss results in the accumulation of cINs[70,71]. Rho-GTPases, such as Ras homolog family member A (RHOA), regulate cytoskeletal dynamics during migration[72,73], while others, including Lissencephaly 1 (LIS1)[74] and Doublecortin (DCX)[75] are also essential for proper cINs migration. In addition, cIN migration is modulated by the neuronal excitability through the activation of ligand-gated ion channels, including GABA and glutamate receptors. Indeed, polarization of receptors by their respective neurotransmitters stimulate cINs motility[76,77]. The balance between intrinsic and extrinsic signals ensures proper directionality and efficiency of cINs migration.

1.2.5. SYNAPTOGENESIS AND CIRCUIT FORMATION

Upon reaching their final positions, cINs extend axons and dendrites and establish connections with their synaptic partners (*i.e.* other cINs, PNs)[35,78,79]. Axonal growth is guided by a specialized structure called the growth cone, which detects extracellular matrix components[80] as well as secreted or membrane-bound guidance signals from target cells[35,81].

The growth cone contains actin filaments within its peripheral domain, allowing rapid cytoskeletal remodeling[82]. Axonal growth direction is controlled by attractive signals (e.g. netrins) and repulsive cues (e.g. Semaphorin 3A), which respectively promote actin polymerization or

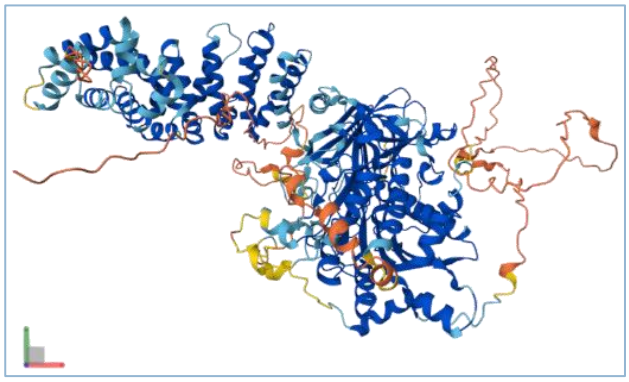

Figure 54: Predicted 3D structure of CCP1. Protein structure retrieved from UniProtKB (accession Q4U2V3), visualized using AlphaFold. Color coding represents positional confidence scores from high (blue) to low (orange/red).

depolymerization[83–85]. Through these mechanisms, cINs identify their appropriate targets and establish functional synaptic connections[82]. Microtubules also contribute to axon guidance by dynamically extending into the peripheral domain of the growth cone, where their stabilization following attractive cues promotes directional axon extension, while repulsive signals can induce microtubule destabilization and growth cone collapse[86].

During early postnatal development, a significant proportion (around 30%) of cINs are eliminated through programmed cell death, ensuring that only appropriately integrated neurons remain within cortical circuits[87,88]. Synaptogenesis and circuit maturation continue during the juvenile period, refining the connectivity between cINs and PNs[89,90].

Mutations affecting these regulatory mechanisms can lead to neurodevelopmental disorders such as anxiety, depression or autism[91,92]. A concreate example is defect in CCP1 protein, which is a protein that influence cytoskeletal dynamics and neuronal migration[60].

1.3. CCP1

Alongside the different factors involved in cIN migration, microtubule dynamics is an important one in the neuronal development[93]. As explained in 1.2.3., neuronal microtubules are regulated by several PTMs, including tubulin polyglutamylation. Polyglutamylation levels are balanced by the opposing activities of glutamylases and deglutamylases[60]. Tubulin polyglutamylation is dynamically regulated by opposing activities of TTLL glutamylases and cytosolic carboxypeptidases (CCPs). Six CCP subtypes exist (CCP1–6), all expressed in neurons but with distinct expression profiles and roles[94]. TTLL enzymes control glutamate chain addition, with TTLL4 acting mainly as an initiase on β-tubulin, TTLL7 functioning as both an initiase and elongase, while TTLL5 initiates glutamylation on α-tubulin and TTLL1/6/11/13 mediate chain elongation[95–97]. Conversely, CCP enzymes regulate glutamate chain length: CCP1/2/3/4/6 shorten polyglutamate chains on both α- and β-tubulin, whereas CCP5 specifically removes the branch-point glutamate. In addition, several CCPs can generate irreversible α-tubulin C-terminal truncations (Δ2- and Δ3-tubulin) following prior detyrosination by vasohibin (VASH)/small vasohibin binding protein (SVBP) complexes[60,98,99].

CCP1 (Figure 14) is the principal deglutamylase in cINs, responsible for both removing genetically encoded C-terminal glutamate residues from tubulin and shortening post-translationally added polyglutamate side chains. This protein is particularly observed in the growth cone and around the nucleus but also detectable in the leading process of migrating cINs [60].

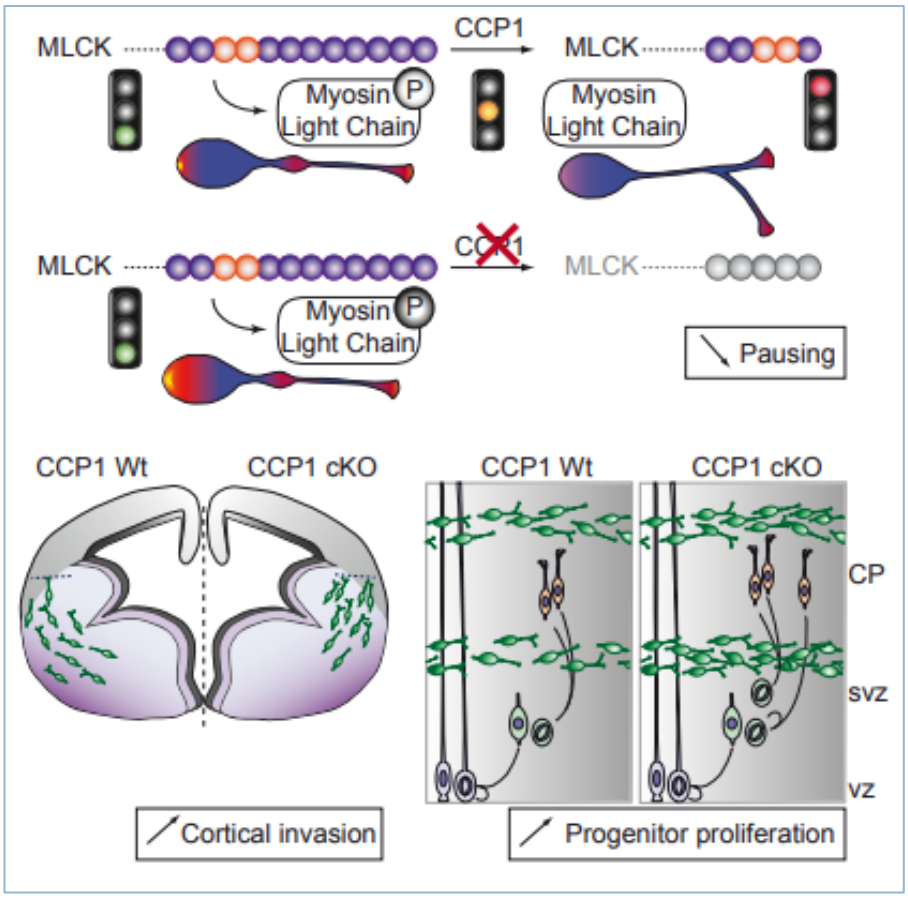

Figure 15 : Effect of CCP1 in MLCK activity. (Top) CCP1 deglutamylates the C-terminal polyglutamate tail of MLCK, enabling proper MLC phosphorylation and actomyosin-driven nucleokinesis, which underlies the characteristic pausing behaviour of saltatory migration. In the absence of CCP1, MLCK becomes hyperglutamylated and its kinase activity is impaired, reducing MLC phosphorylation and nucleokinesis amplitude, resulting in a more continuous migratory pattern with reduced pausing. (Bottom left) Coronal brain sections comparing CCP1 wild-type and conditional knockout (cKO) mice, showing increased cortical invasion by interneurons in the cKO condition. (Bottom right) Schematic of cortical layers (CP, SVZ, VZ) illustrating that the premature cortical accumulation of interneurons in CCP1 cKO animals is associated with increased proliferation of intermediate progenitors in the SVZ[48].

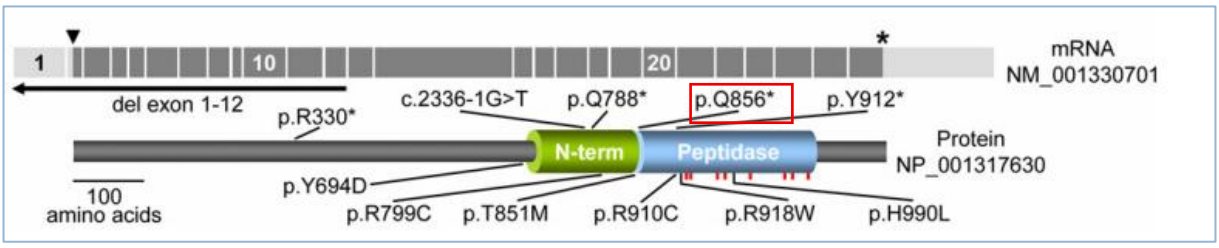

Figure 16 : Schematic representation of the mRNA (exons 1–26), the encoded CCP1 protein, and positions of disease-associated variants. Arrowhead: ATG start codon, asterisk: stop codon. Peptidase: carboxypeptidase domain, N-term: conserved N-terminal domain, red bars: localizations of residues required for CCP1 substrate binding and catalytic activity, in the red rectangle: mutation of interest.[79]

CCP1 plays an important role in neuronal migration and cytoskeletal dynamics[60]. More specifically, CCP1 regulates the activity of MLCK by processing its C-terminal polyglutamate tail[60]. The polyglutamylation level of MLCK influences its kinase activity and therefore the phosphorylation level of myosin light chain (MLC). Under physiological glutamylation level, MLCK progressively phosphorylates MLC causing tension to build within the cell. Once phosphorylation reaches a certain threshold, a contraction of the actomyosin behind the nucleus is triggered resulting in the nucleokinesis event of the migration cycle. The activity balance between CCP1 and the opposing TTLL (TTL1) glutamylase controls actomyosin contractile force, regulating nucleokinesis pauses and the characteristic saltatory mode of neuronal migration [60,100] (Figure 15).

In case of *Ccp1* invalidation, MLCK becomes hyperglutamylated. Consequently, MLCK is no longer able to properly phosphorylate MLC, impairing its function. This leads to consequences of short- and long-term modifications. Indeed, it leads to shorter pauses and reduced nucleokinesis amplitudes, shifting cINs from a saltatory motion to a more continuous one. Despite a similar average migration speed, the of migration cINs becomes more coordinated, causing them to reach the cortex earlier and in greater numbers the lateral cortex.[60] This alteration of migration dynamics results in a higher number of cINs in the cortex at a given timepoint, even though the final number of cINs at the end of the development remains the same. The premature arrival of cINs promotes increased proliferation of IPs through yet unknown external diffusible cues, thereby impacting the production of cortical PNs dedicated to the upper layers[60]. This impact the balance between excitation/inhibition of PN and cINs. Consequently, defects in CCP1 function contributes to imbalances in cortical neuronal composition, a pathological mechanism that may underlie some neurodevelopmental disorders such as autism[60].

Loss-of-function (LOF) variants of CCP1 have been identified in human patients with different severities of neurodevelopmental phenotypes (Figure 16) [101]. Among these, p.Q856* is a homozygous nonsense mutation found in a 16-months-old female presenting a profound motor delay (abnormal eye movements, loss of head control), cognitive delay (no speech), hypotonia, tetraparesis, muscle loss, respiratory insufficiency and axonal motor neuropathy. The brain MRI shows a massive cerebellar atrophy and a dysplastic corpus callosum. Denervation and marked neurogenic reorganization are observed by electromyography. In this mutation, the expression of functional CCP1 is absent. This led to an excess in polyglutamylated tubulin, generated by the continuous activity of polyglutamylases, that appeared to accumulate in a diagnostic skeletal muscle biopsy specimen obtained from one of the patients. Consistent with this idea, CCP1 LOF has been associated with infantile-onset neurodegeneration[101].

1.4. ORGANOIDS

Different models are currently used to study brain development and cIN migration. To begin with, mouse fetal brain tissue has provided fundamental insights but as discussed in section 1.1.4, species-specific differences in progenitor populations, cIN proportions, and developmental timing limit the direct translation of findings to human biology. Two-dimensional iPSC-derived cultures offer a human genetic background but fail to recapitulate the three-dimensional architecture and regional organization of the developing brain[102]. 3D-cerebral organoids have therefore emerged as a compelling alternative[103]. Their high cellular diversity and three-dimensional spatial architecture recapitulate physiological processes more faithfully than two-dimensional culture [102], and cortical neurons derived from organoids display greater transcriptomic maturation compared to those from monolayer systems [104,105]. Furthermore, cortical organoids allow direct study of human biology and recapitulate human developmental features absent in rodent models, such as outer radial glial cells [106,107]. Also, they allow the use of patient-specific cell lines allows disease associated mutations to be studied in a human genetic background [108]. To correct or induce mutation of interest, isogenic controls can be used, and any observed differences can be attributed specifically to the mutation of interest rather than cell lines specific genetic variability. Nevertheless, organoids have limitations as they lack vascularization and immune system interactions, and do not fully recapitulate all cell types present in the developing brain[109].

3D organoids can be generated from ESC or iPCSs. iPSCs are adult somatic cells, such as fibroblast, that are genetically reprogrammed to revert to a pluripotent state similar to that of embryonic stem cells[110]. In this state, they can differentiate into virtually any cell type from the three germ layers through the action of specific transcription factors that maintain pluripotency and prevent differentiation. In 2006, Yamanaka *et al.* identified four essential factors required to reprogram differentiated somatic cells into pluripotent cells: OCT4, KLF4, SOX2, and C-MYC, collectively referred to as the Yamanaka or OKSM factors[110,111]. Additional factors such as Lin28, Nanog, and Oct3 are frequently included to enhance reprogramming efficiency[112]. These transcription factors reactivate the gene regulatory networks (e.g. promotion of *CHD1* expression, repression of *p53*) associated with pluripotency while progressively erasing the cells' original somatic identity [111,113]. During this process, cells exhibit decreased expression of somatic genes, metabolic reprogramming, increased proliferation, and inhibition of apoptosis and

senescence, resulting in an unlimited self-renewal capacity in culture. Pluripotency becomes stabilized once the expression of Sox2, Oct4, and Nanog is maintained independently of exogenous OKSM expression. iPSCs can then be differentiated into various cell types using cocktails of TFs aggregated to form 3D-organoids.

To generate brain organoids, numerous methods exist using guided or unguided patterning [108,114,115]. Unguided protocols are based on the tendency of embryoid bodies to spontaneously adopt a neuroectodermal fate through intrinsic factors, in the absence of exogenous growth factors (GFs). In this case, organoids can contain a mix of different brain region identities such as forebrain, midbrain, hippocampus, and retina[116]. Notably, in the absence of further pattering cues, neuroectodermal cells still tend to acquire a dorsal forebrain identity, generating cortical neurons that self-organize into rosettes[117,118]. Guided protocols rely on the addition of morphogens at specific time points, recapitulating the signaling pathways active during physiological development[114]. This approach enable the generation of organoids with a defined regional identity such as ventral telencephalon[107,119].

In guided protocols, the Dual SMAD inhibition protocol was a major advancement in the generation of cerebral organoids. It simultaneously inhibits the BMP and the TGF-β pathway[114,120] promoting neuroectodermal differentiation while suppressing mesodermal and endodermal cell fates. This protocol relies on two inhibitors (SB and DM) that efficiently drive the differentiation of iPSCs into a large population of neural progenitor cells[119]. The neuroectodermal identity can be further differentiated into specifically the forebrain. During this process, SHH is crucial for the ventral forebrain patterning while BMP and WNT that are important for dorsal forebrain identity [114]. Therefore, to produce organoids with a more ventral identity, thereby producing INs, additional morphogens (IWP2 and SAG) are introduced to increase activity in the SHH signaling pathway while reducing WNT pathway activity[121]. As a result, iPSCs can be directed toward a neuroectodermal fate with high efficiency[115].

Furthermore, organoids with different regional identity can be fused to investigate their interaction[114]. It has been shown that human ventral forebrain organoids recapitulate the MGE and human cortical organoids recapitulate the cerebral cortex[122]. Therefore, they can be fused to generate a model that mimic the tangential migration of interneurons toward the cortex, which is a key developmental process in the human brain[123,124]. Indeed, Bagley et al. showed that cerebral

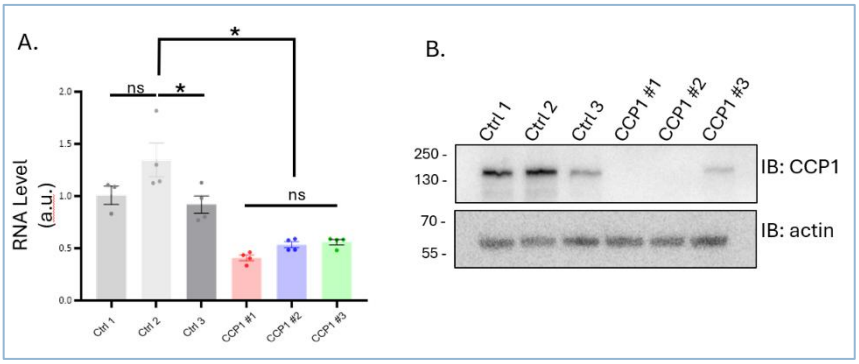

Figure 17 : Investigation of CCP1 mutation in human ventralized organoids (hvCO) model. (A) CCP1 RNA level in 1-month old hvCOs. Statistical comparison performed by ANOVA. ns = non significant. * = p<0.05. (B) Western blot of CCP1 and actin protein levels in 1-month ventral hvCOs. n=8-12 hvCOs per condition.

organoid fusion cultures can model complex interactions between different brain regions by imitating the dorso-ventral axe of the embryonic developing brain [125]. Altogether, ventral forebrain cerebral organoids constitute a highly relevant model for studying human brain development, particularly the generation and migration of interneurons[108,126].

1.5. PRELIMINARY DATA

iPSC coming from three patients carrying loss of function mutation on CCP1 gene (Family A, B and D [101]) alongside with 3 control cell lines being used in the host laboratory. Patient coming from family A, renamed CCP1 #1; harbors compound heterozygous mutations: a nonsense mutation (p.Y912*) introducing a premature stop codon and a splice site variant (c.2336-1G>T) affecting a canonical splice site and leading to the use of an alternative cryptic splice site, thereby altering the mRNA sequence and disrupting the open reading frame. Both mutations result in CCP1 LOF. Cell line CCP1 #2 (Family B), corresponding to the patient cell line described in section 1.3, carries a homozygous nonsense mutation (p.Q856*) resulting in CCP1 LOF. Finally, CCP1 #3 (Family D) carries two missense mutations (p.T851M and p.H990L) predicted to have a functional impact[101] (mutation positions are shown in Figure 16 in section 1.3). The control cell lines include H9 (WiCell, WAO9), an embryonic stem cell (ESC) line, and GM38 (Coriell, GM23394) and GM40 (Coriell, GM23346), which are iPSC lines. They are respectively called control #1, control #2 and control #3. Human dorsal cerebral organoids (hdCO) and human ventral cerebral organoids (hvCOs) generated from these cell lines were first characterized to validate their regional identity (not shown) and CCP1 expression. They were subsequently fused to generate assembloids, enabling the study of cIN migratory behavior and its impact on the progenitor populations of the dorsal compartment.

The qRT-PCR analysis revealed that the CCP1-mutated hvCOs exhibited lower CCP1 mRNA expression levels compared to the control hvCO (Figure 17A). Consistently, WB analysis showed that CCP1 protein was detected in all three controls, whereas no CCP1 expression was observed in hvCO CCP1 #1 and #2. A reduced but detectable level of CCP1 protein was observed in hvCOs from CCP1 #3 consistent with the missense nature of the mutations which are predicted to destabilize the protein structure, rendering it susceptible to proteasomal degradation (Figure 17B). Despite its partial detection, this residual protein has been shown to be catalytically inactive[101]. Together, these results confirm the loss of CCP1 expression both at the mRNA and protein levels in the mutant hvCOs, validating the model to study CCP1 LOF in a human context.

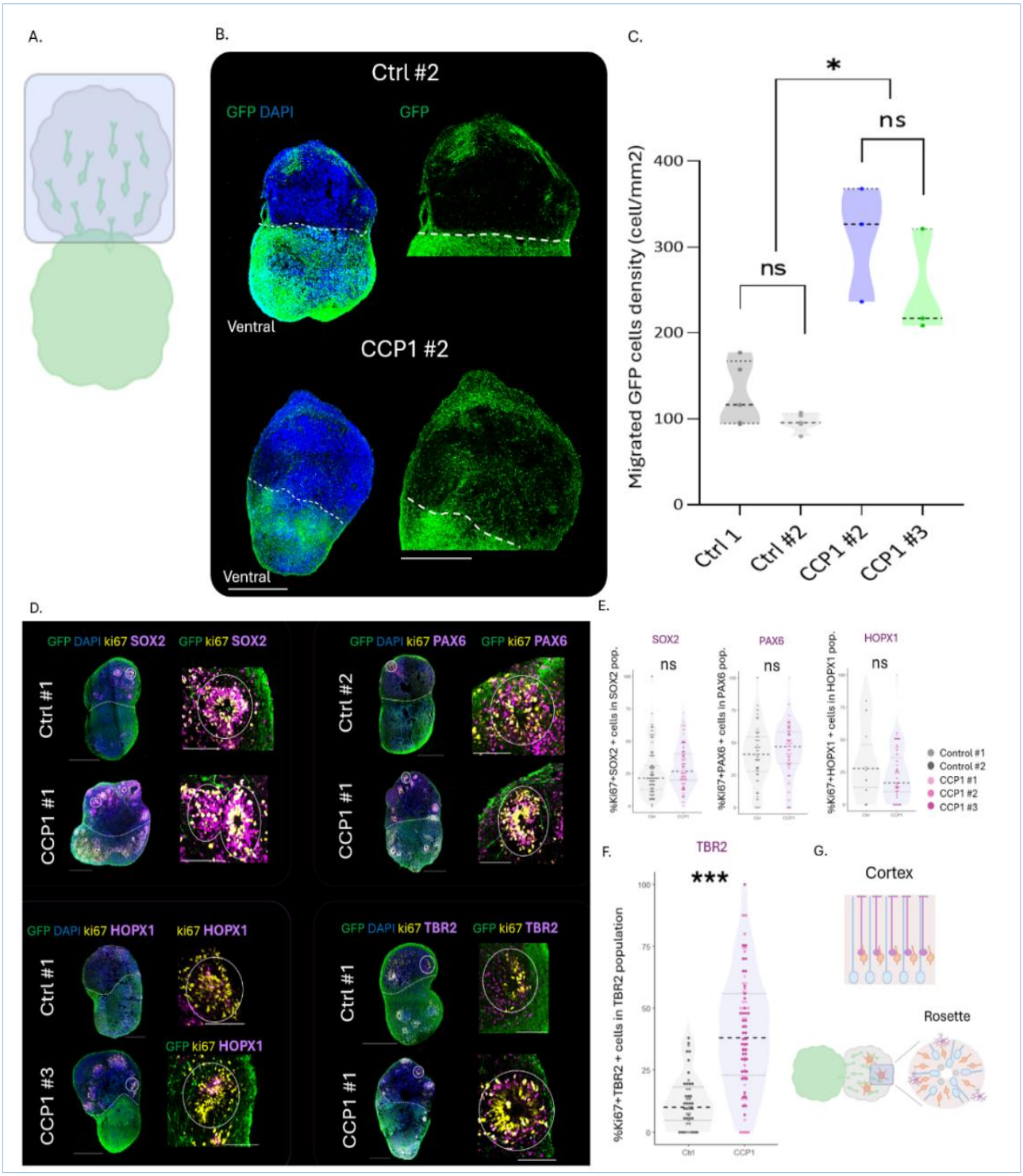

Figure 18 : Advancement of cIN migration front and increased intermediate progenitor proliferation in assembloids. (A) Schematic representation of an assembloid displaying cIN migration from human ventralized cortical organoid (hvCO) toward human dorsalized organoids (hdCO). (B) Representative confocal images showing GFP+ cIN invasion into the dorsal part of 60 days old assembloid in control #2 and CCP1 #2 conditions. (C) Violin plot of the dorsal invasion by quantification of migrated GFP+ cells in the dorsal part of the assembloid. Statistical comparison by ANOVA. ns = non significant. * = p<0.05. (D) Representative confocal images of progenitor population proliferation in 60 days old control and CCP1 mutant assembloids stained for Ki67 (yellow), DAPI (blue), SOX2, PAX6, HOPX1 and TBR2 (purple). Scale bar for the assembloids 500 µm, scale bar for the rosettes 20 µm. (E-F) Violin plots showing the percentage of Ki67 positive cells in the corresponding progenitor population within rosettes. Statistical comparison by t-test. ns: non-significant; *** p<0.001. (G) Schematic representation of the cortex and rosette organization. Grey = general neural progenitor population; blue, apical progenitors; purple, outer radial glia; orange, intermediate progenitors; green, cortical interneurons. Details on the number of differentiations, organoids, and rosettes analyzed are provided in Annex 1.

These cell lines were subsequently used to generate assembloids through the fusion of 1-month-old hvCOs and 1-month-old hdCOs (Figure 18A). A significant increase in the density green fluorescent protein (GFP)+ cINs within the dorsal region was observed in 2-month-old CCP1-mutated assembloids compared to control assembloids, indicating enhanced invasion from the ventral to the dorsal regions (Figure 18B–C). This result recapitulates the temporal advancement of cIN cortical invasion previously described in CCP1 cKO mouse models[101], where a larger cohort of cINs reaches the cortex at a given developmental stage, increasing their contact with dorsal progenitor populations and influencing specifically IP proliferation.

To assess progenitor proliferation within the human assembloids, analyses were focused on rosettes present within hdCOs. Rosettes are self-organized structures composed of neural progenitor cells radially arranged around a central apical lumen, sharing structural and cellular features with the ventricular zone of the developing cortex[116] (Figure 18G). Proliferation within each progenitor population was quantified as the proportion of Ki67+ cells relative to the total marker+ population. Progenitor populations were identified using the following markers: SOX2 for the general neural progenitor population, PAX6 for RGCs, HOPX1 for oRGs, and TBR2 for IPs (Figure 18D). No significant differences in proliferation were observed between CCP1 mutated and control assembloids, except for IPs, which showed a significant increase in Ki67-positive cells in the mutant condition (Figure 18E–F). This selective effect on IPs is consistent with findings previously described in CCP1 cKO mouse model[60]. As shown, in mice, this suggests a preferential communication between from the migrating cINs and IPs.

In mice, migrating cINs are known to communicate with IPs during migration through unknown diffusible cues[60]. The selective increase in IP proliferation observed in our human model suggests a similar mode of crosstalk in human, though this remains to be experimentally confirmed. These findings prompted us to investigate of the secretome of migrating cINs as a mean to identify the molecular nature of these signals. To ensure that any differences observed between conditions could be specifically attributed to CCP1 LOF rather than inter-individual genetic variability, isogenic control lines derived from the mutated cell line were generated and were characterized and used during this master thesis.

2. HYPOTHESES, OBJECTIVES AND STRATEGY

Migrating cINs are known to secrete diffusible signals capable of influencing surrounding cortical progenitor populations in mouse and human, however the identity of these factors and their potential role in regulating IP proliferation during human cortical development remain unknown. CCP1, a deglutamylase enriched in cINs, has been shown to regulate cIN migration dynamics and cortical invasion, with its loss leading to premature accumulation of cINs and altered IP proliferation due to these unknown diffusible cues. The key question is therefore: which proteins are secreted by migrating human INs derived from hvCOs, could these act as paracrine signals influencing surrounding cortical progenitors, and could a CCP1 loss of function also be reflected in the secretome?

This work had two major objectives. The **first objective** was the generation and characterization of hvCOs from CCP1 patient variant and isogenic control cell lines, serving to validate CCP1 loss of function and confirm the ventral identity of the organoids. The **second objective** was to develop a working protocol for the collection of the interneuron secretome, as a foundation for future proteomic analysis.

Table 2 : Summary of cell lines.

	CCP1 #2	Isogenic control
Age	5 MO	5 MO
Lineage	hIPS	hIPS
Sex	female	female

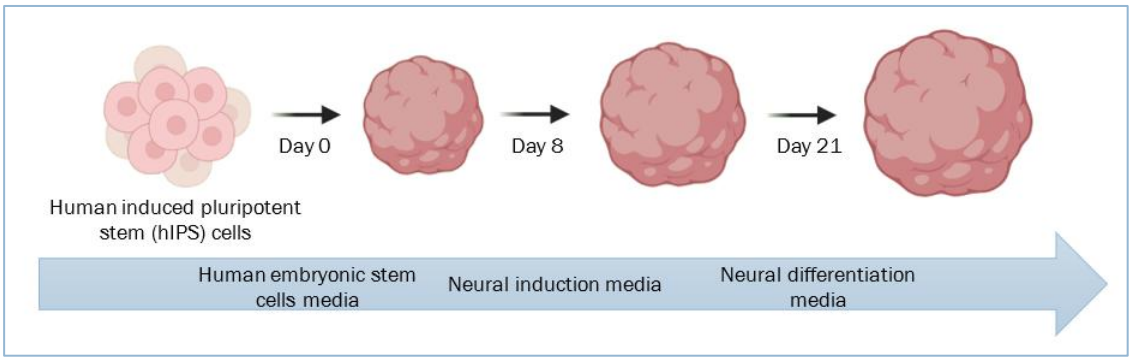

Figure 19 : Differentiation protocol. Schematic representation of the ventral forebrain organoid differentiation protocol, illustrating the sequential stages of organoid generation, including neural induction, ventral patterning, and maturation over time. Human induced pluripotent stem cells, hIPS.

3. MATERIEL AND METHODS

3.1. ORGANOIDS CONCEPTION

3.1.1. CELL LINES

Two cell lines were used during this master thesis (Table 2). CCP1 #2 is a patient-derived iPSC line carrying a homozygous nonsense mutation in CCP1 (p.Q856*). This mutation results in a premature stop codon, leading to a truncation of the CCP1 protein within the peptidase domain and a LOF [101]. The isogenic control CCP1 #2 was obtained by correction of the mutation of CCP1 #2 on both alleles by CRISPR-Cas9 (Clustered Regularly Interspaced Short Palindromic Repeats and CRISPR-associated protein 9) gene editing by Synthego. CCP1 #2 and the isogenic control cell lines were made pluripotent by Bernard Coumans, technologist of the laboratory. Cells were cultured on GelTrex (gibco, A40000468) coated 6 wells cell (Greiner, 657160) culture dish with modified Tenneille's Serum Replacement (mTeSR, maintenance medium for human PSCs containing bFGF and TGFβ) medium (StemCell, 100-287). Dishes were coated by adding 1 ml per well of resuspended GelTrex into DMEM/F12 medium (Thermo, 12053569).

3.1.2. GENERATION

hVCO were generated using a protocol adapted from the Dual SMAD Inhibition Protocol (Figure 19). Day 0 corresponds to the generation of embryoid bodies. Upon reaching 70 to 80% confluence, cells were washed twice with dulbecco's phosphate buffered saline (dPBS) (gibcco,14040133) before incubating in 600 µL of accutase (Merck-Sigma, SCR005) supplemented with 20 µM (1:1000) of Rock Inhibitor (RI) (BioConnect, S1049) per well for 3 min (minutes) at 37°C. Cells were then mechanically detached by repeated pipetting with a P1000 pipette for no longer than 1 minute (min). Human embryonic stem cell (hESC) medium (Table 3) was then added, and cell detachment was further completed using a 5 mL serological pipette. The suspension was transferred into a 15 mL tube and further homogenized by pipetting approximately 20 times. At this stage, cell concentration is determined using the Invitrogen™ Countess™ 3 Automated Cell Counter (10µl of cell suspension diluted 1:2 in dPBS into a Countess slide).

Table 3 : Composition of the different media.

Product	Reference	hESC	NIM	NDM-A Young	NDM-A Old
DMEM/F-12, GlutaMAX™ supplement	Gibco™ 31331028	80%	97%	48%	48%
KnockOut™ Serum Replacement	Gibco™ 10828028	20%	/	/	/
Neurobasal™ Medium	ThermoFisher 21103049	/	/	48%	48%
GlutaMAX™ Supplement	ThermoFisher 35050-038	1%	1%	0.5%	0.5%
MEM Non-Essential Amino Acids Solution	Gibco™ 11140035	1%	1%	1%	1%
Penicillin-Streptomycin	Gibco™ 15140122	1%	1%	1%	1%
Beta mercapto ethanol	Sigma-Aldrich M7154	1mM	/	0,5mM	/
Heparin	Sigma-Aldrich H3149	/	1%	/	/
N2	ThermoFisher 17502048	/	/	0.5%	0.5%
B27 -VitA	ThermoFisher 12587010	/	/	1%	1%
Insulin	Sigma-Aldrich I9278	/	/	2,5 µg/ml	/

Subsequently, the suspension was centrifuged for 4 min at 300 g at room temperature (RT) and the cells were resuspended in hESC medium supplemented with 4 ng/ml of basic fibroblast growth factor (bFGF) (ThermoFischer, 100-18B) and 20 µM of RI. The cell concentration was adjusted to reach a total of 9,000 cells per 150 µl. The suspension was then transferred into a U-bottom ultra-low-attachment 96-well plate (174925, ThermoScientific). Finally, the plate was centrifuged for 2 min at 200 g and RT ensuring the seeding of the cells before being placed in an incubator at 37°C with 5% CO_2.

On day 1, cell aggregation at the bottom of each well was observed. The medium was then replaced with hESC medium with the same concentration of RI and bFGF but supplemented with 100 nM LDN193189 (Milteny Biotech, 130-103-925), 5 µM XAV939 (StemCell, 72-672) and 10µM SB431542 (Sigma-Aldrich, S4317) to induce a neuroectodermal identity. As only 50 µL of the 150 µL total well volume was replaced, LDN193189, XAV939, and SB431542 were prepared at three times the target concentration in the fresh medium, ensuring the correct final concentration.

On day 3 and day 6, the medium was replaced with hESC medium supplemented with LDN193189, XAV939, and SB431542 at their target concentrations. From day 6 onwards, bFGF was omitted, and the RI concentration was reduced to half its initial value. On day 8, the medium was changed to neural induction media (NIM, table 3) supplemented with 100 nM SAG (Sigma-Aldrich, SML314) and 2.5 µM IWP2 (Sigma-Aldrich, 10536) to promote forebrain patterning. A volume of 120 µL of the previous medium was removed and 150 µL of NIM was added. Until day 22, wells were refreshed 3 times per week by replacing 50 µL of medium.

On day 22, the NIM was replaced by neural differentiation media young (NDM-Ay, table 3), which was further changed three times per week until reaching 30 days old. After 30 days of culture, organoids were transferred into P60 dishes (Corning, 430196) containing 5 mL of NDM-A old (NDM-Ao, table 3) medium and maintained on a shaker at 75 rpm to ensure adequate oxygenation. A maximum of 24 organoids were pooled per dish to prevent fusion. Twice a week, 1 mL of medium was removed and replaced with 1.5 mL of fresh medium.

3.1.3. ORGANOID PERIMETER AND AREA QUANTIFICATION

Organoid growth was quantified by measuring organoid area using the software Fiji Is Just Image J (FIJI) (ImageJ distribution, version 1.8.0_322). The spatial scale was defined with a known distance of 1000 µm corresponding to 557 pixels.

The polygon selection tool was used to manually trace the contour of each organoid. Normality was assessed on growth curves using the Shapiro–Wilk test. Normally distributed data were

analyzed using t-test followed by multiple comparisons testing (comparison of each column mean with every other column mean). Analyzes were monitored and computed using GraphPad Prism (version 8.0.2.263).

3.2. CARACTERISATION OF mRNA

3.2.1. mRNA EXTRACTION

The Zymmo quick RNA miniprep (Zymo Research, R1054) was used to extract the messenger ribonucleic acid (mRNA) of 4 to 12 organoids per trials. Briefly, organoids were mechanically dissociated in 600 µL of lysis buffer at room temperature (RT) until a homogenous, water like consistency was achieved. If the lysate was too viscous, additional lysis buffer (50 µL increments) was added until the desired consistency was reached. The lysate was then transferred to a Spin-Away Filter in a collection tube and centrifuged at 12,000 g for 30 seconds (sec) to remove most genomic DNA. The flow-through was homogenized with an equal volume of absolute ethanol and transferred to a Zymo-Spin IIICG column in a collection tube, followed by centrifugation at 12,000 g for 30 sec. This step is repeated until the entire mix has been filtered. The flow-through was discarded, and the column underwent in-column DNase I treatment. Columns were washed with 400 µL RNA Wash Buffer and centrifuged at 12,000 g for 30 sec, discarding the flow-through. Each sample was then incubated at RT for 15 min with 80 µL of DNase I Reaction Mix (5 µL DNase I, 1 U/µL, and 75 µL DNA Digestion Buffer). Following DNase treatment, 400 µL RNA Prep Buffer was applied to the column and centrifuged at 12,000 g for 30 sec. Columns were subsequently washed twice with 700 µL and 400 µL of RNA Wash Buffer, each followed by centrifugation at 12,000 g for 30 sec. Columns were then transferred to RNase-free tubes, and RNA was eluted with 35 µL of DNase/RNase-free water directly onto the column matrix, followed by centrifugation at 12,000 g for 1 min. RNA concentration and purity were assessed using a NanoDrop spectrophotometer. Purified RNA samples were stored at –80°C until further use.

3.2.2. RETROTRANSCRIPTION

Complementary deoxy-nucleic acid (cDNA) synthesis was performed using the RevertAid H Minus First Strand cDNA Synthesis Kit (Thermo Scientific - K1632). Preparation steps were performed on ice to preserve RNA integrity. For each reaction, 500 ng of total RNA were diluted in nuclease-free water to a final volume of 16 µL. Subsequently, 2 µL of random primers were added, and samples were incubated for 5 min. A reaction mix was then prepared containing RevertAid

H Minus reverse transcriptase (100 U/µl), 5x reaction buffer, deoxyribonucleotide triphosphate (dNTP – 10mM) mix, and RiboLock RNase inhibitor (20 U/µl), according to the manufacturer's instructions. The reaction mix was then added to each sample. Reverse transcription was carried out using a Biometra T3000 Thermocycler. The thermal program consisted of an initial incubation at 25°C for 5 min, followed by 45°C for 60 min to allow cDNA synthesis, and a final inactivation step at 70°C for 5 min. Synthesized cDNA was stored at −20°C until use.

3.2.3. qPCR

qPCR was performed using the GoTaq qPCR kit (Promega - A6102). The cDNA was diluted in sterile DNA/RNAse free water to a final concentration of 3.125 ng/µL. For each reaction, 5 µl of 2x qPCR Master Mix, 0.25 µL of forward primer (250 nM), 0.25 µL of reverse primer (250 nM), 0.5 µL of nuclease-free water and 4 µl of diluted cDNA (12.5ng) were combined. Primers were used at a stock concentration of 10 µM. Two housekeeping genes (*YWHAZ* and *HPRT*) and four target genes of ventral forebrain identity (*DCX*, *DLX5*, *NKX2.1*, and *GAD67*) plus *CCP1* were analyzed (Sequences in the annex 2).

Reactions were loaded in a 384-wells plate (Bioke, 4ti-0380 plus 4ti-0560, Combi pack), and centrifuged (1 min at 1,000 g) ensuring that the mix and samples were collected at the bottom of each well. Amplification was performed using the LightCycler 480 Real-Time PCR System (Roche). The thermal cycling protocol consisted of 45 amplification cycles, including a denaturation step at 95°C and an annealing/extension step at 60°C for 30 seconds.

To perform the statistical analyses, Absolute Quantification/Fit were retrieved. Relative gene expression was computed using the comparative Ct (ΔΔCt) method. ΔCt values were calculated as follows: $\Delta Ct = Ct_{\text{target gene}} - Ct_{\text{YWHAZ}}$. ΔΔCt were then calculated $\Delta\Delta Ct = \Delta Ct - \Delta\bar{C}t$; followed by the Fold change $= 2^{-\Delta\Delta Ct}$. Statistical analyses were performed using GraphPad Prism (version 8.0.2.263). Outliers were identified with the ROUT method (Q=1%) and excluded from subsequent analyses. Normality was assessed using the Shapiro–Wilk test. Normally distributed data were analyzed using one-way ANOVA followed by multiple comparisons testing (comparison of each column mean with every other column mean). Non-normally distributed data were analyzed by Kruskal–Wallis test with multiple comparisons.

3.3. CARACTERISATION OF PROTEINS

3.3.1. WESTERN BLOT

hvCOs were lysed in RIPA buffer supplemented with protease (Sigma, P8340) and phosphatase inhibitors (Sigma, 4906845001). Cells were lysed mechanically with a tissue grinder and proteins were allowed to solubilize on ice for 30 min and centrifuged for 10 min at 10,000 rotations per min. Total protein concentration of the supernatant was determined using a bicinchoninic acid (BCA) assay (ThermoFischer, 23223).

20 µg of protein samples were denatured by heating 5 min at 95°C, before loading them to 10% SDS-PAGE gel. A molecular marker (#26619, ThermoFisher) was used in order to follow the migration of the proteins of interest. The gel electrophoresis was performed at 120 mV for approximately 1h30 in Running Buffer. Proteins were subsequently transferred onto a polyvinylidene fluoride (PVDF) membrane (EmershamTM HybondTM P 0.45 PVDF #10600023, Cytiva) previously activated with methanol at 300mA for 2 h in Transfer buffer.

Membranes were blocked in 5% milk bovin serum albumin (BDA) diluted in blocking solution (TBS-T) for 1 h at 4°C to prevent non-specific binding. Membranes were then incubated overnight at 4°C with primary antibodies targeting CCP1 (CCP1 rabbit # 14067-1-AP, Proteintech). After 3 times washing with TBS-T 10 min at RT, membranes were incubated with the secondary antibodies (1:5000 in blocking solution) for 45 min at RT. Then, membranes were incubated for 2 hours (h) at RT with a-tubulin-HRP antibody (#9099, Cell Signaling) at a 1:5,000 dilution in blocking solution.

Protein bands were revealed using an enhanced chemiluminescence (ECL) substrate (PierceTM ECL Western Blotting Substrate #32106, Thermoscientific) and detected with Amersham ImageQuantTM 800 western blot imaging system (Cytiva).

3.3.2. COLLECTION AND CRYOSECTION

Organoids were fixed in 4% paraformaldehyde (PFA) (15710 – Electro Microscopy Sciences) for 45 min at RT. Following fixation, organoids were incubated in a 30% sucrose (27478.365, VWR Chemicals) solution in PBS at 4°C for a minimum of 3 days.

Samples were then transferred into Neg-50 Optimal Cutting Temperature compound (OCT) (NT-50, 6506, Epredia) to remove residual sucrose. Organoids were positioned at the bottom of

Table 4 : references, dilution and species of antibodies used for IF.

Name	Reference	Dilution	Specie
Anti GAD67	Merck – MAB5406	1:500	Rabbit
Anti SOX2	BD Pharmigen - 561469	1:500 for slides 1:300 for dishes	Mouse
Anto SOX10	R&D System – AF2864	1:500	Goat
Anti NKX2.1	Abcam – Ab76013	1:500	Rabbit
Anti CCP1	Abcam – Ab244512	1:500	Rabbit
Anti SST28	Synaptic Systems – 366 006	1:500 for slide 1:300 for dishes	Chicken
Anti PDGFRa	R&D Systems – AF1062	1:300	Goat
Anti PAX6	Merck Millipore – AB2237	1:500	Rabbit
Anti caspase 3	Cell signaling - 9661	1:500	Rabbit
Anti TUJ1 (=beta III tubulin)	BioTechne – MAB1195	1:500	Mouse
Anti LHX6	Santa Cruze – sc-271433	1:500	Mouse
Anti MAP2	Abcam – Ab5392	1:500	Chicken
Secondary antibodies	Invitrogen – Alexa-Fluor	1:1000	Donkey

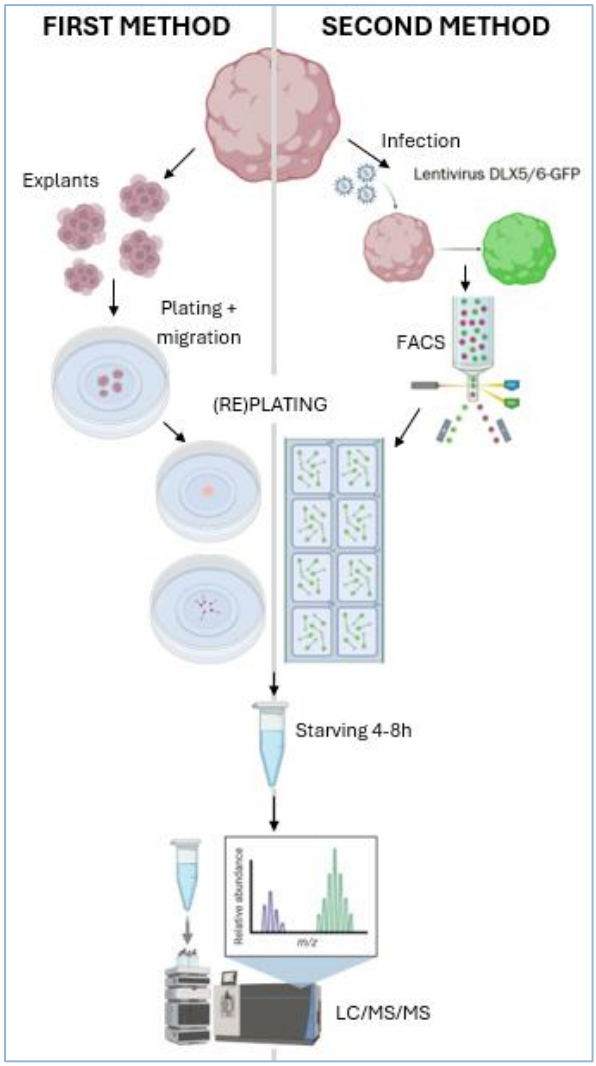

Figure 20 : comparison of first and second method used of the secretome analyses. On the left, first method-specific features are represented. On the right second methods-specific features are represented. On the middle, shared features.

plastic embedding molds filled with OCT compound, rapidly frozen in cold isopentane on dry ice, and stored at −80°C until cryosectioning.

Cryosections were prepared using an Epredia Cryostar NX70 cryostat. Sections of 14 µm thickness were cut at −19°C (chamber and blade temperature) and mounted onto SuperFrost Plus adhesive slides (J1800AMNZ, Epredia). Slides were dried overnight at RT and stored at −20°C until further use.

3.3.3. IMMUNOFLUORESCENCE

Slides were washed twice for 5 min in PBS, followed by antigen retrieval using Dako target retrieval solution (Agilent - S2367)1x solution (10x stock diluted in Milli-Q water) for 15 min at 90 °C. Slides were then washed 3 times for 5 min in PBS and permeabilized for 1 h at RT in a humidified light protected chamber using a buffer containing 1% Bovin Serum Albumin (BSA) (8076.3, Roth), 5% donkey serum (017-000-121, Jackson ImmunoResearch), and 0.5% Triton X-100 (T8787, SIGMA) in PBS. Primary antibodies were applied overnight at 4 °C in a humidified chamber in a buffer composed of 3% BSA, 5% donkey serum, and 0.3% Triton X-100 in PBS. Antibody used were SOX2, SOX10, NKX2.1, SST28, GAD67, PAX6, CCP1, and PDGFRα (table 4). Slides were washed 4 times for 15 min with PBS-T (Tween 0,1% - P9416, SIGMA) and incubated with secondary antibodies for 2 h at RT at a dilution of 1:1000. Nuclear staining was performed with 4’,6-diamidino-2-phenylindole (DAPI) (1:2000 – D9542, SIGMA) for 15 min at RT, followed by 2 washes of 5 min in PBS. Slides were mounted using DAKO fluorescent mounting medium (Agilent Dako, S3023, Agilent) and left to dry overnight at RT. IF images have been captured using the NIKON confocal microscope using the 20X dry objective.

3.5. SECRETOME ANALYSIS

The objective of this section was the collection the secretome of migrating cINS from hvCOs, the proteins secreted by human interneurons during their migration. To this end, the secretome was to be collected following 6 and 10 h of starvation from two conditions: one enriched in migrating cINs and one enriched in neuronal progenitors. The collected medium would then be sent to the GIGA mass spectrometry platform for processing by Christopher Kune and Gabriel Mazzuchelli using liquid chromatography coupled to tandem mass spectrometry (LC-MS/MS).

During this master thesis, the sample collection protocol was developed; however, secretome collection and mass spectrometry analysis were not reached. Two different protocols were tested, as illustrated in Figure 20.

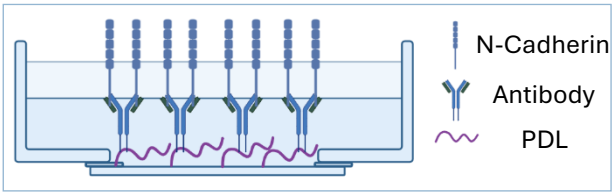

Figure 21 : Scheme of the coating. In a glass bottom dish, subsequent layers of PDL, antibody anti constant fraction and Ncadh. PDL = poly-d-lysin.

Table 5 : respective volumes of solution for each type of dish.

	1 COMPARTMENT	4 COMPARTMENTS	8 COMPARTMENTS
Poly-D-lysin	600 µl	150 µl	300 µl
Anti-Fc	500 µl	120 µl	300 µl
Ncadh + fibronectin	500 µl	120 µl	300 µl
Starving		200 µl	250 µl

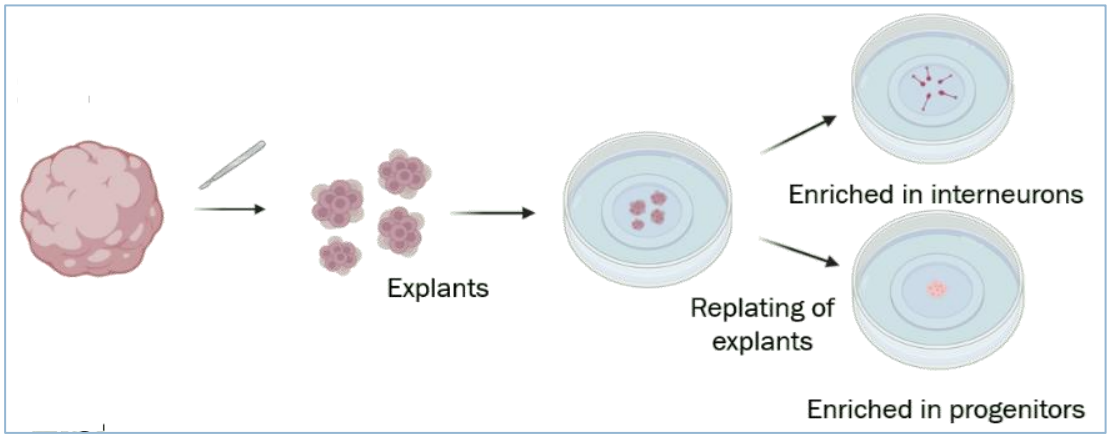

Figure 22 : Pipeline of the first method of the secretome analysis. Explants are made from organoids by scalpel dissection. They are then plated and replated after many days into a condition enriched in interneurons (top right) and a condition enriched in progenitors (bottom right).

3.5.1. DISH COATING

Different types of culture dishes were tested, including single-compartment (Greiner Bio-One, 627870), four-compartment (627870, Greiner) and eight-compartment formats (80826 - ibidi). Volumes of coating solutions were adjusted accordingly for each type of dish (see Table 5).

Dishes were first incubated with poly-D-lysine (PDL) at 37°C for 2.5 h followed by 3 PBS washes. PDL working solution (1x) was prepared from a 10x stock solution (SigmaAldrich, P7786) diluted in PBS. The anti-mouse Fc antibody solution was then added, and dishes were incubated overnight at 4°C. Mouse anti-Fc antibody solution was prepared by performing a 1:200 dilution (4 µg/100 µL, Sigma-Aldrich, M4280) in borate buffer. Dishes were then incubated for 3 h at 37°C and washed 3 times with borate buffer. The borate buffer was prepared using 3,09g of boric acid (BP161-1 - Fisher) and 0,5g of NaOH (Roth, 9356.1) in 500ml of miliQ water and the solution was sterilized by autoclave. The N-Cadherin (Ncadh) solution was then added, and dishes were incubated at 37°C for 3 h (Figure 21). Ncadh (Biotechne, 6626NC050) was reconstituted in PBS to obtain a 10x stock solution. The working solution (1x) was prepared by diluting the stock solution in borate buffer. Fibronectin (Sigma-Aldrich, F4759) was then added from a 100x stock solution and diluted to its final working concentration (1x) in the same borate buffer containing Ncadh. Finally, dishes were rinsed twice with PBS and stored at 4°C, sealed with parafilm until further use (Figure 21).

3.5.2. FIRST METHOD – PLATING, MIGRATION AND REPLATING

One month and half hvCOs were cut in half to remove the necrotic regions and dead cells. The remaining tissue was further dissected into explants using either forceps and a scalpel or a tissue punch (Figure 22).

For plating, PBS was completely removed from the 4 compartments coated dish and 70 µl of pre-warmed NDM-Ao medium was added. Approximately 30 explants were collected in a total volume of 60 µl and distributed across the dish and supplemented with an additional 60 µL of medium added very slowly. Floating explants were carefully pressed to the bottom of the dish using forceps. Another 60 µl of medium was then added very slowly. The dish was incubated for 30 min at 37°C and 5% CO2 and the medium was adjusted to reach a final volume of 500 µl by compartment. When performed on one compartment dishes, all volumes and number of explants were quadrupled.

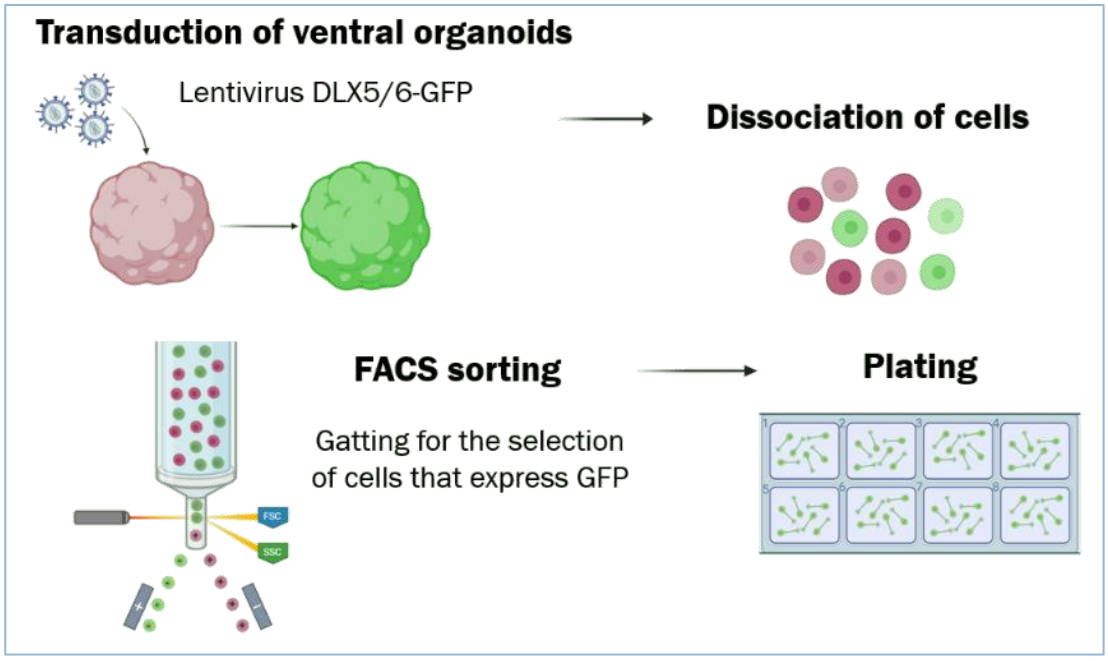

Figure 23 : Pipeline of the second method of the secretome analysis. Organoids are infected prior dissociation and FACS sorting. GFP + and – neg cells are plated in a 8 compartments dish.

Explants were incubated for 8 to 10 days, with NDM-Ao medium change twice a week, allowing cINs to migrate out of explants. Explants were then carefully removed from the dishes and replated into another to generate respectively an interneuron-enriched condition and a progenitor-enriched condition. In the interneuron-enriched condition, explants were carefully removed while minimizing disruption of the migrated interneurons, either by (1) applying small, sharp movements with forceps, (2) by dissecting around the explant with forceps, or (3) by using a tissue punch. For the progenitor-enriched explant condition, explants were plated following the protocol described before. In both conditions, each compartment contained 350 µL of NDM-Ao.

As starving is common to both methods, it is explained in 3.5.4.

3.5.3. SECOND METHOD

3.5.3.1. INFECTION

hvCOs were cut in half, and their necrotic centers and dead cells were removed 3 days prior to infection to label healthy cINs. Cut organoids were infected by a GW_1701 pLV mDLX CopGFP lentivirus (vector type rLV2) at a concentration of 6.87 x 10^7 TU/µL with a multiplicity of infection (MOI) of 15.

Each half-hvCOs was first transferred into a well of a 96-well plate into 100 µL of NDM-Ao. In the L2 laboratory, the viral solution was prepared in conditioned medium in which the organoids were previously maintained, according to the formula:

$$volume\ of\ virus = \frac{MOI \times \#\ of\ cells\ to\ infect\ (^{\#cells}/_{1/2org} \times \#1/2org)}{virus\ titration\ (\frac{TU}{\mu l})}.$$

Per half organoids, 50µL of virus solution was added. The organoids were incubated for 4 h at 37 °C, after which the medium containing the virus was removed and replaced with 150 µL of fresh NDM-Ao. Finally, media was replaced every two days for two weeks (Figure 23).

3.5.3.2. DISSOCIATION

Two weeks after infection, organoids were cut into four pieces and transferred into HBSS. The HBSS was then removed, and a solution containing 450 µL of papain (Cell System, LK003159) and 50 µL of DNase I (Cell System, LK003159) was added, followed by an incubation of 20 min at 37 °C and 5% CO2.

Subsequently, 500 µL of ovomucoid (Cell System, LK003159) was added to neutralize the papain. The solution was removed, 1 mL of HBSS was added, and mechanical dissociation was

performed through 25 up-and-down using a P1000. The suspension was passed through a 40 µm filter and left on ice for 5 min, allowing dead cells to aggregate, float and be easily removed. Samples were then centrifuged for 5 min at 4 °C at 300 g, the supernatant was removed and the cells were resuspended in 1000 µL of NDM-Ao.

3.5.3.3. FACS

Cell sorting was performed at the FACS (fluorescence activated cell sorting) platform of the GIGA Institute using the CytoFLEX SRT. Cells were sorted based on GFP fluorescence intensity into two distinct populations: GFP+ cells corresponding to interneurons and GFP- cells corresponding to progenitors. Sorted cells were collected into NDM-Ao medium for further analysis.

In this technique, cells were passed through a nozzle and hydrodynamically focused into a single-cell stream. Individual cells were traversed by a laser, and the emitted fluorescence signal was collected through an optical detection system and measured using photomultiplier tubes (PMTs). Based on GFP fluorescence intensity, cells were identified as GFP+ or GFP- and subsequently sorted into separate collection tubes. Cell sorting was achieved by applying an electrical charge to droplets containing individual cells, allowing their electrostatic deflection into the appropriate collection tube.

3.5.3.4. PLATING

Cells obtained from the FACS sorting were plated into 8 compartments dishes with an NCadh coating. Based on the total cell yield from FACS sorting, different cell densities were tested were tested (60,000, 30,000, 15,000, 7,500, 5,000 cells/compartment). NDM-Ao medium was added to each well to reach a final volume of 350 µL per compartment. Cells were then incubated at 37°C and 5% CO_2 overnight.

The remainder of the protocol is shared between the two methods.

3.5.4. STARVING

The medium was removed, then compartments were rinsed twice with Neurobasal-A medium minus phenol red (gibco - 12349015) to remove dead cells. 300 µl of Neurobasal-A medium minus phenol red was then added to each compartment (Table 3 - starving). Two starvation conditions of 6 and 10 h were initiated. At the end of these periods, the medium from each well was collected and stored at −20 °C.

3.5.5. FIXATION AND IMMUNOFLUORESCENCE

After the collection, dishes are fixed in PFA 4% for 15 min. After 2 rinses of PBS, dishes are conserved in PBS at 4°C. IF was performed in a light-protected box. Cells were incubated with 300 µl of permeabilization solution (5% donkey serum and 0.5% Triton X-100 in PBS solution) for 1 h at RT. Primary antibodies (cleaved Caspase-3, TUJ1, SST28, and LHX6 (table 4)) were then incubated overnight at 4 °C in a buffer containing 3% BSA, 5% donkey serum, and 0.1% Triton X-100 in PBS. Samples were then washed four times for 10 min with PBS, and incubated with secondary antibodies for 2 h at RT. Samples were subsequently washed four times for 15 min with PBS-T 0.1%, followed by nuclear staining with DAPI (1:1000) for 15 min at RT. Samples were rinsed in PBS and stored in PBS at 4 °C until imaging. Imaging of dishes was done using the NIKON confocal microscope, 20X dry objective. Fluorescence settings were adjusted in terms of laser power, gain, pinhole and scan speed to obtain qualitative pictures.

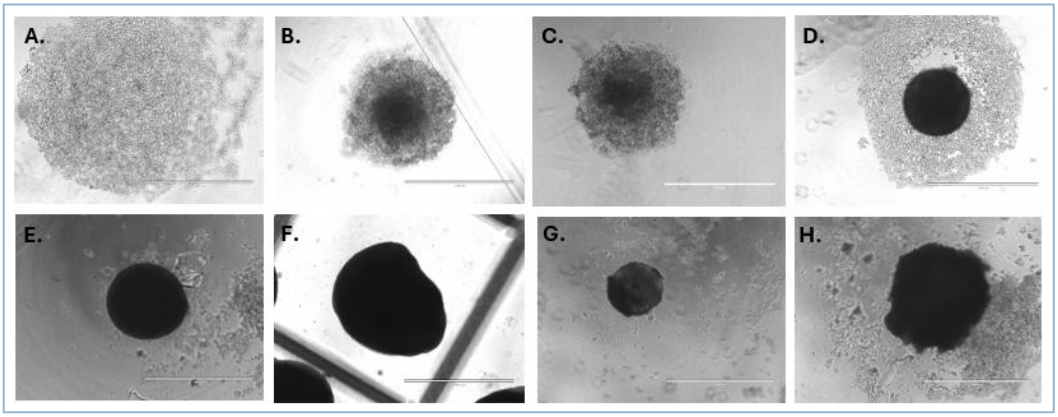

Figure 24: Representative brightfield images of organoid morphology and growth across development. (A–F) Organoids at days 0, 1, 2, 10, 15, and 30 respectively, illustrating the progressive compaction and growth of viable organoids over time. (G–H) Examples of non-viable organoids. (G) Organoid displaying an abnormally small size and transparent appearance. (H) Organoid showing extensive cell death and debris. Scale bar: 1000 µm.

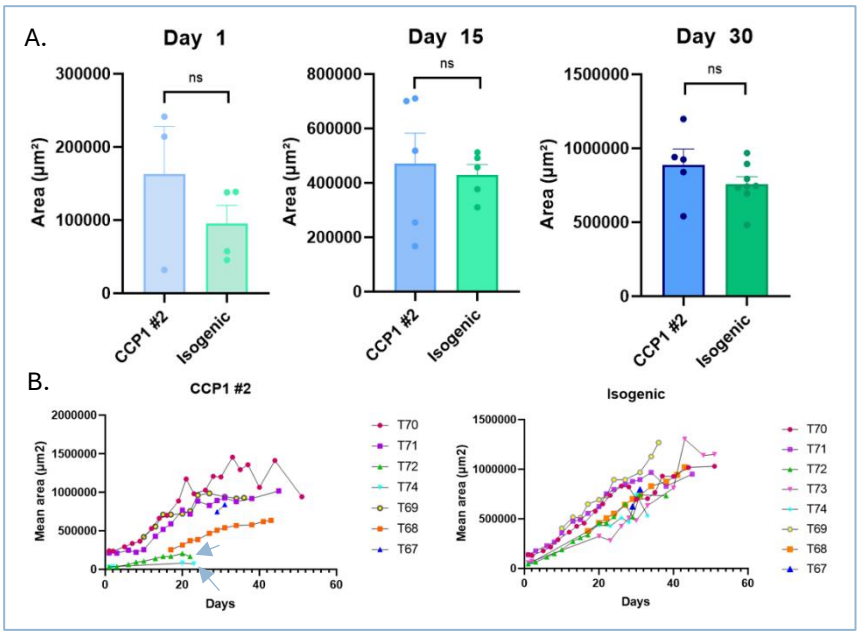

Figure 25 : Organoid growth assessment across cell lines and differentiation trials. (A) Mean organoid area (µm^2) at days 1, 15 and 30 compared across cell lines: CCP1 #2 (N = 3-5 differentiations, 5 organoids/differentiation), and CCP1 Isogenic control (N = 4-8 differentiations, 5 organoids/differentiation). Statistical comparisons were performed by t-test. ns: not significant. (B) Individual trial growth trajectories for each cell line, showing mean organoid area (µm^2) over time (days). Arrows indicate trials excluded from downstream analyses due to reduced or irregular growth trajectories. T: trial number.

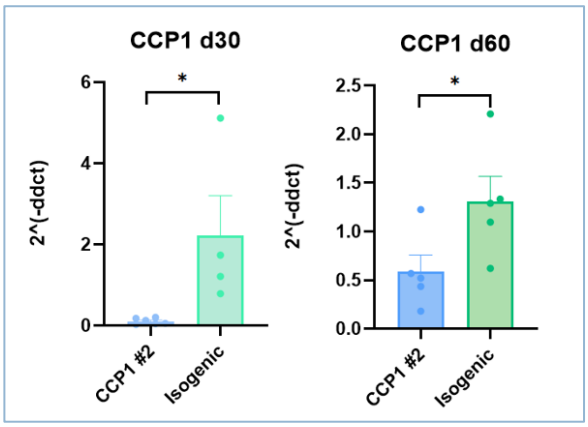

Figure 26 : CCP1 mRNA expression in mutated and isogenic cell lines at days 30 and 60. Relative CCP1 expression shown as 2^(-ΔΔCt) relative to control. Error bars represent standard error of the mean. Individual data points represent independent trial (4 to 10 organoids). Colour coding: blue = CCP1 #2; green = isogenic control. Statistical comparisons were performed by t-test. * = p<0.05.

4. RESULTS

4.1. CARACTERISATION OF THE HUMAN VENTRAL CEREBRAL ORGANOIDS

To investigate the ability of hvCOs to recapitulate human ventral forebrain development and to evaluate the impact of CCP1 LOF, we first characterized their regional identity and differentiation potential at the molecular level. During human brain development, spatial patterning of neural progenitors is tightly regulated by specific developmental cues that define distinct neuronal domains, including ventral regions such as the medial ganglionic eminence (MGE). Assessing the expression of key ventral identity and lineage-specific markers is essential to determine whether hvCOs faithfully reproduce ventral forebrain characteristics and generate the expected MGE-derived populations. Therefore, we compared mutant CCP1 #2 and isogenic control hvCOs to determine whether CCP1 LOF affects the generation of ventral forebrain-derived cell populations.

4.1.1. GROWTH EVALUATION

The quality of the hvCOs was monitored across all batches generated through growth measurement and morphological assessment. The hvCOs displayed a clustering of the cells at the center of the well, generating a round smooth hvCO growing with consistent growth (Figure 24 A-F). HvCO displaying a flat, transparent or fragmented appearance were flagged as non-viable and excluded from further analyses (Figure 24 G-H).

Analysis of hvCO growth revealed no significant differences in hvCO between the CCP1 #2 and the isogenic control across the three developmental timepoints assessed, indicating comparable overall growth between the two cell lines (Figure 25A). At batch level, however, CCP1 #2 #72 and #74 displayed reduced or irregular growth trajectories (Figure 25B) were excluded from downstream experiments to avoid introducing technical biases.

4.1.2. CCP1 EXPRESSION

CCP1 expression was assessed at the mRNA level by RT-qPCR, and at the protein level by WB and immunolabeling, to validate a reduced *CCP1* expression in the CCP1 #2 and its correction in the isogenic control.

At 30 and 60 days old, CCP1 #2 hvCOs displayed a significantly lower *CCP1* mRNA expression compared to isogenic control hvCOs (Figure 26).

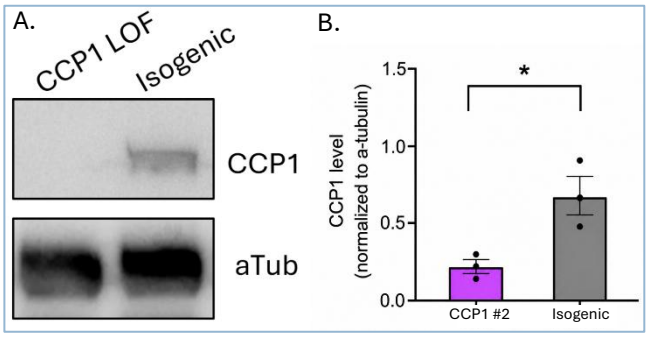

Figure 27 : CCP1 protein expression in mutated and isogenic cell lines at days 30. A. Representative WB analysis showing CCP1 protein expression in CCP1 #2 and isogenic cell line. Alpha -tubulin were used as a loading control. B. Quantification of CCP1 level normalized to alpha-tubulin expression. Error bars represent standard error of the mean. Individual data points represent independent trial (4 to 10 organoids). Colour coding: purple = CCP1 #2; grey = isogenic control. Statistical comparisons were performed by t-test. * = p<0.05.

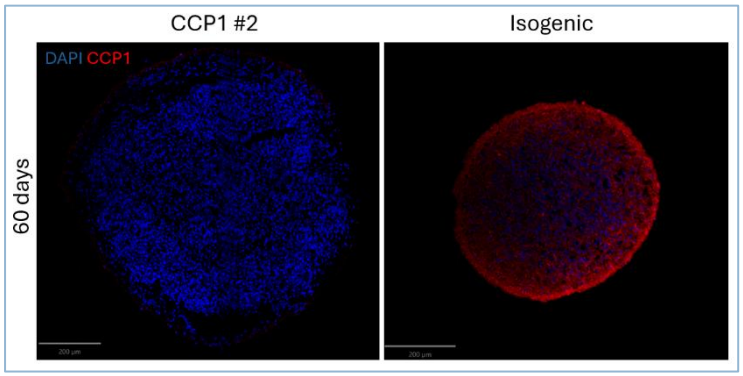

Figure 28 : CCP1 protein expression assessed by immunofluorescence in 60 days old organoids. Representative confocal images of CCP1 #2, and isogenic control hvCO sections stained for CCP1 (red) and DAPI (blue). Scale bars: CCP1 #2 = 200 µm; isogenic control = 100 µm.

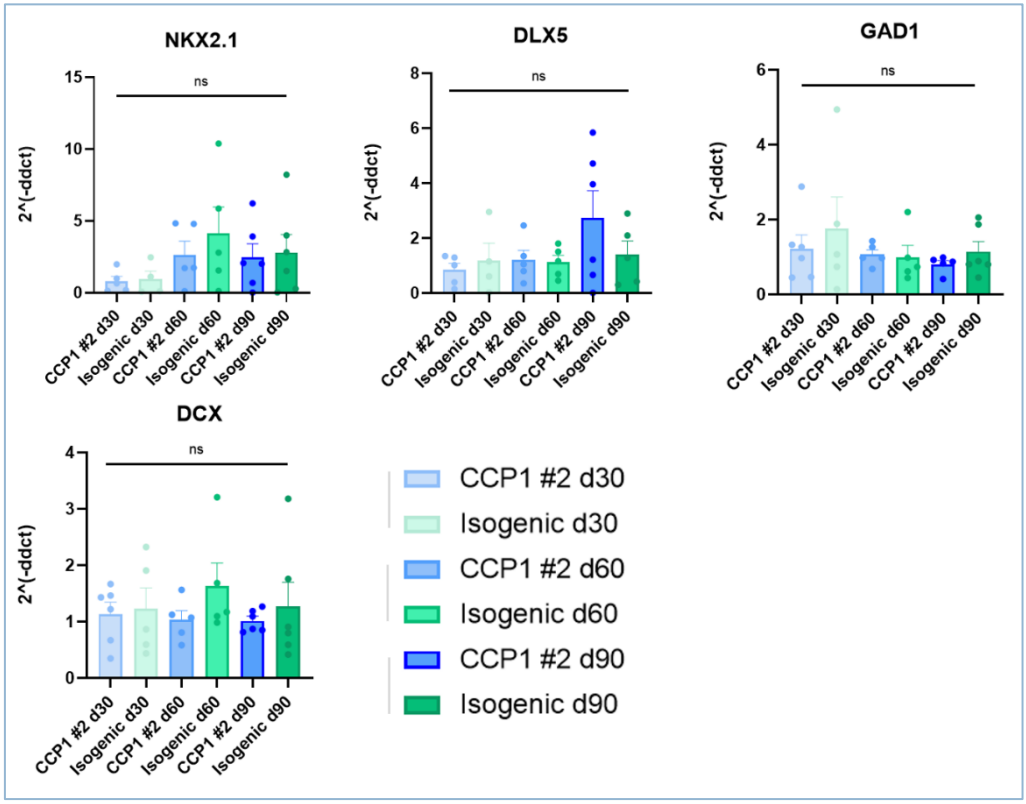

Figure 29 : qPCR analysis of ventral identity across cell lines and developmental stages. Relative gene expression of NKX2.1, DLX5 and GAD1 in CCP1 #2, and isogenic control hvCOs at days 30, 60, and 90. Expression levels are shown as 2^(-ΔΔCt) relative to control. Error bars represent standard error of the mean. Individual data points represent independent trial. Colour coding: blue = CCP1 #2 ; green = isogenic control. Timepoints: light shade = day 30; medium shade = day 60; dark shade = day 90. n = 5-6 trials. N = 4-10 organoids per condition. Statistical comparisons performed by ANOVA. ns = not significant.

CCP1 was further investigated at the protein level by WB in 30 days old hvCOs. Results indicated a significantly lower CCP1 expression in CCP1 #2 hvCOs compared to isogenic control hvCOs (Figure 27).

To complement those results, IF was performed in 60-day-old hvCOs. CCP1 signal was detected in isogenic controls but was absent in the CCP1 #2 condition, confirming loss of CCP1 protein expression (Figure 28). Together, these results confirm reduced CCP1 expression at both the mRNA and protein levels in CCP1 #2 hvCOs, validating the isogenic correction at the molecular level.

4.1.3. MATURATION ASSESSEMENT

To further monitor hvCO maturation at different developmental stages, RT-qPCR was performed on extracts from 30-, 60- and 90-day old hvCOs as they correspond to the progenitor proliferation and early neurogenesis stages of human developpement[127]. This approach allowed the investigation of gene expression dynamics across early, intermediate, and late stages of organoid maturation and differentiation. The genes panel analyzed included *NKX2.1, DLX5*, *GAD1 and DCX*. *NKX2.1*[125] and *DLX5*[128] were used as MGE ventral progenitors and post-mitotic migrating cINs, respectively. *LHX6* could also have been investigated, as it is expressed in a specific subregion of the MGE that gives rise to ventral MGE-derived interneurons[125]. *DCX* is a pan-neuronal marker and was used in this context as a marker of immature cINs[125]. *GAD1*, the gene encoding GAD67, was used as a marker of mature GABAergic cINs identity[125]. These markers are specific to ventral identity and expressed at different stages of cINs maturation, enabling the validation of hvCO patterning and developmental progression toward a ventral fate. *PAX6* could also have been analyzed to evaluate the absence of dorsal forebrain markers and further confirm the ventral identity of the generated hvCOs[125].

All genes were expressed at 30 days in both CCP1 #2 and isogenic control hvCOs. The expression level of *NKX2.1* tended to be lower in 30-day-old hvCOs compared to 60- and 90-day-old hvCOs in both CCP1 #2 and isogenic control conditions. *DLX5* expression did not show significant differences between cell lines or time points, although a tendency toward increased expression was observed in 90-day-old hvCOs. Finally, *GAD1* and *DCX* expression levels remained stable across time points, suggesting the presence of mature GABAergic cINs from the earliest timepoint analyzed (*GAD1*), and a sustained population of migrating cINs throughout the developmental window assessed (*DCX*). No statistically significant differences were observed between cell lines or time points for any of the four markers (Figure 29).

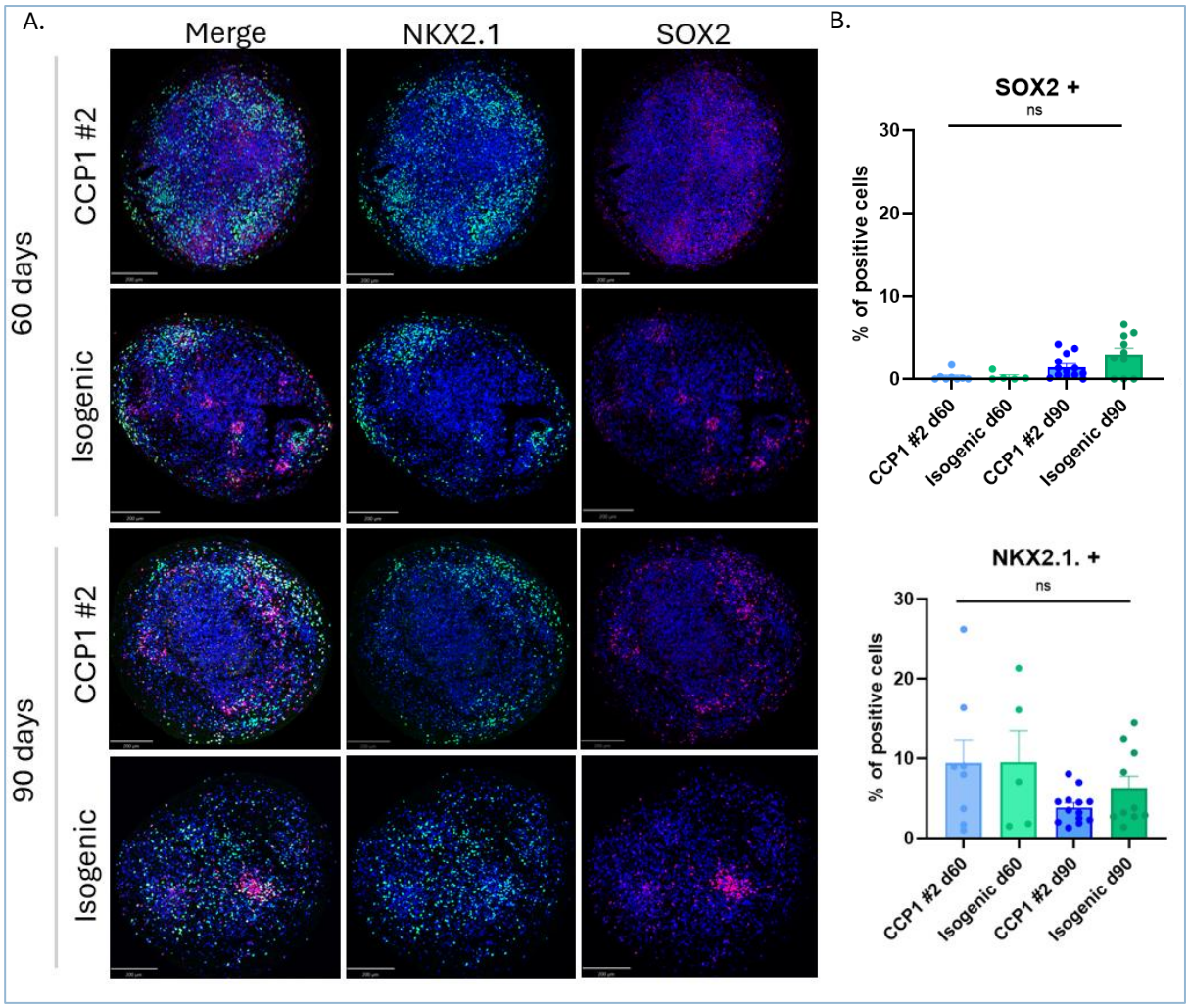

Figure 30 : Cell characterisation by NKX2.1 and SOX2 immunofluorescence in hvCOs. (A) Representative confocal images of 90 days old organoid sections from control, CCP1 LOF, and isogenic control hvCO, stained for NKX2.1 (green), SOX2 (red), and DAPI (blue). Scale bar: 200 µm. (B) Bar graphs showing the percentage of SOX2+, NKX2.1+, and NKX2.1+SOX2+ positive cells per condition at days 60 and 90. Error bars represent standard error of the mean. Individual data points represent independent organoids (N = 3-5 organoid per condition, n= 1 trial). Colour coding: blue = control; pink = CCP1 LOF; purple = isogenic control. Timepoints: light shade = day 30; medium shade = day 60; dark shade = day 90. Statistical comparisons performed by ANOVA. * $p < 0.05$.

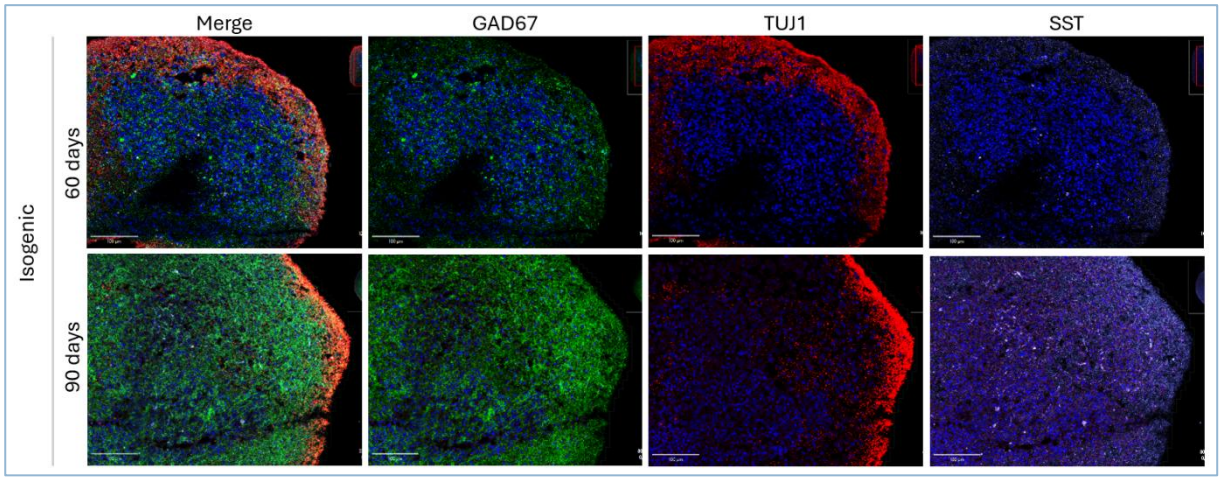

Figure 31: Cell characterisation by GAD67, TUJ1 and SST immunofluorescence in hvCOs. Representative confocal images of 60 days (top images) and 90 days (bottom images) old organoid sections from isogenic control hvCO, stained for GAD67 (green), TUJ1 (red), SST (purple), and DAPI (blue). Arrows = examples of SST+ cells. Scale bar: 100 µm

4.2. SECRETOME OPTIMISATION

4.1.4. IDENTITY CHARACTERIZATION

Cellular identity was assessed in 60- and 90-day old hvCOs to track the temporal evolution of neural cell population identities across development. Three panels were designed to characterize distinct cell populations: ventral progenitors, mature neurons and interneurons, and glial lineages respectively.

The first panel characterized ventral progenitor populations using *SOX*2 as a broad neural progenitor marker and *NKX2.1* as a marker specific to MGE progenitors[129]. *SOX2* was observed at lower levels in 60-day-old compared to 90-day-old hvCOs in both conditions, although this tendency did not reach statistical significance. Conversely, *NKX2.1* tend to decrease between 60 and 90 days in both CCP1 #2 and isogenic control hvCOs, although this difference was not statistically significant. The trend of reduction in *NKX2.1* expression may reflect a shift away from MGE-committed identity at later timepoints, sign of maturation of GABAergique cINs, warranting further investigation with additional maturation markers (Figure 30).

The second panel focused on neuronal maturation and interneuron identity (Figure 31). β-III-tubulin served as a general post-mitotic neuronal marker. GAD67 was used to identify GABAergic interneurons, and SST was used to identify a specific subtype of SST expressing cINs subtype. Staining for these markers requires further optimization for proper quantification. However, some preliminary observations could still be made. An increase in total GAD67 staining was observed between 60- and 90-day-old hvCOs, suggesting an increase in the number of GAD67 positive cells. β-III-tubulin staining was present at both timepoints but was largely restricted to the organoid periphery, limiting reliable quantification. SST staining was absent at 60 days old, but some positive cells were observed at 90 days old.

The third panel assessed the potential emergence of glial lineages using SOX10 as a marker of oligodendrocyte precursor cells (OPC). No SOX10-positive cells were detected in any condition or time point (Figure 32).

Overall, these results indicate a progressive maturation of hvCOs toward a GABAergic interneuron fate, with the emergence of more mature cIN-associated markers over time while maintaining a population of immature migrating interneurons. The presence of both migrating and differentiating GABAergic populations supports the relevance of hvCOs as a model to study cIN secretome during migration. However, the persistence of heterogeneous cell populations highlights the complexity of ventralized organoids and suggests that additional characterization

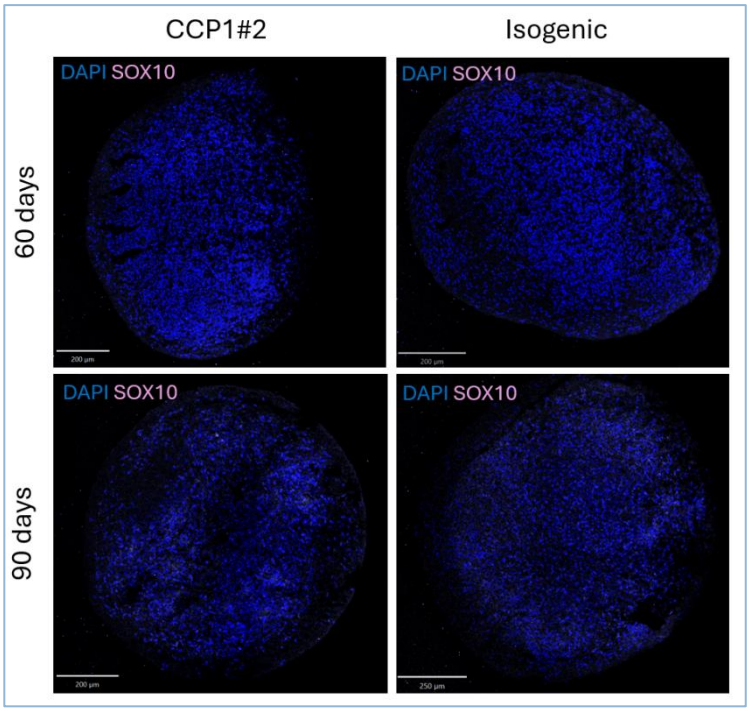

Figure 32 : SOX10 immunofluorescence in hvCOs at days 60 and 90. Representative confocal images of organoid sections from CCP1 #2, and isogenic control hvCOs at days 60 and 90, stained for SOX10 (light purple) and DAPI (blue). Scale bars : 200 µm.

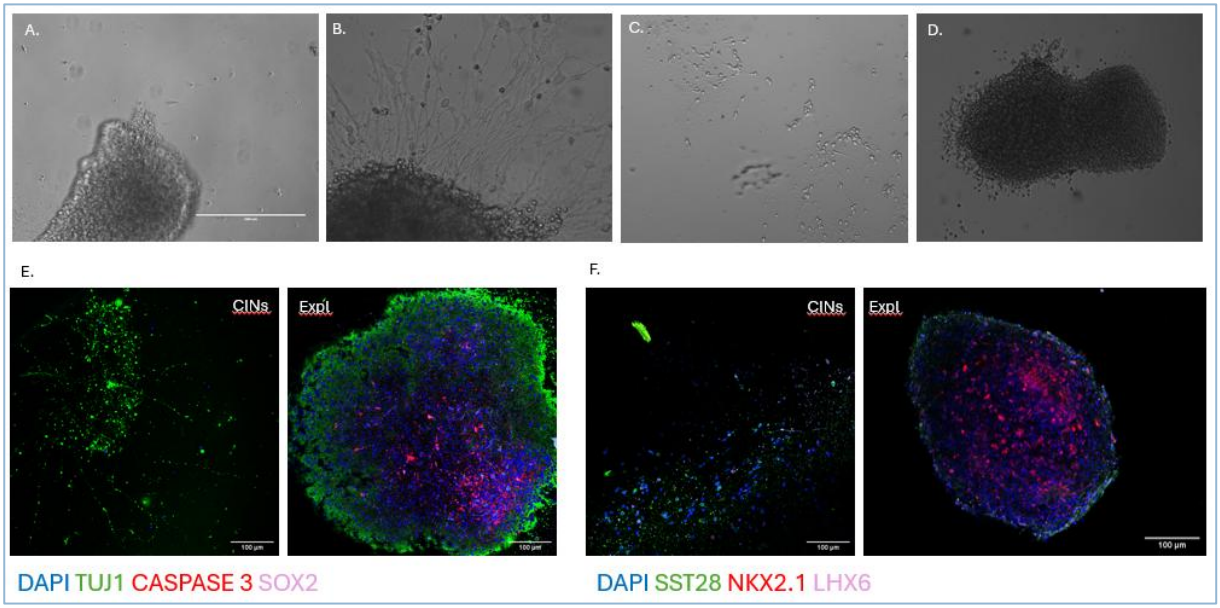

Figure 33 : Overview of the first secretome collection trial. (A) Picture of explants 2 days post plating illustrating limited cell migration observed. (B–C) Representative picture of explants 5days post plating illustrating (B) outgrowth was predominantly composed of axonal-like processes with few migrating somas. (C) cIN-enriched condition following explant removal, showing the remaining migrating cell population. (D) Progenitor-enriched condition following explant replated. (E) Immunofluorescence of both conditions stained for TUJ1 (green), Caspase-3 (red), and SOX2 (pink), counterstained with DAPI (blue). (G) Immunofluorescence of both conditions stained for SST (green), NKX2.1 (red), and LHX6 (purple), counterstained with DAPI (blue). Scale bars: 100 µm.

will be required to refine the identification of specific cIN subtypes and developmental trajectories.

4.2.1. ANALYSIS OF THE MIGRATION OF cINS FROM hvCOS

As secretome collection requires culturing cells under conditions compatible with active migration, a key preliminary step was to confirm whether cINs retain their migratory capacity when cultured on acellular N-cadherin-coated dishes, the substrate selected for secretome collection. hvCO explants plated on N-cadherin-coated dishes displayed a crown of neurons (bIII-tubulin, Fig. 33E) migrating out from the explant (Figure 33B), with morphology consistent with active migrating cINs. Separately, preliminary time-lapse (TL) observations of these explants showed the characteristic saltatory migration pattern described for cINs, supporting the suitability of this substrate for secretome collection (not shown).

The current follow up experiments will be to immunolabel the migrating neurons to confirm their expected cIN identity.

Following the characterization of the hvCO model, the investigation of diffusible cues involved in cIN communication was initiated. The objective was to establish a reliable protocol allowing the collection of the secretome from migrating cINs. Two complementary strategies were evaluated: (i) collection from migrating cells derived from hvCO explants and (ii) isolation of cIN-enriched populations by FACS prior to secretome collection. As the protocol was still under optimization, GM38-derived hvCOs were used, as they were the only available samples at that time. The intended application of this protocol was the secretome collection from CCP1 #2 and isogenic control hvCOs.

4.2.2. ANALYIS OF THE SECRETOME OF CINS USING THE EXPLANT BASED APPROACH

The first strategy aimed to collect the secretome of migrating cINs from hvCO explants plated on NCadh coating. This represented the first implementation of this methodology using hvCOs rather than mouse MGE explants in the lab. A graphical overview of the experiment is provided in Figure 20 (Material and Methods). However, as a reminder, the cIN-enriched condition is named as such because the ring of neurons migrating out of the explant is expected to be predominantly composed of cINs (to be confirmed), while the progenitor-enriched condition refers to the replated explant, expected to predominantly contain progenitors whose secretome would mask that of any other cell type.

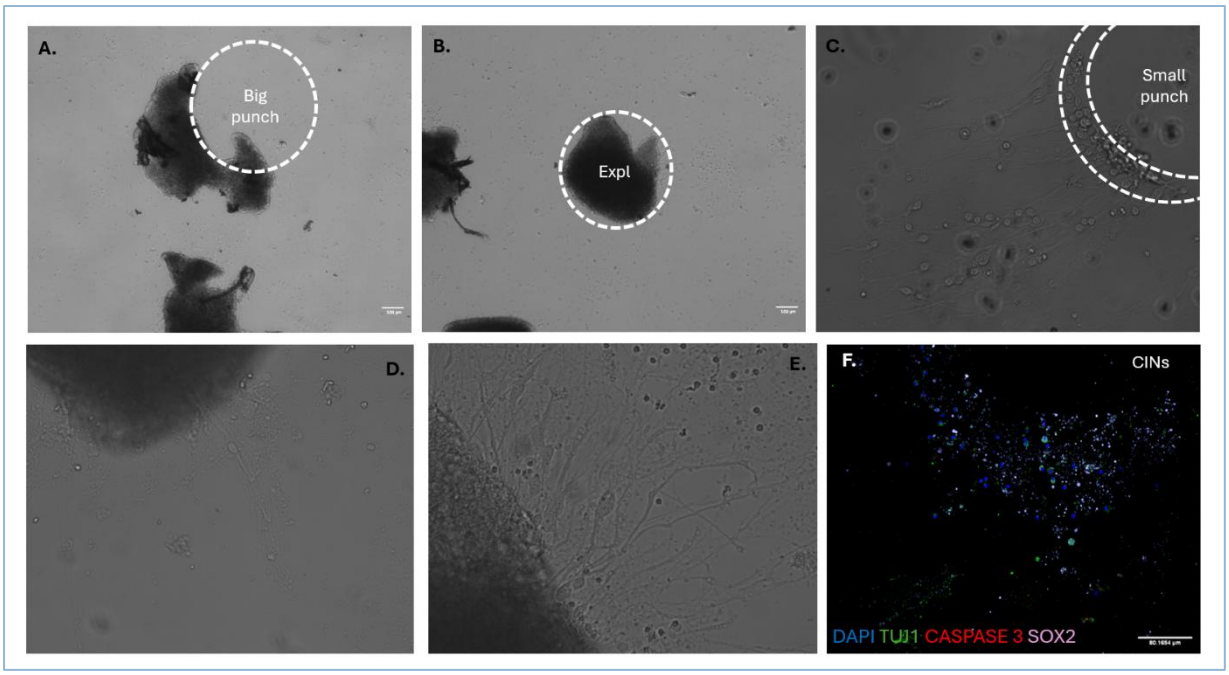

Figure 34 : Overview of the different preparation methods. A-B. Representative brightfield images of organoids explants generated using a large punch tool (dashed circle indicates punch diameter). Zoom = 4X. C. Representative brightfield image of the remaining cells (between the two dash lines in the cINs enriched condition after the small punch (dashed lines indicates punch cuts). Zoom = 10x D. Representative brightfield images of cINs migrating out of the explant after 8 days of migration in the forceps condition. Zoom = 10X. E. Representative brightfield images of cINs migrating out of the explant after 8 days of migration in the punch condition. Zoom = 20X F. Immunofluorescence staining of cIN condition of TUJ1 (green), Caspase 3 (red) and SST28 (purple) counterstained with DAPI (blue). Scale bars: 100 µm.

Two months old hvCO explants were plated in four-compartment dishes. After a few days, cells were observed migrating out of the explants (Figure 34A-C). However, the peripheral explant outgrowth was predominantly composed of long, thin processes extending from the explant, with comparatively few migrating cell bodies, a cell density that appeared insufficient for secretome collection, which requires larger numbers than TL imaging. Moreover, upon explant removal, these extensive processes covering the culture surface caused detachment of the migrating cells, preventing efficient isolation of this population.

To assess the cellular composition in both conditions, IF staining was performed using neuronal markers (TUJ1, marking beta-III-tubulin, SST and LHX6), and progenitor markers (SOX2 and NKX2.1) after the 2 starving time points. The cIN-enriched condition contained only 9.0% of TUJ1+ cells, 11.1% of SST+ cells and 5.9% of LHX6+ cells. SST+ and LHX6+ cells were mainly detected at the periphery of explants, suggesting limited antibody accessibility with the tissue, even if Triton X-100 has been used. This limitation could potentially be addressed by optimizing tissue permeabilization conditions by testing different Triton X-100 concentrations. However, the current protocol already involves relatively harsh permeabilization conditions, and further increasing Triton X-100 may compromise tissue integrity. Alternatively, an antigen retrieval step, commonly used in immunofluorescence on tissue sections, could be implemented to improve epitope accessibility and enhance antibody penetration within the explants. No SOX2+ cells and no NKX2.1+ cells were detected in the cIN-enriched condition, whereas 1.8% and 1.3% respectively were observed in the progenitor-enriched condition (Figure 34 E-F).

Cell death was assessed using Caspase-3 staining as high cell death leads to the release of cytoplasmic proteins that may mask proteins of interest in the secretome. Less than 1% of dead cells were observed in both cIN-enriched and progenitors-enriched condition, indicating that cell death was unlikely to interfere with secretome composition (Figure 34 E).

To improve hvCO explant adhesion during culture and preserve migrating cells after explant removal, two dissection strategies were compared: manual dissection with forceps and scalpel, and punch biopsy approach. The rationale was to generated explants using a large diameter punch tool (500 µm) (Figure 32 A-B) and subsequently remove the explant core using a smaller punch (350 µm) leaving the surrounding crown of migrating cells undisturbed. Migrating cells were observed in both conditions with punch-generated explants exhibiting improved adhesion and migration (Figure 34 D-E). For explant removal itself, the forceps method proved more effective, although it remained time-consuming, technically challenging, and still resulted in the removal of some migrating cells. The punch tool was difficult to manipulate precisely under the

microscope. Notably, even when substantial outgrowth was observed, the migrating populations appeared morphologically heterogeneous, suggesting the presence of mixed cell types rather than a pure cIN population (Figure 34 E).

Taken together, these results highlight the technical limitations of the explant-based approach. The adhesion of hvCO explants remained poor across all dissection methods tested, including mouse- and human-derived Ncadh coatings. The standard Ncadh coating commonly used in migration assays is derived from mouse cadherin. However, because hvCOs are of human origin, the use of a non-human one may introduce species-specific bias. To address this limitation, human NCadh has also been tested as a species-matched alternative. Only a fraction of plated explants adhered and produced migratory outgrowth. Quantitatively speaking, this set up would be sufficient to obtain data on individual migrating neurons by time-lapse imaging, but insufficient to generate secretome analysis, where many experiments would need to be aggregated. Migrating cells were also repeatedly lost during explant removal or replating. More importantly, the proportion of cIN markers among migrating cells was low and heterogeneous (TUJ1: 9.0%; SST: 11.1%; LHX6: 5.9%), suggesting that the migrating cell population reflects the overall cellular diversity of the hvCO rather than a cIN-specific. This heterogeneity appears inherent to the organoid model and was not resolved by refining the dissection protocol. The explant-based approach was therefore abandoned in favour of FACS-based isolation of cINs prior to secretome collection, to ensure that the collected secretome originates specifically from cINs.

4.2.3. ANALYSIS OF THE SECRETOME OF CINS USING THE FACS-BASED METHOD

The second strategy was developed to improve the specificity of the collected secretome by isolating cIN-enriched populations prior to plating. hvCOs were infected with a DLX5/6-GFP lentivirus, allowing the identification and isolation of cIN populations by FACS. As a reminder, a graphical abstract of the experiment is provided in Figure 20 (Materials and Methods). In this experiment, the cIN-enriched condition corresponds to DLX5/6-GFP$^+$ FACS-sorted cells, expected to be enriched in cINs, while the progenitor-enriched condition corresponds to GFP$^-$ cells, expected to be enriched in progenitors.

Two-month-old hvCOs were sectioned and infected with the DLX5/6-GFP lentivirus. Cell viability reached 99%, with approximately 5.96 x 10^5 cells/mL obtained after dissociation. A total of 63,407 GFP$^+$, corresponding to the cIN-enriched condition, and 113,697 GFP$^-$ cells, corresponding to the progenitor-enriched condition, were collected. To assess optimal density conditions, different cell quantities were plated: 30,000, 15,000, 7,500, and 5,000 cells per well for GFP$^+$ cells, and 60,000, 30,000, 15,000, and 5,000 cells per well for GFP$^-$ cells.

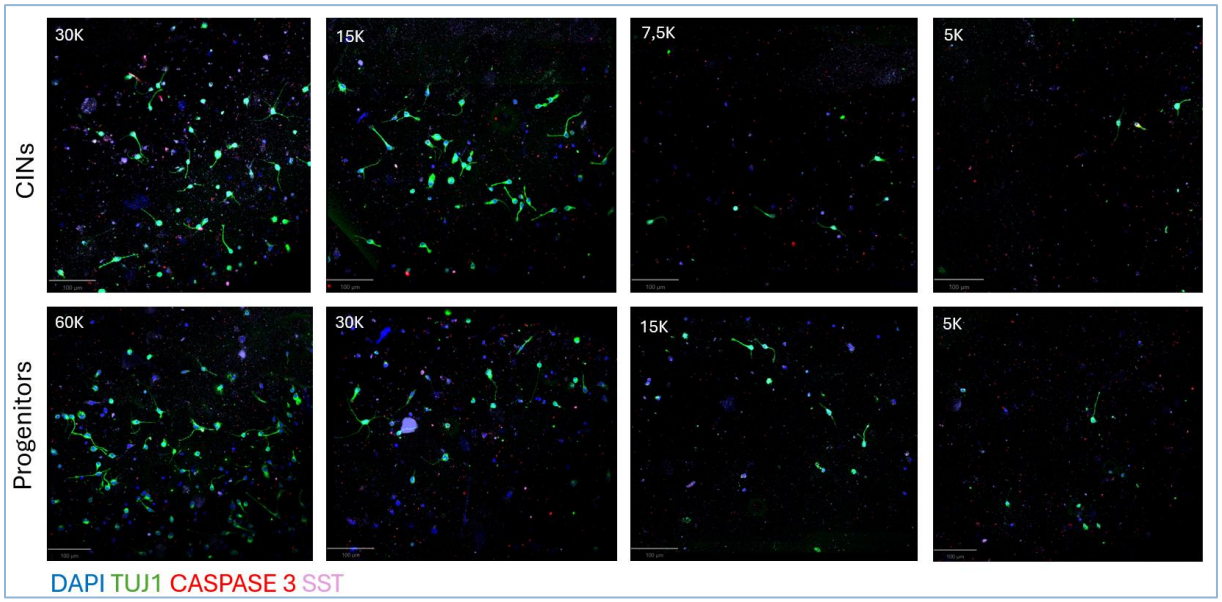

Figure 35 : Immunofluorescence images of TUJ1, Caspase 3 and SST expression in cells plated after the FACS. 30.000, 15.000, 7.500 and 5.000 cells were plated in the CINS condition (upper part). 60.000, 30.000, 15.000 and 5.000 cells were plated in the progenitor condition (lower part). TUJ1 = green, Caspase 3 = red, SST28 = purple. Scale bar = 100µm.

IF performed after de starving using Caspase-3 showed a survival rate of on average 100% regardless of cell density. To assess identity, IF staining was performed on β-III-tubulin and SST markers (Figure 35). In the cIN-enriched condition, approximately 57% of cells were positive for β-III-tubulin, and among these, 86% expressed SST. In comparison, the progenitor-enriched condition (GFP-) contained 54% β-III-tubulin+ cells, with 33% SST+ cells. The similar proportion of β-III-tubulin+ cells between the two populations suggests that DLX5/6-GFP sorting does not simply distinguish neuronal from progenitor populations. Instead, the enrichment of SST+ cells within the GFP+ fraction indicates that DLX5/6 expression preferentially labels a subset of ventral-derived interneurons, particularly the SST+ lineage. However, the presence of a substantial proportion of neuronal cells within the GFP- population highlights the heterogeneity of hvCOs, which could generate multiple ventral neuronal lineages, including non-cortical interneuron populations such as striatal neurons. Therefore, DLX5/6-GFP alone may not be sufficient to accurately isolate cIN progenitors or fully define interneuron identity in hvCOs. Additional markers or combinatorial sorting strategies will be required to refine the purification of specific cIN populations.

5. DISCUSSION

During cortical development, migrating cINs contribute to the regulation of IPs proliferation in both mouse and human models, through the release of external diffusible factors, released by cINs, whose identity remains unknown. The transient increase cortical invasion by cINs at mid-corticogenesis leads to an expansion of the IP population, thereby leading to generation of supernumerary PNs dedictade to the upper cortical layers. Such defects leads to excitatory/inhibitory imbalance in cortical circuits, potentially contributing to the emergence of neurodevelopmental disorders [60]. Thus, the objectives of my work were:1/ to characterize hvCOs as a relevant model of human-derived migrating interneurons; 2/ develop a protocol to collect the secretome of migrating cINs derived from these hvCOs. These experiments provide the basis for the future identification of the diffusible signals through which cINs influence the IP populations during human cortical development.

Over the past years, several protocols have been developed to generate ventral forebrain organoids, such as those by Bagley et al. (2017)[125] and Birey et al. (2017)[121]. The protocol used during my master thesis is adapted from previously established approaches with the objective of enhancing cINs production. Since this adaptation has not yet been independently validated in literature, a comprehensive characterization of the resulting hvCOs was performed. This characterization included the analysis of CCP1 expression, ventral forebrain identity, and neuronal maturation across three developmental time points and in two cell lines: CCP1 #2, and its isogenic control. This comparison was essential, as potential differences in hvCO composition between these lines could influence subsequent secretome analyses.

Regarding CCP1 characterization, immunofluorescence analysis revealed an absence of detectable CCP1 protein expression in CCP1 #2 hvCOs, whereas CCP1 expression was restored in the isogenic corrected line. These observations confirm that the mutation leads to a loss of CCP1 protein expression and that CRISPR-mediated correction rescues the CCP1 phenotype. Together with transcriptomic data, these results validate both cell lines as relevant models to investigate the consequences of CCP1 LOF.

The follow up work will optimize the IF protocol and the analyses will be done on three to five biological replicates to quantify the fluorescence. Furthermore, CCP1 LOF was characterized at the molecular level, but its functional consequences remain to be assessed by timelapse imaging to investigate migrating behaviour changes. Additionally, as other CCPs are known to act as deglutamylases, it could be interesting to study their expression profile in our hvCOs to rule out compensation for the absence of CCP1. Indeed, CCP1 is part of a larger family of cytosolic

carboxypeptidases involved in tubulin deglutamylation. Therefore, it would be relevant to assess whether compensatory mechanisms occur through changes in the expression of other CCP or TTLL family members. If such compensation occurs, restoration of the healthy phenotype could be expected despite CCP1 loss. Previous work by Silva et al. from the host laboratory showed that in mouse Dlx5/6-positive subpallial structures, Ccp1 and Ccp5 are among the most highly expressed cytosolic carboxypeptidases, together with Ttll1 and Ttll4. Interestingly, conditional deletion of Ccp1 in mice did not induce transcriptional compensation through other Ccps or Ttlls. However, in Ccp1 deficient mice knock out for Ttll1 and 4, a rescue of the phenotype is observed[60]. Reproducing similar analyses in the CCP1 #2 hvCO model would therefore determine whether the absence of compensation is conserved in the hvCO context.

We found that hvCOs recapitulated features of human MGE by expressing a ventral identity. Compared with conventional unguided cerebral organoid protocols, which predominantly generate dorsal cortical identities and show an early presence of NKX2.1 but a delayed arrival of GAD1[123], the early detection of these markers suggests that the hvCO protocol efficiently promotes ventral patterning. The presence of ventral identity markers at early differentiation stages indicates that the combination of patterning cues used in the hvCO model may accelerate or enhance ventral fate specification compared with spontaneous brain organoid development. Interestingly, the peak in NKX2.1 mRNA at 60 days is consistent with the IF results, where the proportion of NKX2.1+ cells also appeared to decrease between 60 and 90 days, alongside a slight increase in SOX2+ cells. This increase could imply a progressive MGE progenitor specification over time, as described in previously published ventral forebrain organoid characterizations[122]. The immunofluorescence analyses further supported the ventral identity of the hvCO model.

Taken together, the transcriptomic and immunofluorescence analyses indicate that the hvCO protocol efficiently generates ventral forebrain-like organoids containing MGE progenitors and differentiating GABAergic interneurons. The absence of major differences between CCP1-mutated and isogenic control hvCOs for ventral identity and neuronal markers suggests that CCP1 LOF does not impair early ventral specification or interneuron generation. However, whether CCP1 affects later stages of interneuron maturation, migration behavior, or functional properties remains to be investigated.

A major advantage of organoid models is the possibility to generate isogenic controls through genome editing approaches. By introducing or correcting a specific mutation while maintaining the same genetic background, phenotypic differences observed between mutant

and control hvCOs can be more confidently attributed to the mutation of interest rather than to donor-specific genetic variability. This approach strengthens the causal interpretation of disease-associated phenotypes and provides a more robust platform for dissecting molecular mechanisms underlying human diseases. For instance, in the context of ventral forebrain organoids, the comparison between CCP1 #2 and its isogenic control hvCOs revealed no significant differences in the expression of ventral identity markers, suggesting that CCP1 loss-of-function does not substantially impair ventral patterning or the generation of MGE-derived populations at the developmental stages investigated. This example highlights how isogenic organoid models allow researchers to distinguish mutation-specific effects from background-related variability and to more accurately define the contribution of a genetic alteration to a given phenotype. The combination of patient-derived organoids with CRISPR/Cas9-mediated gene correction has enabled the generation of genetically matched mutant and corrected organoids, improving the identification of mutation-driven phenotypes[130,131].

Beyond neuronal populations, the presence of additional cell types was explored to further characterize the cellular complexity of the hvCO model. In particular, the emergence of oligodendrocyte precursor cells (OPCs) was investigated. OPCs represent a late-developing glial population that appears after the generation of neural progenitors and early neuronal populations during central nervous system development. SOX10 was initially assessed as a marker of oligodendroglial lineage commitment; however, no SOX10-positive cells were detected at day 60 or day 90 in either CCP1 #2 or isogenic control hvCOs.

Although SOX10 is widely used to identify oligodendroglial cells, its expression alone is not sufficient to define OPC identity, as it is maintained throughout oligodendrocyte lineage progression. Therefore, additional markers should be analyzed to confirm the presence of OPC populations. OLIG2, a TF involved in ventral neural progenitor specification and oligodendroglial lineage initiation, could provide information regarding the emergence of oligodendroglial-competent progenitors. However, OLIG2 expression alone does not distinguish OPCs from earlier ventral progenitor populations, as is also expressed in IN precursors. Similarly, PDGFRA represents a commonly used OPC marker due to its role in OPC proliferation, survival, and migration, but should be combined with additional lineage markers to ensure accurate identification[132]. Therefore, the co-expression of OLIG2, SOX10 and PDGFRA would provide stronger evidence for the presence and maturation status of OPC populations within the hvCO model.

The absence of detectable SOX10-positive cells at the analyzed stages may reflect the developmental window captured by the current hvCO culture conditions rather than an inability of the model to generate oligodendroglial populations. Indeed, previous studies using ventralized neural organoid approaches have reported that oligodendroglial populations generally emerge at later stages of differentiation, often after day 90, as organoids undergo further maturation[133,134]. Extending the culture duration and analyzing later developmental time points would therefore be necessary to determine whether hvCOs can recapitulate later stages of glial development.

The second aim of the thesis was to investigate the secretome, more precisely secreted proteins, of migrating cINs derived from the previously characterized hvCOs. To date, most secretome analyses on the brain were focused on NSCs whether prenatally or in the neurogenic niches of adult and mainly in mice[135]. The secretome of migrating human cINs remains largely unexplored. Considering that cINs release unknown diffusible cues capable of modulating IP proliferation, identifying these signals represents an important step toward understanding interneuron-mediated regulation of cortical development[60].

To address this question, two complementary approaches were explored to isolate and characterize the cIN-derived secretome by LC/MS/MS. Importantly, LC/MS/MS require appropriate experimental controls to distinguish constitutive secretion from cell-type-specific or condition-dependent signals. Therefore, the inclusion of a progenitor-enriched condition was necessary to identify proteins specifically associated with migrating cINs rather than general organoid secretion[136].

The first strategy was based on the use of hvCO explants plated on NCadh-coated dishes, allowing migrating cells to exit the explant before separating the remaining tissue from the migrated population. The rationale was to generate two distinct conditions: one enriched in migrating interneurons and another enriched in progenitor populations. This approach was initially validated in the lab using E13.5 mouse MGE explants, demonstrating its ability to isolate migrating cINs populations. However, its application to human organoids revealed several limitations.

In contrast to mouse MGE explants, where cIN migration occurs rapidly within approximately one day, we observed that hvCO-derived interneurons required a much longer period of approximately ten days to migrate from the explants. Moreover, the number of migrating

cells was substantially lower in hvCOs compared with mouse explants. In addition, the morphology of migrating cells differed between species. In mouse explants, numerous cells with visible somas migrated away from the explant, displaying morphology consistent with migrating interneurons. In hvCOs, the migrating population was mainly composed of elongated, axon-like processes, with relatively few detectable cell bodies and some astrocyte-like cells. This suggests that prolonged migration is associated with progressive cellular differentiation toward a more mature state.

This morphology represented a major technical limitation for the subsequent isolation step. The extensive outgrowth of processes covered the culture surface and prevented efficient detachment of migrating cells. Indeed, most cell bodies remained attached to the explant and were removed together with the tissue during explant withdrawal. Consequently, even if some migrating cells remained in the cIN-enriched condition, the number of cells was likely insufficient to produce detectable amounts of secreted proteins for LC-MS/MS analysis.

Additional observations further highlighted the complexity of the human organoid system. Cells displaying larger somas and multiple short extensions, reminiscent of astrocytic morphology, were also observed, unlike in mouse MGE explants. This heterogeneity likely reflects the broader cellular diversity of hvCOs compared to dissected MGE tissue. Consistently, immunofluorescence analysis showed that only approximately 9% of migrating cells were β-III-tubulin+, suggesting that the majority of the migrating population did not correspond to post-mitotic migrating cINs, considered as a proxy for cINs. However, this likely also includes non-cortical INs, given the cellular heterogeneity of the hvCO model, meaning that "cINs" identified by this approach may not be restricted to the population of interest. Therefore, proteins detected in the collected medium would likely represent a mixture of signals from multiple cell types rather than cIN-specific secreted factors. This issue is addressed in the second method below, as single-cell transcriptomic data from the lab performed on CCP1#2 and isogenic control 3-month-old hvCOs indicated that 89% of DLX5/6-expressing interneurons correspond to cINs based on their marker expression (data not shown).

These observations represent an important limitation for interpreting secretome data, as the objective was specifically to identify diffusible signals released by migrating cINs. To overcome these limitations, several alternative approaches were tested; however, none resulted in sufficient enrichment of migrating cINs for reliable secretome collection. These results highlight the difficulty of directly adapting protocols developed in mouse embryonic tissue to

human organoid models, which display greater cellular heterogeneity and different developmental kinetics.

Considering the limitations encountered with the explant-based approach, a second strategy based on fluorescence-activated cell sorting (FACS) was explored to improve the separation between cINs and progenitor populations. This approach aimed to generate two populations with a higher cellular specificity, thereby increasing the likelihood of identifying cIN-derived secreted factors.

Immunostaining of plated cells in both conditions showed that 57% of cells were TUJ1+ in the cIN-enriched condition versus 54% in the progenitor-enriched condition, a near-identical proportion, indicating that DLX5/6-GFP sorting does not cleanly separate neurons from progenitors overall. However, among TUJ1+ cells, 86% were SST+ in the cIN-enriched condition compared to 33% in the progenitor-enriched condition. This remaining 33% SST+ population is a real problem, as the progenitor-enriched condition cannot be considered a clean control: a substantial fraction of the population corresponds to the same cIN subtype being investigated, reducing the biological difference in secreted proteins expected between conditions. This limited difference between conditions represents a major challenge for secretome analysis, as the majority of cells in both conditions do not correspond to the population of interest. Consequently, secreted proteins detected by LC-MS/MS would likely reflect a combination of signals originating from multiple cell populations, reducing the ability to identify cIN-specific factors.

Several improvements could enhance the efficiency and specificity of this approach. First, optimization of the FACS strategy, including adjustment of gating parameters, fluorescence thresholds, and doublet discrimination, could increase the purity of the sorted populations. In addition, improving the labeling strategy may provide a more efficient enrichment of cINs. Second, combining the current labeling approach with an additional marker expressed in IN progenitors or migratory cIN such as *SOX2* could increase separation between populations. In addition, investigating other migrating populations, such as *DCX*-positive neuronal populations, could help determine the extent to which non-cIN cells contribute to the secretome profile within the GFP+ population.

Regarding the progenitor-enriched condition, the presence of TUJ1-positive cells suggests that this population was not exclusively composed of progenitors. Since βIII-tubulin is generally associated with neuronal differentiation rather than progenitor identity, these cells may correspond to other neuronal populations, potentially including striatal- and olfactory bulb-like interneurons, as suggested by preliminary observations by single cell RNA sequencing performed

on hvCOs from the laboratory. Therefore, further characterization of both conditions will be required before interpreting secretome differences between them.

An important limitation of the current strategy was the relatively low proportion of GFP-positive cells obtained after lentiviral infection. This could result either from suboptimal infection efficiency or from biological variability in the generation of ventral populations within the hvCO model. In particular, differences in patterning efficiency in CCP1 #2 and isogenic control hvCOs may influence the proportion of cINs available for isolation. Increasing the efficiency of interneuron specification during organoid generation may therefore represent an essential step toward improving secretome collection.

Following FACS, the experimental design included two starvation periods of 6 and 10 hours before secretome collection. These time-points were selected based on previous mouse MGE experiments to maintain comparability between species. Serum starvation is commonly used in secretome studies to reduce the presence of abundant serum-derived proteins and improve the detection of low-abundance secreted factors. However, the duration of serum-free incubation represents a critical balance between increasing proteomic sensitivity and maintaining cellular integrity[136]. Longer starvation periods may induce cellular stress, alter gene expression profiles, or promote differentiation processes, thereby affecting the biological relevance of the collected secretome. In this context, shorter incubation periods were selected to preserve the migratory phenotype of cINs while allowing sufficient accumulation of extracellular proteins[136]. The use of two time points additionally enables the evaluation of secretion kinetics, helping to determine whether specific proteins are rapidly released or progressively accumulate in the extracellular environment.

Although both starvation conditions could not be fully evaluated within the timeframe of this thesis, cell viability was assessed after the “short” 6-hour starvation period. A critical issue in secretome studies is the contamination of extracellular samples by intracellular proteins released during cell death. Even under optimal culture conditions, a fraction of cells may undergo apoptosis or necrosis, leading to the release of intracellular proteins that can interfere with LC-MS/MS interpretation[136]. The mass spectrometry facility established a maximum acceptable cell death threshold of 5% for sample analysis. Importantly, the post-FACS cIN-enriched condition displayed less than 1% cell death, indicating that the collected medium would likely reflect active secretion rather than extensive cellular damage. This result supports the feasibility of the FACS-based strategy as the most promising approach for future secretome experiments.

Although secretome analysis could not be completed during this thesis, the establishment and optimization of the protocol represent an important methodological step toward identifying cIN-derived extracellular signals. Among the approaches tested, the FACS-based strategy appeared the most promising due to its ability to enrich cIN populations while maintaining high cell viability. Nevertheless, additional optimization will be required, particularly to improve interneuron labeling efficiency, increase the proportion of cINs generated within hvCOs, and confirm that sorted cINs retain their migratory properties after plating.

Once fully established, this protocol will enable the comparison of secretomes derived from cIN-enriched and progenitor-enriched conditions in CCP1 #2 and isogenic control hvCOs. By identification of differentially secreted proteins, it is expected to found proteins related to cell proliferation or migration.

In addition to investigating proteins, it could be valuable to also study microRNAs, growth factors, chemokine, circDNA, cytokines, and metalloproteinases [135,137]. The cINs secretome could act through different modes of intercellular communication: autocrine, paracrine and bidirectional. In our context, autocrine signaling is defined as secreted signals acting back on cIN itself; paracrine signaling corresponds to secreted signals acting on neighboring cells, including cells from other lineages (e.g. PNs, microglia) or progenitors; and reciprocal (bidirectional) paracrine signaling, whereby cINs and IPs mutually influence each other's behavior. The cINs secretome could be released via extracellular vesicles (EV) which are classified into two main categories: large EVs, known as microvesicles (100–1000 nm in diameter), and small EVs, referred to as exosomes (40–100 nm in diameter)[137]. Soluble proteins are secreted via exocytosis of secretory vesicles and miRNAs, are packaged into small, lipid-bound EVs (e.g. exosomes) before release into the extracellular space[135].

In the NSCs secretome, VEGF, BDNF, Tenascin-C and IGF-1/2 are present and participate to proliferation and differentiation of NSCs. CNTF, LIF and IGF1 promote the migration of NSCs[137]. Given the developmental immaturity and cellular complexity of organoid models, the cIN secretome may contain factors involved in proliferation, migration and differentiation, but their interpretation will require careful validation to distinguish cIN-specific signals from broader organoid-associated responses.

Future perspective, once the secretome is collected and secreted proteins investigated bibliographically, is to determine interesting candidates in the context of IP proliferation. The STRING Data Resource Website would be a valuable tool to visualize protein interactomes and perform gene ontology (GO) analyses. GO is a comprehensive resource concerning the functions

of genes and gene products (proteins and noncoding RNAs)[138]. To strengthen the candidate list, similar analyses of scRNA-seq data could be performed. Candidate of interest could be assessed functionally in organoids models to evaluate the impact on progenitors and subsequent neuronal population. Additionally, as a first step to assess the global biological relevance of the secretome, it would be interesting to test the effect of secretome from a control cell line versus cell lines mutated for candidate genes on cortical progenitors, to evaluate broad effects on their proliferation or differentiation. However, as this approach would reflect the combined effect of all secretome changes induced by the mutation rather than the candidate protein specifically, this could be complemented by testing the purified candidate molecule, or a synthetic analogue/agonist, if the protein itself is not isolable, directly on progenitors, providing a more targeted assessment of its individual contribution.

Overall, my thesis established and characterized a human ventral cortical organoid model suitable for studying CCP1 LOF and cortical interneuron development. Furthermore, it provided the foundation for the future identification of interneuron-derived extracellular signals regulating cortical progenitor populations. Although additional optimization is required before secretome profiling can be performed, the approaches developed here represent an important step toward understanding human-specific mechanisms of interneuron-mediated cortical development.

6. BIBLIOGRAPHY

(1) Stiles, J.; Jernigan, T. L. The Basics of Brain Development. *Neuropsychol Rev* **2010**, *20* (4), 327–348. https://doi.org/10.1007/s11065-010-9148-4.

(2) Chen, V. S.; Morrison, J. P.; Southwell, M. F.; Foley, J. F.; Bolon, B.; Elmore, S. A. Histology Atlas of the Developing Prenatal and Postnatal Mouse Central Nervous System, with Emphasis on Prenatal Days E7.5 to E18.5. *Toxicol Pathol* **2017**, *45* (6), 705–744. https://doi.org/10.1177/0192623317728134.

(3) Rubenstein, J. L. R.; Shimamura, K.; Martinez, S.; Puelles, L. REGIONALIZATION OF THE PROSENCEPHALIC NEURAL PLATE. *Annu. Rev. Neurosci.* **1998**, *21* (1), 445–477. https://doi.org/10.1146/annurev.neuro.21.1.445.

(4) Evans, A. E.; Kelly, C. M.; Precious, S. V.; Rosser, A. E. Molecular Regulation of Striatal Development: A Review. *Anatomy Research International* **2012**, *2012*, 1–14. https://doi.org/10.1155/2012/106529.

(5) Taverna, E.; Götz, M.; Huttner, W. B. The Cell Biology of Neurogenesis: Toward an Understanding of the Development and Evolution of the Neocortex. *Annu. Rev. Cell Dev. Biol.* **2014**, *30* (1), 465–502. https://doi.org/10.1146/annurev-cellbio-101011-155801.

(6) Gressens, P. Le développement du système nerveux : de la neurogénèse à la structuration des réseaux neuronaux. *Bulletin de l'Académie Nationale de Médecine* **2021**, *205* (8), 901–907. https://doi.org/10.1016/j.banm.2021.05.014.

(7) Di Bella, D. J.; Domínguez-Iturza, N.; Brown, J. R.; Arlotta, P. Making Ramón y Cajal Proud: Development of Cell Identity and Diversity in the Cerebral Cortex. *Neuron* **2024**, *112* (13), 2091–2111. https://doi.org/10.1016/j.neuron.2024.04.021.

(8) Pilaz, L.; Silver, D. L. Post-transcriptional Regulation in Corticogenesis: How RNA-binding Proteins Help Build the Brain. *WIREs RNA* **2015**, *6* (5), 501–515. https://doi.org/10.1002/wrna.1289.

(9) Uzquiano, A.; Gladwyn-Ng, I.; Nguyen, L.; Reiner, O.; Götz, M.; Matsuzaki, F.; Francis, F. Cortical Progenitor Biology: Key Features Mediating Proliferation versus Differentiation. *Journal of Neurochemistry* **2018**, *146* (5), 500–525. https://doi.org/10.1111/jnc.14338.

(10) Huang, Z. Molecular Regulation of Neuronal Migration during Neocortical Development. *Molecular and Cellular Neuroscience* **2009**, *42* (1), 11–22. https://doi.org/10.1016/j.mcn.2009.06.003.

(11) Rakic, P. Neurons in Rhesus Monkey Visual Cortex: Systematic Relation between Time of Origin and Eventual Disposition. *Science* **1974**, *183* (4123), 425–427. https://doi.org/10.1126/science.183.4123.425.

(12) Rice, D. S.; Curran, T. Role of the Reelin Signaling Pathway in Central Nervous System Development. *Annu. Rev. Neurosci.* **2001**, *24* (1), 1005–1039. https://doi.org/10.1146/annurev.neuro.24.1.1005.

(13) Alcántara, S.; Ruiz, M.; D'Arcangelo, G.; Ezan, F.; De Lecea, L.; Curran, T.; Sotelo, C.; Soriano, E. Regional and Cellular Patterns of *Reelin* mRNA Expression in the Forebrain of the Developing and Adult Mouse. *J. Neurosci.* **1998**, *18* (19), 7779–7799. https://doi.org/10.1523/JNEUROSCI.18-19-07779.1998.

(14) Ge, W.-P.; Miyawaki, A.; Gage, F. H.; Jan, Y. N.; Jan, L. Y. Local Generation of Glia Is a Major Astrocyte Source in Postnatal Cortex. *Nature* **2012**, *484* (7394), 376–380. https://doi.org/10.1038/nature10959.

(15) Greig, L. C.; Woodworth, M. B.; Galazo, M. J.; Padmanabhan, H.; Macklis, J. D. Molecular Logic of Neocortical Projection Neuron Specification, Development and Diversity. *Nat Rev Neurosci* **2013**, *14* (11), 755–769. https://doi.org/10.1038/nrn3586.

(16) Brady, M. V.; Vaccarino, F. M. Role of SHH in Patterning Human Pluripotent Cells towards Ventral Forebrain Fates. *Cells* **2021**, *10* (4), 914. https://doi.org/10.3390/cells10040914.

(17) Wilson, L.; Maden, M. The Mechanisms of Dorsoventral Patterning in the Vertebrate Neural Tube. *Developmental Biology* **2005**, *282* (1), 1–13. https://doi.org/10.1016/j.ydbio.2005.02.027.

(18) Lupo, G.; Harris, W. A.; Lewis, K. E. Mechanisms of Ventral Patterning in the Vertebrate Nervous System. *Nat Rev Neurosci* **2006**, *7* (2), 103–114. https://doi.org/10.1038/nrn1843.

(19) Gámez, B.; Rodriguez-Carballo, E.; Ventura, F. BMP Signaling in Telencephalic Neural Cell Specification and Maturation. *Front. Cell. Neurosci.* **2013**, *7*. https://doi.org/10.3389/fncel.2013.00087.

(20) Chenn, A. Wnt/Beta-Catenin Signaling in Cerebral Cortical Development. *Organogenesis* **2008**, *4* (2), 76–80. https://doi.org/10.4161/org.4.2.5852.

(21) Harrison-Uy, S. J.; Pleasure, S. J. Wnt Signaling and Forebrain Development. *Cold Spring Harb Perspect Biol* **2012**, *4* (7), a008094. https://doi.org/10.1101/cshperspect.a008094.

(22) Zeiss, C. J. Comparative Milestones in Rodent and Human Postnatal Central Nervous System Development. *Toxicol Pathol* **2021**, *49* (8), 1368–1373. https://doi.org/10.1177/01926233211046933.

(23) Yang, Z. The Principle of Cortical Development and Evolution. *Neurosci. Bull.* **2025**, *41* (3), 461–485. https://doi.org/10.1007/s12264-024-01259-2.

(24) Mason, J. O.; Price, D. J. Building Brains in a Dish: Prospects for Growing Cerebral Organoids from Stem Cells. *Neuroscience* **2016**, *334*, 105–118. https://doi.org/10.1016/j.neuroscience.2016.07.048.

(25) Radonjić, N. V.; Ayoub, A. E.; Memi, F.; Yu, X.; Maroof, A.; Jakovcevski, I.; Anderson, S. A.; Rakic, P.; Zecevic, N. Diversity of Cortical Interneurons in Primates: The Role of the Dorsal Proliferative Niche. *Cell Reports* **2014**, *9* (6), 2139–2151. https://doi.org/10.1016/j.celrep.2014.11.026.

(26) Muñoz-Manchado, A. B.; Bengtsson Gonzales, C.; Zeisel, A.; Munguba, H.; Bekkouche, B.; Skene, N. G.; Lönnerberg, P.; Ryge, J.; Harris, K. D.; Linnarsson, S.; Hjerling-Leffler, J. Diversity of Interneurons in the Dorsal Striatum Revealed by Single-Cell RNA Sequencing and PatchSeq. *Cell Reports* **2018**, *24* (8), 2179-2190.e7. https://doi.org/10.1016/j.celrep.2018.07.053.

(27) Sultan, K. T.; Shi, S. Generation of Diverse Cortical Inhibitory Interneurons. *WIREs Developmental Biology* **2018**, *7* (2), e306. https://doi.org/10.1002/wdev.306.

(28) Riedemann, T. Diversity and Function of Somatostatin-Expressing Interneurons in the Cerebral Cortex. *IJMS* **2019**, *20* (12), 2952. https://doi.org/10.3390/ijms20122952.

(29) Jorstad, N. L.; Close, J.; Johansen, N.; Yanny, A. M.; Barkan, E. R.; Travaglini, K. J.; Bertagnolli, D.; Campos, J.; Casper, T.; Crichton, K.; Dee, N.; Ding, S.-L.; Gelfand, E.; Goldy, J.; Hirschstein, D.; Kiick, K.; Kroll, M.; Kunst, M.; Lathia, K.; Long, B.; Martin, N.; McMillen, D.; Pham, T.; Rimorin, C.; Ruiz, A.; Shapovalova, N.; Shehata, S.; Siletti, K.; Somasundaram, S.; Sulc, J.; Tieu, M.; Torkelson, A.; Tung, H.; Callaway, E. M.; Hof, P. R.; Keene, C. D.; Levi, B. P.; Linnarsson, S.; Mitra, P. P.; Smith, K.; Hodge, R. D.; Bakken, T. E.; Lein, E. S. Transcriptomic Cytoarchitecture Reveals Principles of Human Neocortex Organization. *Science* **2023**, *382* (6667), eadf6812. https://doi.org/10.1126/science.adf6812.

(30) Cadwell, C. R.; Bhaduri, A.; Mostajo-Radji, M. A.; Keefe, M. G.; Nowakowski, T. J. Development and Arealization of the Cerebral Cortex. *Neuron* **2019**, *103* (6), 980–1004. https://doi.org/10.1016/j.neuron.2019.07.009.

(31) Paredes, M. F.; James, D.; Gil-Perotin, S.; Kim, H.; Cotter, J. A.; Ng, C.; Sandoval, K.; Rowitch, D. H.; Xu, D.; McQuillen, P. S.; Garcia-Verdugo, J.-M.; Huang, E. J.; Alvarez-Buylla, A. Extensive Migration of

Young Neurons into the Infant Human Frontal Lobe. *Science* **2016**, *354* (6308), aaf7073. https://doi.org/10.1126/science.aaf7073.

(32) Marín, O. Development of GABAergic Interneurons in the Human Cerebral Cortex. *Eur J of Neuroscience* **2025**, *61* (9), e70136. https://doi.org/10.1111/ejn.70136.

(33) Feng, X.; Gao, Y.; Chu, F.; Shan, Y.; Liu, M.; Wang, Y.; Zhu, Y.; Lu, Q.; Li, M. Cortical Arealization of Interneurons Defines Shared and Distinct Molecular Programs in Developing Human and Macaque Brains. *Nat Commun* **2025**, *16* (1), 672. https://doi.org/10.1038/s41467-025-56058-8.

(34) Shi, Y.; Wang, M.; Mi, D.; Lu, T.; Wang, B.; Dong, H.; Zhong, S.; Chen, Y.; Sun, L.; Zhou, X.; Ma, Q.; Liu, Z.; Wang, W.; Zhang, J.; Wu, Q.; Marín, O.; Wang, X. Mouse and Human Share Conserved Transcriptional Programs for Interneuron Development. *Science* **2021**, *374* (6573), eabj6641. https://doi.org/10.1126/science.abj6641.

(35) Llorca, A.; Deogracias, R. Origin, Development, and Synaptogenesis of Cortical Interneurons. *Front. Neurosci.* **2022**, *16*, 929469. https://doi.org/10.3389/fnins.2022.929469.

(36) Pan, Y.-H.; Wu, N.; Yuan, X.-B. Toward a Better Understanding of Neuronal Migration Deficits in Autism Spectrum Disorders. *Front. Cell Dev. Biol.* **2019**, *7*, 205. https://doi.org/10.3389/fcell.2019.00205.

(37) Moffat, J. J.; Ka, M.; Jung, E.-M.; Kim, W.-Y. Genes and Brain Malformations Associated with Abnormal Neuron Positioning. *Mol Brain* **2015**, *8* (1), 72. https://doi.org/10.1186/s13041-015-0164-4.

(38) Stouffer, M. A.; Golden, J. A.; Francis, F. Neuronal Migration Disorders: Focus on the Cytoskeleton and Epilepsy. *Neurobiology of Disease* **2016**, *92*, 18–45. https://doi.org/10.1016/j.nbd.2015.08.003.

(39) DeFelipe, J.; López-Cruz, P. L.; Benavides-Piccione, R.; Bielza, C.; Larrañaga, P.; Anderson, S.; Burkhalter, A.; Cauli, B.; Fairén, A.; Feldmeyer, D.; Fishell, G.; Fitzpatrick, D.; Freund, T. F.; González-Burgos, G.; Hestrin, S.; Hill, S.; Hof, P. R.; Huang, J.; Jones, E. G.; Kawaguchi, Y.; Kisvárday, Z.; Kubota, Y.; Lewis, D. A.; Marín, O.; Markram, H.; McBain, C. J.; Meyer, H. S.; Monyer, H.; Nelson, S. B.; Rockland, K.; Rossier, J.; Rubenstein, J. L. R.; Rudy, B.; Scanziani, M.; Shepherd, G. M.; Sherwood, C. C.; Staiger, J. F.; Tamás, G.; Thomson, A.; Wang, Y.; Yuste, R.; Ascoli, G. A. New Insights into the Classification and Nomenclature of Cortical GABAergic Interneurons. *Nat Rev Neurosci* **2013**, *14* (3), 202–216. https://doi.org/10.1038/nrn3444.

(40) Molyneaux, B. J.; Arlotta, P.; Menezes, J. R. L.; Macklis, J. D. Neuronal Subtype Specification in the Cerebral Cortex. *Nat Rev Neurosci* **2007**, *8* (6), 427–437. https://doi.org/10.1038/nrn2151.

(41) Tasic, B.; Menon, V.; Nguyen, T. N.; Kim, T. K.; Jarsky, T.; Yao, Z.; Levi, B.; Gray, L. T.; Sorensen, S. A.; Dolbeare, T.; Bertagnolli, D.; Goldy, J.; Shapovalova, N.; Parry, S.; Lee, C.; Smith, K.; Bernard, A.; Madisen, L.; Sunkin, S. M.; Hawrylycz, M.; Koch, C.; Zeng, H. Adult Mouse Cortical Cell Taxonomy Revealed by Single Cell Transcriptomics. *Nat Neurosci* **2016**, *19* (2), 335–346. https://doi.org/10.1038/nn.4216.

(42) Tasic, B.; Yao, Z.; Graybuck, L. T.; Smith, K. A.; Nguyen, T. N.; Bertagnolli, D.; Goldy, J.; Garren, E.; Economo, M. N.; Viswanathan, S.; Penn, O.; Bakken, T.; Menon, V.; Miller, J.; Fong, O.; Hirokawa, K. E.; Lathia, K.; Rimorin, C.; Tieu, M.; Larsen, R.; Casper, T.; Barkan, E.; Kroll, M.; Parry, S.; Shapovalova, N. V.; Hirschstein, D.; Pendergraft, J.; Sullivan, H. A.; Kim, T. K.; Szafer, A.; Dee, N.; Groblewski, P.; Wickersham, I.; Cetin, A.; Harris, J. A.; Levi, B. P.; Sunkin, S. M.; Madisen, L.; Daigle, T. L.; Looger, L.; Bernard, A.; Phillips, J.; Lein, E.; Hawrylycz, M.; Svoboda, K.; Jones, A. R.; Koch, C.; Zeng, H. Shared and Distinct Transcriptomic Cell Types across Neocortical Areas. *Nature* **2018**, *563* (7729), 72–78. https://doi.org/10.1038/s41586-018-0654-5.

(43) Gouwens, N. W.; Sorensen, S. A.; Berg, J.; Lee, C.; Jarsky, T.; Ting, J.; Sunkin, S. M.; Feng, D.; Anastassiou, C. A.; Barkan, E.; Bickley, K.; Blesie, N.; Braun, T.; Brouner, K.; Budzillo, A.; Caldejon, S.;

Casper, T.; Castelli, D.; Chong, P.; Crichton, K.; Cuhaciyan, C.; Daigle, T. L.; Dalley, R.; Dee, N.; Desta, T.; Ding, S.-L.; Dingman, S.; Doperalski, A.; Dotson, N.; Egdorf, T.; Fisher, M.; De Frates, R. A.; Garren, E.; Garwood, M.; Gary, A.; Gaudreault, N.; Godfrey, K.; Gorham, M.; Gu, H.; Habel, C.; Hadley, K.; Harrington, J.; Harris, J. A.; Henry, A.; Hill, D.; Josephsen, S.; Kebede, S.; Kim, L.; Kroll, M.; Lee, B.; Lemon, T.; Link, K. E.; Liu, X.; Long, B.; Mann, R.; McGraw, M.; Mihalas, S.; Mukora, A.; Murphy, G. J.; Ng, L.; Ngo, K.; Nguyen, T. N.; Nicovich, P. R.; Oldre, A.; Park, D.; Parry, S.; Perkins, J.; Potekhina, L.; Reid, D.; Robertson, M.; Sandman, D.; Schroedter, M.; Slaughterbeck, C.; Soler-Llavina, G.; Sulc, J.; Szafer, A.; Tasic, B.; Taskin, N.; Teeter, C.; Thatra, N.; Tung, H.; Wakeman, W.; Williams, G.; Young, R.; Zhou, Z.; Farrell, C.; Peng, H.; Hawrylycz, M. J.; Lein, E.; Ng, L.; Arkhipov, A.; Bernard, A.; Phillips, J. W.; Zeng, H.; Koch, C. Classification of Electrophysiological and Morphological Neuron Types in the Mouse Visual Cortex. *Nat Neurosci* **2019**, *22* (7), 1182–1195. https://doi.org/10.1038/s41593-019-0417-0.

(44) Heins, N.; Cremisi, F.; Malatesta, P.; Gangemi, R. M. R.; Corte, G.; Price, J.; Goudreau, G.; Gruss, P.; Götz, M. Emx2 Promotes Symmetric Cell Divisions and a Multipotential Fate in Precursors from the Cerebral Cortex. *Molecular and Cellular Neuroscience* **2001**, *18* (5), 485–502. https://doi.org/10.1006/mcne.2001.1046.

(45) Georgala, P. A.; Manuel, M.; Price, D. J. The Generation of Superficial Cortical Layers Is Regulated by Levels of the Transcription Factor Pax6. *Cerebral Cortex* **2011**, *21* (1), 81–94. https://doi.org/10.1093/cercor/bhq061.

(46) Porter, F. D.; Drago, J.; Xu, Y.; Cheema, S. S.; Wassif, C.; Huang, S.-P.; Lee, E.; Grinberg, A.; Massalas, J. S.; Bodine, D.; Alt, F.; Westphal, H. *Lhx2* , a LIM Homeobox Gene, Is Required for Eye, Forebrain, and Definitive Erythrocyte Development. *Development* **1997**, *124* (15), 2935–2944. https://doi.org/10.1242/dev.124.15.2935.

(47) Dou, C.-L. Dual Role of Brain Factor-1 in Regulating Growth and Patterning of the Cerebral Hemispheres. *Cerebral Cortex* **1999**, *9* (6), 543–550. https://doi.org/10.1093/cercor/9.6.543.

(48) Mallamaci, A.; Mercurio, S.; Muzio, L.; Cecchi, C.; Pardini, C. L.; Gruss, P.; Boncinelli, E. The Lack of Emx2 Causes Impairment of Reelin Signaling and Defects of Neuronal Migration in the Developing Cerebral Cortex. *J Neurosci* **2000**, *20* (3), 1109–1118. https://doi.org/10.1523/JNEUROSCI.20-03-01109.2000.

(49) Schmahl, W.; Knoedlseder, M.; Favor, J.; Davidson, D. Defects of Neuronal Migration and the Pathogenesis of Cortical Malformations Are Associated with Small Eye (Sey) in the Mouse, a Point Mutation at the Pax-6-Locus. *Acta Neuropathol* **1993**, *86* (2), 126–135. https://doi.org/10.1007/BF00334879.

(50) Bulchand, S.; Grove, E. A.; Porter, F. D.; Tole, S. LIM-Homeodomain Gene Lhx2 Regulates the Formation of the Cortical Hem. *Mechanisms of Development* **2001**, *100* (2), 165–175. https://doi.org/10.1016/S0925-4773(00)00515-3.

(51) Muzio, L.; Mallamaci, A. *Foxg1* Confines Cajal-Retzius Neuronogenesis and Hippocampal Morphogenesis to the Dorsomedial Pallium. *J. Neurosci.* **2005**, *25* (17), 4435–4441. https://doi.org/10.1523/JNEUROSCI.4804-04.2005.

(52) Lim, L.; Mi, D.; Llorca, A.; Marín, O. Development and Functional Diversification of Cortical Interneurons. *Neuron* **2018**, *100* (2), 294–313. https://doi.org/10.1016/j.neuron.2018.10.009.

(53) Gouwens, N. W.; Sorensen, S. A.; Baftizadeh, F.; Budzillo, A.; Lee, B. R.; Jarsky, T.; Alfiler, L.; Baker, K.; Barkan, E.; Berry, K.; Bertagnolli, D.; Bickley, K.; Bomben, J.; Braun, T.; Brouner, K.; Casper, T.; Crichton, K.; Daigle, T. L.; Dalley, R.; De Frates, R. A.; Dee, N.; Desta, T.; Lee, S. D.; Dotson, N.; Egdorf, T.; Ellingwood, L.; Enstrom, R.; Esposito, L.; Farrell, C.; Feng, D.; Fong, O.; Gala, R.; Gamlin, C.; Gary, A.; Glandon, A.; Goldy, J.; Gorham, M.; Graybuck, L.; Gu, H.; Hadley, K.; Hawrylycz, M. J.; Henry, A. M.; Hill, D.; Hupp, M.; Kebede, S.; Kim, T. K.; Kim, L.; Kroll, M.; Lee, C.; Link, K. E.; Mallory,

M.; Mann, R.; Maxwell, M.; McGraw, M.; McMillen, D.; Mukora, A.; Ng, L.; Ng, L.; Ngo, K.; Nicovich, P. R.; Oldre, A.; Park, D.; Peng, H.; Penn, O.; Pham, T.; Pom, A.; Popović, Z.; Potekhina, L.; Rajanbabu, R.; Ransford, S.; Reid, D.; Rimorin, C.; Robertson, M.; Ronellenfitch, K.; Ruiz, A.; Sandman, D.; Smith, K.; Sulc, J.; Sunkin, S. M.; Szafer, A.; Tieu, M.; Torkelson, A.; Trinh, J.; Tung, H.; Wakeman, W.; Ward, K.; Williams, G.; Zhou, Z.; Ting, J. T.; Arkhipov, A.; Sümbül, U.; Lein, E. S.; Koch, C.; Yao, Z.; Tasic, B.; Berg, J.; Murphy, G. J.; Zeng, H. Integrated Morphoelectric and Transcriptomic Classification of Cortical GABAergic Cells. *Cell* **2020**, *183* (4), 935-953.e19. https://doi.org/10.1016/j.cell.2020.09.057.

(54) Lim, L.; Mi, D.; Llorca, A.; Marín, O. Development and Functional Diversification of Cortical Interneurons. *Neuron* **2018**, *100* (2), 294–313. https://doi.org/10.1016/j.neuron.2018.10.009.

(55) Wonders, C. P.; Anderson, S. A. The Origin and Specification of Cortical Interneurons. *Nat Rev Neurosci* **2006**, *7* (9), 687–696. https://doi.org/10.1038/nrn1954.

(56) Lavdas, A. A.; Grigoriou, M.; Pachnis, V.; Parnavelas, J. G. The Medial Ganglionic Eminence Gives Rise to a Population of Early Neurons in the Developing Cerebral Cortex. *J. Neurosci.* **1999**, *19* (18), 7881–7888. https://doi.org/10.1523/JNEUROSCI.19-18-07881.1999.

(57) Anderson, S. A.; Marín, O.; Horn, C.; Jennings, K.; Rubenstein, J. L. R. Distinct Cortical Migrations from the Medial and Lateral Ganglionic Eminences. *Development* **2001**, *128* (3), 353–363. https://doi.org/10.1242/dev.128.3.353.

(58) Tanaka, D.; Nakaya, Y.; Yanagawa, Y.; Obata, K.; Murakami, F. Multimodal Tangential Migration of Neocortical GABAergic Neurons Independent of GPI-Anchored Proteins. *Development* **2003**, *130* (23), 5803–5813. https://doi.org/10.1242/dev.00825.

(59) Bellion, A. Nucleokinesis in Tangentially Migrating Neurons Comprises Two Alternating Phases: Forward Migration of the Golgi/Centrosome Associated with Centrosome Splitting and Myosin Contraction at the Rear. *Journal of Neuroscience* **2005**, *25* (24), 5691–5699. https://doi.org/10.1523/JNEUROSCI.1030-05.2005.

(60) Silva, C. G.; Peyre, E.; Adhikari, M. H.; Tielens, S.; Tanco, S.; Van Damme, P.; Magno, L.; Krusy, N.; Agirman, G.; Magiera, M. M.; Kessaris, N.; Malgrange, B.; Andrieux, A.; Janke, C.; Nguyen, L. Cell-Intrinsic Control of Interneuron Migration Drives Cortical Morphogenesis. *Cell* **2018**, *172* (5), 1063-1078.e19. https://doi.org/10.1016/j.cell.2018.01.031.

(61) Toudji, I.; Toumi, A.; Chamberland, É.; Rossignol, E. Interneuron Odyssey: Molecular Mechanisms of Tangential Migration. *Front Neural Circuits* **2023**, *17*, 1256455. https://doi.org/10.3389/fncir.2023.1256455.

(62) Marín, O.; Yaron, A.; Bagri, A.; Tessier-Lavigne, M.; Rubenstein, J. L. R. Sorting of Striatal and Cortical Interneurons Regulated by Semaphorin-Neuropilin Interactions. *Science* **2001**, *293* (5531), 872–875. https://doi.org/10.1126/science.1061891.

(63) Martini, F. J.; Valiente, M.; López Bendito, G.; Szabó, G.; Moya, F.; Valdeolmillos, M.; Marín, O. Biased Selection of Leading Process Branches Mediates Chemotaxis during Tangential Neuronal Migration. *Development* **2009**, *136* (1), 41–50. https://doi.org/10.1242/dev.025502.

(64) Behar, T.; Li, Y.; Tran, H.; Ma, W.; Dunlap, V.; Scott, C.; Barker, J. GABA Stimulates Chemotaxis and Chemokinesis of Embryonic Cortical Neurons via Calcium-Dependent Mechanisms. *J. Neurosci.* **1996**, *16* (5), 1808–1818. https://doi.org/10.1523/JNEUROSCI.16-05-01808.1996.

(65) Li, G.; Adesnik, H.; Li, J.; Long, J.; Nicoll, R. A.; Rubenstein, J. L. R.; Pleasure, S. J. Regional Distribution of Cortical Interneurons and Development of Inhibitory Tone Are Regulated by Cxcl12/Cxcr4 Signaling. *J. Neurosci.* **2008**, *28* (5), 1085–1098. https://doi.org/10.1523/JNEUROSCI.4602-07.2008.

(66) Marín, O. Cellular and Molecular Mechanisms Controlling the Migration of Neocortical Interneurons. *Eur J Neurosci* **2013**, *38* (1), 2019–2029. https://doi.org/10.1111/ejn.12225.

(67) Stoufflet, J.; Tielens, S.; Nguyen, L. Shaping the Cerebral Cortex by Cellular Crosstalk. *Cell* **2023**, *186* (13), 2733–2747. https://doi.org/10.1016/j.cell.2023.05.040.

(68) Bastaki, F.; Nair, P.; Mohamed, M.; Malik, E. M.; Helmi, M.; Al-Ali, M. T.; Hamzeh, A. R. Identification of a Novel CTCF Mutation Responsible for Syndromic Intellectual Disability – a Case Report. *BMC Med Genet* **2017**, *18* (1), 68. https://doi.org/10.1186/s12881-017-0429-0.

(69) Peyre, E.; Silva, C. G.; Nguyen, L. Crosstalk between Intracellular and Extracellular Signals Regulating Interneuron Production, Migration and Integration into the Cortex. *Front. Cell. Neurosci.* **2015**, *9*. https://doi.org/10.3389/fncel.2015.00129.

(70) Anderson, S. A.; Eisenstat, D. D.; Shi, L.; Rubenstein, J. L. R. Interneuron Migration from Basal Forebrain to Neocortex: Dependence on *Dlx* Genes. *Science* **1997**, *278* (5337), 474–476. https://doi.org/10.1126/science.278.5337.474.

(71) Petryniak, M. A.; Potter, G. B.; Rowitch, D. H.; Rubenstein, J. L. R. Dlx1 and Dlx2 Control Neuronal versus Oligodendroglial Cell Fate Acquisition in the Developing Forebrain. *Neuron* **2007**, *55* (3), 417–433. https://doi.org/10.1016/j.neuron.2007.06.036.

(72) Azzarelli, R.; Kerloch, T.; Pacary, E. Regulation of Cerebral Cortex Development by Rho GTPases: Insights from in Vivo Studies. *Front. Cell. Neurosci.* **2015**, *8*. https://doi.org/10.3389/fncel.2014.00445.

(73) Pacary, E.; Heng, J.; Azzarelli, R.; Riou, P.; Castro, D.; Lebel-Potter, M.; Parras, C.; Bell, D. M.; Ridley, A. J.; Parsons, M.; Guillemot, F. Proneural Transcription Factors Regulate Different Steps of Cortical Neuron Migration through Rnd-Mediated Inhibition of RhoA Signaling. *Neuron* **2011**, *69* (6), 1069–1084. https://doi.org/10.1016/j.neuron.2011.02.018.

(74) Reiner, O.; Sapir, T. LIS1 Functions in Normal Development and Disease. *Current Opinion in Neurobiology* **2013**, *23* (6), 951–956. https://doi.org/10.1016/j.conb.2013.08.001.

(75) Lysko, D. E.; Putt, M.; Golden, J. A. SDF1 Reduces Interneuron Leading Process Branching through Dual Regulation of Actin and Microtubules. *J. Neurosci.* **2014**, *34* (14), 4941–4962. https://doi.org/10.1523/JNEUROSCI.4351-12.2014.

(76) Inamura, N.; Kimura, T.; Tada, S.; Kurahashi, T.; Yanagida, M.; Yanagawa, Y.; Ikenaka, K.; Murakami, F. Intrinsic and Extrinsic Mechanisms Control the Termination of Cortical Interneuron Migration. *J. Neurosci.* **2012**, *32* (17), 6032–6042. https://doi.org/10.1523/JNEUROSCI.3446-11.2012.

(77) Bortone, D.; Polleux, F. KCC2 Expression Promotes the Termination of Cortical Interneuron Migration in a Voltage-Sensitive Calcium-Dependent Manner. *Neuron* **2009**, *62* (1), 53–71. https://doi.org/10.1016/j.neuron.2009.01.034.

(78) Markram, H.; Toledo-Rodriguez, M.; Wang, Y.; Gupta, A.; Silberberg, G.; Wu, C. Interneurons of the Neocortical Inhibitory System. *Nat Rev Neurosci* **2004**, *5* (10), 793–807. https://doi.org/10.1038/nrn1519.

(79) Fino, E.; Packer, A. M.; Yuste, R. The Logic of Inhibitory Connectivity in the Neocortex. *Neuroscientist* **2013**, *19* (3), 228–237. https://doi.org/10.1177/1073858412456743.

(80) Su, J.; Basso, D.; Iyer, S.; Su, K.; Wei, J.; Fox, M. A. Paracrine Role for Somatostatin Interneurons in the Assembly of Perisomatic Inhibitory Synapses. *J. Neurosci.* **2020**, *40* (39), 7421–7435. https://doi.org/10.1523/JNEUROSCI.0613-20.2020.

(81) Batool, S.; Raza, H.; Zaidi, J.; Riaz, S.; Hasan, S.; Syed, N. I. Synapse Formation: From Cellular and Molecular Mechanisms to Neurodevelopmental and Neurodegenerative Disorders. *Journal of Neurophysiology* **2019**, *121* (4), 1381–1397. https://doi.org/10.1152/jn.00833.2018.

(82) Baas, P. W.; Luo, L. Signaling at the Growth Cone. *Neuron* **2001**, *32* (6), 981–984. https://doi.org/10.1016/S0896-6273(01)00556-6.

(83) Seiradake, E.; Jones, E. Y.; Klein, R. Structural Perspectives on Axon Guidance. *Annu. Rev. Cell Dev. Biol.* **2016**, *32* (1), 577–608. https://doi.org/10.1146/annurev-cellbio-111315-125008.

(84) Stavoe, A. K. H.; Colón-Ramos, D. A. Netrin Instructs Synaptic Vesicle Clustering through Rac GTPase, MIG-10, and the Actin Cytoskeleton. *Journal of Cell Biology* **2012**, *197* (1), 75–88. https://doi.org/10.1083/jcb.201110127.

(85) Kolodkin, A. L. Semaphorins: Mediators of Repulsive Growth Cone Guidance. *Trends in Cell Biology* **1996**, *6* (1), 15–22. https://doi.org/10.1016/0962-8924(96)81033-6.

(86) Dent, E. W.; Gupton, S. L.; Gertler, F. B. The Growth Cone Cytoskeleton in Axon Outgrowth and Guidance. *Cold Spring Harbor Perspectives in Biology* **2011**, *3* (3), a001800–a001800. https://doi.org/10.1101/cshperspect.a001800.

(87) Rakic, S.; Zecevic, N. Programmed Cell Death in the Developing Human Telencephalon. *Eur J of Neuroscience* **2000**, *12* (8), 2721–2734. https://doi.org/10.1046/j.1460-9568.2000.00153.x.

(88) Southwell, D. G.; Paredes, M. F.; Galvao, R. P.; Jones, D. L.; Froemke, R. C.; Sebe, J. Y.; Alfaro-Cervello, C.; Tang, Y.; Garcia-Verdugo, J. M.; Rubenstein, J. L.; Baraban, S. C.; Alvarez-Buylla, A. Intrinsically Determined Cell Death of Developing Cortical Interneurons. *Nature* **2012**, *491* (7422), 109–113. https://doi.org/10.1038/nature11523.

(89) Wong, F. K.; Bercsenyi, K.; Sreenivasan, V.; Portalés, A.; Fernández-Otero, M.; Marín, O. Pyramidal Cell Regulation of Interneuron Survival Sculpts Cortical Networks. *Nature* **2018**, *557* (7707), 668–673. https://doi.org/10.1038/s41586-018-0139-6.

(90) Southwell, D. G.; Paredes, M. F.; Galvao, R. P.; Jones, D. L.; Froemke, R. C.; Sebe, J. Y.; Alfaro-Cervello, C.; Tang, Y.; Garcia-Verdugo, J. M.; Rubenstein, J. L.; Baraban, S. C.; Alvarez-Buylla, A. Intrinsically Determined Cell Death of Developing Cortical Interneurons. *Nature* **2012**, *491* (7422), 109–113. https://doi.org/10.1038/nature11523.

(91) Murphy, D. L.; Lesch, K.-P. Targeting the Murine Serotonin Transporter: Insights into Human Neurobiology. *Nat Rev Neurosci* **2008**, *9* (2), 85–96. https://doi.org/10.1038/nrn2284.

(92) Homberg, J. R.; Schubert, D.; Gaspar, P. New Perspectives on the Neurodevelopmental Effects of SSRIs. *Trends in Pharmacological Sciences* **2010**, *31* (2), 60–65. https://doi.org/10.1016/j.tips.2009.11.003.

(93) Liu, G.; Dwyer, T. Microtubule Dynamics in Axon Guidance. *Neurosci. Bull.* **2014**, *30* (4), 569–583. https://doi.org/10.1007/s12264-014-1444-6.

(94) Rodriguez-Calado, S.; Avilés, F. X.; Lorenzo, J. Cytosolic Carboxypeptidase 1. In *Handbook of Proteolytic Enzymes*; Elsevier, 2025; pp 1631–1637. https://doi.org/10.1016/B978-0-443-28849-4.00254-X.

(95) Janke, C.; Rogowski, K.; Wloga, D.; Regnard, C.; Kajava, A. V.; Strub, J.-M.; Temurak, N.; Van Dijk, J.; Boucher, D.; Van Dorsselaer, A.; Suryavanshi, S.; Gaertig, J.; Eddé, B. Tubulin Polyglutamylase Enzymes Are Members of the TTL Domain Protein Family. *Science* **2005**, *308* (5729), 1758–1762. https://doi.org/10.1126/science.1113010.

(96) Van Dijk, J.; Rogowski, K.; Miro, J.; Lacroix, B.; Eddé, B.; Janke, C. A Targeted Multienzyme Mechanism for Selective Microtubule Polyglutamylation. *Molecular Cell* **2007**, *26* (3), 437–448. https://doi.org/10.1016/j.molcel.2007.04.012.

(97) Berezniuk, I.; Lyons, P. J.; Sironi, J. J.; Xiao, H.; Setou, M.; Angeletti, R. H.; Ikegami, K.; Fricker, L. D. Cytosolic Carboxypeptidase 5 Removes α- and γ-Linked Glutamates from Tubulin. *Journal of Biological Chemistry* **2013**, *288* (42), 30445–30453. https://doi.org/10.1074/jbc.M113.497917.

(98) Aillaud, C.; Bosc, C.; Peris, L.; Bosson, A.; Heemeryck, P.; Van Dijk, J.; Le Friec, J.; Boulan, B.; Vossier, F.; Sanman, L. E.; Syed, S.; Amara, N.; Couté, Y.; Lafanechère, L.; Denarier, E.; Delphin, C.; Pelletier, L.; Humbert, S.; Bogyo, M.; Andrieux, A.; Rogowski, K.; Moutin, M.-J. Vasohibins/SVBP Are Tubulin Carboxypeptidases (TCPs) That Regulate Neuron Differentiation. *Science* **2017**, *358* (6369), 1448–1453. https://doi.org/10.1126/science.aao4165.

(99) Nieuwenhuis, J.; Adamopoulos, A.; Bleijerveld, O. B.; Mazouzi, A.; Stickel, E.; Celie, P.; Altelaar, M.; Knipscheer, P.; Perrakis, A.; Blomen, V. A.; Brummelkamp, T. R. Vasohibins Encode Tubulin Detyrosinating Activity. *Science* **2017**, *358* (6369), 1453–1456. https://doi.org/10.1126/science.aao5676.

(100) Tielens, S.; Huysseune, S.; Godin, J. D.; Chariot, A.; Malgrange, B.; Nguyen, L. Elongator Controls Cortical Interneuron Migration by Regulating Actomyosin Dynamics. *Cell Res* **2016**, *26* (10), 1131–1148. https://doi.org/10.1038/cr.2016.112.

(101) Shashi, V.; Magiera, M. M.; Klein, D.; Zaki, M.; Schoch, K.; Rudnik-Schöneborn, S.; Norman, A.; Lopes Abath Neto, O.; Dusl, M.; Yuan, X.; Bartesaghi, L.; De Marco, P.; Alfares, A. A.; Marom, R.; Arold, S. T.; Guzmán-Vega, F. J.; Pena, L. D.; Smith, E. C.; Steinlin, M.; Babiker, M. O.; Mohassel, P.; Foley, A. R.; Donkervoort, S.; Kaur, R.; Ghosh, P. S.; Stanley, V.; Musaev, D.; Nava, C.; Mignot, C.; Keren, B.; Scala, M.; Tassano, E.; Picco, P.; Doneda, P.; Fiorillo, C.; Issa, M. Y.; Alassiri, A.; Alahmad, A.; Gerard, A.; Liu, P.; Yang, Y.; Ertl-Wagner, B.; Kranz, P. G.; Wentzensen, I. M.; Stucka, R.; Stong, N.; Allen, A. S.; Goldstein, D. B.; Undiagnosed Diseases Network; Schoser, B.; Rösler, K. M.; Alfadhel, M.; Capra, V.; Chrast, R.; Strom, T. M.; Kamsteeg, E.; Bönnemann, C. G.; Gleeson, J. G.; Martini, R.; Janke, C.; Senderek, J. Loss of Tubulin Deglutamylase CCP 1 Causes Infantile-onset Neurodegeneration. *The EMBO Journal* **2018**, *37* (23), e100540. https://doi.org/10.15252/embj.2018100540.

(102) Quadrato, G.; Brown, J.; Arlotta, P. The Promises and Challenges of Human Brain Organoids as Models of Neuropsychiatric Disease. *Nat Med* **2016**, *22* (11), 1220–1228. https://doi.org/10.1038/nm.4214.

(103) Lancaster, M. A.; Renner, M.; Martin, C.-A.; Wenzel, D.; Bicknell, L. S.; Hurles, M. E.; Homfray, T.; Penninger, J. M.; Jackson, A. P.; Knoblich, J. A. Cerebral Organoids Model Human Brain Development and Microcephaly. *Nature* **2013**, *501* (7467), 373–379. https://doi.org/10.1038/nature12517.

(104) Paşca, A. M.; Sloan, S. A.; Clarke, L. E.; Tian, Y.; Makinson, C. D.; Huber, N.; Kim, C. H.; Park, J.-Y.; O'Rourke, N. A.; Nguyen, K. D.; Smith, S. J.; Huguenard, J. R.; Geschwind, D. H.; Barres, B. A.; Paşca, S. P. Functional Cortical Neurons and Astrocytes from Human Pluripotent Stem Cells in 3D Culture. *Nat Methods* **2015**, *12* (7), 671–678. https://doi.org/10.1038/nmeth.3415.

(105) Camp, J. G.; Badsha, F.; Florio, M.; Kanton, S.; Gerber, T.; Wilsch-Bräuninger, M.; Lewitus, E.; Sykes, A.; Hevers, W.; Lancaster, M.; Knoblich, J. A.; Lachmann, R.; Pääbo, S.; Huttner, W. B.; Treutlein, B. Human Cerebral Organoids Recapitulate Gene Expression Programs of Fetal Neocortex Development. *Proc. Natl. Acad. Sci. U.S.A.* **2015**, *112* (51), 15672–15677. https://doi.org/10.1073/pnas.1520760112.

(106) Hansen, D. V.; Lui, J. H.; Parker, P. R. L.; Kriegstein, A. R. Neurogenic Radial Glia in the Outer Subventricular Zone of Human Neocortex. *Nature* **2010**, *464* (7288), 554–561. https://doi.org/10.1038/nature08845.

(107) Qian, X.; Nguyen, H. N.; Song, M. M.; Hadiono, C.; Ogden, S. C.; Hammack, C.; Yao, B.; Hamersky, G. R.; Jacob, F.; Zhong, C.; Yoon, K.; Jeang, W.; Lin, L.; Li, Y.; Thakor, J.; Berg, D. A.; Zhang, C.; Kang, E.; Chickering, M.; Nauen, D.; Ho, C.-Y.; Wen, Z.; Christian, K. M.; Shi, P.-Y.; Maher, B. J.; Wu, H.; Jin, P.; Tang, H.; Song, H.; Ming, G. Brain-Region-Specific Organoids Using Mini-Bioreactors for Modeling ZIKV Exposure. *Cell* **2016**, *165* (5), 1238–1254. https://doi.org/10.1016/j.cell.2016.04.032.

(108) Di Lullo, E.; Kriegstein, A. R. The Use of Brain Organoids to Investigate Neural Development and Disease. *Nat Rev Neurosci* **2017**, *18* (10), 573–584. https://doi.org/10.1038/nrn.2017.107.

(109) Zhao, H. H.; Haddad, G. Brain Organoid Protocols and Limitations. *Front. Cell. Neurosci.* **2024**, *18*, 1351734. https://doi.org/10.3389/fncel.2024.1351734.

(110) Takahashi, K.; Tanabe, K.; Ohnuki, M.; Narita, M.; Ichisaka, T.; Tomoda, K.; Yamanaka, S. Induction of Pluripotent Stem Cells from Adult Human Fibroblasts by Defined Factors. *Cell* **2007**, *131* (5), 861–872. https://doi.org/10.1016/j.cell.2007.11.019.

(111) Takahashi, K.; Yamanaka, S. Induction of Pluripotent Stem Cells from Mouse Embryonic and Adult Fibroblast Cultures by Defined Factors. *Cell* **2006**, *126* (4), 663–676. https://doi.org/10.1016/j.cell.2006.07.024.

(112) Yu, J.; Vodyanik, M. A.; Smuga-Otto, K.; Antosiewicz-Bourget, J.; Frane, J. L.; Tian, S.; Nie, J.; Jonsdottir, G. A.; Ruotti, V.; Stewart, R.; Slukvin, I. I.; Thomson, J. A. Induced Pluripotent Stem Cell Lines Derived from Human Somatic Cells. *Science* **2007**, *318* (5858), 1917–1920. https://doi.org/10.1126/science.1151526.

(113) Cerneckis, J.; Cai, H.; Shi, Y. Induced Pluripotent Stem Cells (iPSCs): Molecular Mechanisms of Induction and Applications. *Sig Transduct Target Ther* **2024**, *9* (1), 112. https://doi.org/10.1038/s41392-024-01809-0.

(114) Zhang, Z.; O'Laughlin, R.; Song, H.; Ming, G. Patterning of Brain Organoids Derived from Human Pluripotent Stem Cells. *Current Opinion in Neurobiology* **2022**, *74*, 102536. https://doi.org/10.1016/j.conb.2022.102536.

(115) Ying, Q.-L.; Stavridis, M.; Griffiths, D.; Li, M.; Smith, A. Conversion of Embryonic Stem Cells into Neuroectodermal Precursors in Adherent Monoculture. *Nat Biotechnol* **2003**, *21* (2), 183–186. https://doi.org/10.1038/nbt780.

(116) Lancaster, M. A.; Renner, M.; Martin, C.-A.; Wenzel, D.; Bicknell, L. S.; Hurles, M. E.; Homfray, T.; Penninger, J. M.; Jackson, A. P.; Knoblich, J. A. Cerebral Organoids Model Human Brain Development and Microcephaly. *Nature* **2013**, *501* (7467), 373–379. https://doi.org/10.1038/nature12517.

(117) Shi, Y.; Kirwan, P.; Smith, J.; Robinson, H. P. C.; Livesey, F. J. Human Cerebral Cortex Development from Pluripotent Stem Cells to Functional Excitatory Synapses. *Nat Neurosci* **2012**, *15* (3), 477–486, S1. https://doi.org/10.1038/nn.3041.

(118) Kadoshima, T.; Sakaguchi, H.; Nakano, T.; Soen, M.; Ando, S.; Eiraku, M.; Sasai, Y. Self-Organization of Axial Polarity, inside-out Layer Pattern, and Species-Specific Progenitor Dynamics in Human ES Cell–Derived Neocortex. *Proc. Natl. Acad. Sci. U.S.A.* **2013**, *110* (50), 20284–20289. https://doi.org/10.1073/pnas.1315710110.

(119) Chambers, S. M.; Fasano, C. A.; Papapetrou, E. P.; Tomishima, M.; Sadelain, M.; Studer, L. Highly Efficient Neural Conversion of Human ES and iPS Cells by Dual Inhibition of SMAD Signaling. *Nat Biotechnol* **2009**, *27* (3), 275–280. https://doi.org/10.1038/nbt.1529.

(120) Puspita, L.; Deline, M.; Shim, J. Dual SMAD Inhibition as a Versatile Platform in Human Pluripotent Stem Cell–Based Regenerative Medicine and Disease Modeling. *Molecules and Cells* **2025**, *48* (11), 100284. https://doi.org/10.1016/j.mocell.2025.100284.

(121) Birey, F.; Andersen, J.; Makinson, C. D.; Islam, S.; Wei, W.; Huber, N.; Fan, H. C.; Metzler, K. R. C.; Panagiotakos, G.; Thom, N.; O'Rourke, N. A.; Steinmetz, L. M.; Bernstein, J. A.; Hallmayer, J.; Huguenard, J. R.; Paşca, S. P. Assembly of Functionally Integrated Human Forebrain Spheroids. *Nature* **2017**, *545* (7652), 54–59. https://doi.org/10.1038/nature22330.

(122) Xiang, Y.; Tanaka, Y.; Patterson, B.; Kang, Y.-J.; Govindaiah, G.; Roselaar, N.; Cakir, B.; Kim, K.-Y.; Lombroso, A. P.; Hwang, S.-M.; Zhong, M.; Stanley, E. G.; Elefanty, A. G.; Naegele, J. R.; Lee, S.-H.; Weissman, S. M.; Park, I.-H. Fusion of Regionally Specified hPSC-Derived Organoids Models Human Brain Development and Interneuron Migration. *Cell Stem Cell* **2017**, *21* (3), 383-398.e7. https://doi.org/10.1016/j.stem.2017.07.007.

(123) Xiang, Y.; Tanaka, Y.; Patterson, B.; Kang, Y.-J.; Govindaiah, G.; Roselaar, N.; Cakir, B.; Kim, K.-Y.; Lombroso, A. P.; Hwang, S.-M.; Zhong, M.; Stanley, E. G.; Elefanty, A. G.; Naegele, J. R.; Lee, S.-H.; Weissman, S. M.; Park, I.-H. Fusion of Regionally Specified hPSC-Derived Organoids Models Human Brain Development and Interneuron Migration. *Cell Stem Cell* **2017**, *21* (3), 383-398.e7. https://doi.org/10.1016/j.stem.2017.07.007.

(124) Bagley, J. A.; Reumann, D.; Bian, S.; Lévi-Strauss, J.; Knoblich, J. A. Fused Cerebral Organoids Model Interactions between Brain Regions. *Nat Methods* **2017**, *14* (7), 743–751. https://doi.org/10.1038/nmeth.4304.

(125) Bagley, J. A.; Reumann, D.; Bian, S.; Lévi-Strauss, J.; Knoblich, J. A. Fused Cerebral Organoids Model Interactions between Brain Regions. *Nat Methods* **2017**, *14* (7), 743–751. https://doi.org/10.1038/nmeth.4304.

(126) Adlakha, Y. K. Human 3D Brain Organoids: Steering the Demolecularization of Brain and Neurological Diseases. *Cell Death Discov.* **2023**, *9* (1), 221. https://doi.org/10.1038/s41420-023-01523-w.

(127) Le Bail, R.; Bonafina, A.; Espuny-Camacho, I.; Nguyen, L. Learning about Cell Lineage, Cellular Diversity and Evolution of the Human Brain through Stem Cell Models. *Current Opinion in Neurobiology* **2021**, *66*, 166–177. https://doi.org/10.1016/j.conb.2020.10.018.

(128) Eisenstat, D. D.; Liu, J. K.; Mione, M.; Zhong, W.; Yu, G.; Anderson, S. A.; Ghattas, I.; Puelles, L.; Rubenstein, J. L. R. DLX-1, DLX-2, and DLX-5 Expression Define Distinct Stages of Basal Forebrain Differentiation. *J. Comp. Neurol.* **1999**, *414* (2), 217–237. https://doi.org/10.1002/(SICI)1096-9861(19991115)414:2%3C217::AID-CNE6%3E3.0.CO;2-I.

(129) Alzu'bi, A.; Lindsay, S.; Kerwin, J.; Looi, S. J.; Khalil, F.; Clowry, G. J. Distinct Cortical and Sub-Cortical Neurogenic Domains for GABAergic Interneuron Precursor Transcription Factors NKX2.1, OLIG2 and COUP-TFII in Early Fetal Human Telencephalon. *Brain Struct Funct* **2017**, *222* (5), 2309–2328. https://doi.org/10.1007/s00429-016-1343-5.

(130) Drost, J.; Clevers, H. Organoids in Cancer Research. *Nat Rev Cancer* **2018**, *18* (7), 407–418. https://doi.org/10.1038/s41568-018-0007-6.

(131) Matano, M.; Date, S.; Shimokawa, M.; Takano, A.; Fujii, M.; Ohta, Y.; Watanabe, T.; Kanai, T.; Sato, T. Modeling Colorectal Cancer Using CRISPR-Cas9–Mediated Engineering of Human Intestinal Organoids. *Nat Med* **2015**, *21* (3), 256–262. https://doi.org/10.1038/nm.3802.

(132) Huang, H.; He, W.; Tang, T.; Qiu, M. Immunological Markers for Central Nervous System Glia. *Neurosci. Bull.* **2023**, *39* (3), 379–392. https://doi.org/10.1007/s12264-022-00938-2.

(133) Gordon, A.; Yoon, S.-J.; Tran, S. S.; Makinson, C. D.; Park, J. Y.; Andersen, J.; Valencia, A. M.; Horvath, S.; Xiao, X.; Huguenard, J. R.; Pașca, S. P.; Geschwind, D. H. Long-Term Maturation of Human Cortical Organoids Matches Key Early Postnatal Transitions. *Nat Neurosci* **2021**, *24* (3), 331–342. https://doi.org/10.1038/s41593-021-00802-y.

(134) He, Z.; Dony, L.; Fleck, J. S.; Szałata, A.; Li, K. X.; Slišković, I.; Lin, H.-C.; Santel, M.; Atamian, A.; Quadrato, G.; Sun, J.; Pașca, S. P.; Human Cell Atlas Organoid Biological Network; Amin, N. D.; Kelley, K. W.; Bertucci, T.; Temple, S.; Bowles, K. R.; Caporale, N.; Villa, E.; Testa, G.; Cruceanu, C.; Binder, E. B.; Camp, J. G.; Theis, F. J.; Treutlein, B. An Integrated Transcriptomic Cell Atlas of Human Neural Organoids. *Nature* **2024**, *635* (8039), 690–698. https://doi.org/10.1038/s41586-024-08172-8.

(135) Dause, T. J.; Denninger, J. K.; Smith, B. M.; Kirby, E. D. The Neural Stem Cell Secretome across Neurodevelopment. *Experimental Neurology* **2022**, *355*, 114142. https://doi.org/10.1016/j.expneurol.2022.114142.

(136) Knecht, S.; Eberl, H. C.; Kreisz, N.; Ugwu, U. J.; Starikova, T.; Kuster, B.; Wilhelm, S. An Introduction to Analytical Challenges, Approaches, and Applications in Mass Spectrometry–Based Secretomics. *Molecular & Cellular Proteomics* **2023**, *22* (9), 100636. https://doi.org/10.1016/j.mcpro.2023.100636.

(137) Abdellaoui, S.; Katsimpardi, L. Neural Stem Cell Secretome: A Secret Key to Unlocking the Power of Regeneration in the Adult and Aging Brain. *Aging Brain* **2025**, *8*, 100144. https://doi.org/10.1016/j.nbas.2025.100144.

(138) The Gene Ontology Consortium; Aleksander, S. A The Gene Ontology Knowledgebase in 2023. *GENETICS* **2023**, *224* (1), iyad031. https://doi.org/10.1093/genetics/iyad031.

Use of AI: Artificial intelligence was used in this thesis for reformulation, syntaxis and translation purposes.

7. ANNEXES

1. SAMPLES SUMMARY

Tableau 6 : samples used for the quantification in Figure 18.

Figure	Lineage	N
SOX 2	Control #1	48Rosettes – 14Organoids – 4Trials
	Control #2	35Rosettes – 19Organoids – 4Trials
	CCP1 #1	44Rosettes – 19Organoids – 3Trials
	CCP1 #2	24Rosettes – 15Organoids – 1Trials
	CCP1 #3	16Rosettes – 14Organoids – 2Trials
PAX6	Control #1	17Rosettes – 10Organoids – 3Trials
	Control #2	40Rosettes – 12Organoids – 3Trials
	CCP1 #1	57Rosettes – 14Organoids – 4Trials
	CCP1 #2	10Rosettes – 16Organoids – 2Trials
	CCP1 #3	14Rosettes – 14Organoids – 2Trials
HOPX1	Control #1	7Rosettes – 3Organoids – 1Trials
	Control #2	3Rosettes – 1Organoids – 1Trials
	CCP1 #1	25Rosettes – 5Organoids – 1Trials
	CCP1 #2	0Rosettes – 0Organoids – 0Trials
	CCP1 #3	26Rosettes – 8Organoids – 2Trials
TBR2	Control #1	34Rosettes – 15Organoids – 5Trials
	Control #2	14Rosettes – 7Organoids – 3Trials
	CCP1 #1	33Rosettes – 17Organoids – 3Trials
	CCP1 #2	12Rosettes – 14Organoids – 2Trials
	CCP1 #3	17Rosettes – 14Organoids – 2Trials

2. PRIMERS SEQUENCES

Table 7: Sequences of primers used for the qPCR.

Gene	Forward sequence	Reverse sequence
CCP1	5'-GACACTCTTGCTGCATTGCT-3'	5'-GAATGAGCATGTTTCTATGCCG-3'
NKX2.1	5'-CGACTCGCTTCTCAGTGTCTGA-3'	5'-CCTCCATGCCCACTTTCTTG-3'
DCX	5'-AGGTACGTTTCTACCGCAATG-3'	5'-CAGCGTACACAATCCCCTTG-3'
DLX5	5'-TTCCAAGCTCCGTTCCAGAC-3'	5'-GAATCGGTAGCTGAAGACTCG-3'
GAD1	5'-AGGCAATCCTCCAAGAACCT-3'	5'-ATGTCCACCACTTCCAGGAG-3'
YWHAZ	5'-GTAGGAGCCCGTAGGTCATC-3'	5'-TTCTCAGCACCTTCCGTCTT-3'
HPRT	5'-ATTTCAAATCCAACAAGGTCTGGC-3'	5'-GCTTGCTGGTGAAAAGGACC-3'